

UNIVERSITY OF ŽILINA



TRANSCOM 2013

10-th EUROPEAN CONFERENCE
OF YOUNG RESEARCHERS AND SCIENTISTS

under the auspices of

Dušan Čaplovič

Minister of Education, Science, Research and Sport of the Slovak Republic

&

Tatiana Čorejová

Rector of the University of Žilina

SECTION 4

**ELECTRIC POWER SYSTEMS
ELECTRICAL AND ELECTRONIC ENGINEERING**

ŽILINA June 24 - 26, 2013
SLOVAK REPUBLIC

Edited by Ján Barabáš, Anton Lieskovský
© University of Žilina, 2013
ISBN: 978-80-554-0693-0

TRANSCOM 2013

10th European conference of young researchers and scientists

TRANSCOM 2013, the 10th international conference of young European researchers, scientists and educators, aims to establish and expand international contacts and co-operation. The 10th international conference TRANSCOM is jubilee. It will be held in the year when the University of Žilina celebrates 60 years since her constitution (1953 – 2013). The main purpose of the conference is to provide young researchers and scientists with an encouraging and stimulating environment in which they present results of their research to the scientific community. TRANSCOM has been organised regularly every other year since 1995. Between 160 and 400 young researchers and scientists participate regularly in the event. The conference is organised for postgraduate students and young researchers and scientists up to the age of 35 and their tutors. Young workers are expected to present the results they had achieved.

The conference is organised by the University of Žilina. It is the university with about 13 000 graduate and postgraduate students. The university offers Bachelor, Master and PhD programmes in the fields of transport, telecommunications, forensic engineering, management operations, information systems, in mechanical, civil, electrical, special engineering and in social sciences.

SECTIONS AND SCIENTIFIC COMMITTEE

1. TRANSPORT AND COMMUNICATIONS TECHNOLOGY.

Scientific committee: Bugaj M. (SK), Drozdziel P. (PL), Janáček J. (SK), Jánošíková Ľ. (SK), Kampf R. (CZ), Palúch S. (SK), Rievaj V. (SK)

2. ECONOMICS AND MANAGEMENT.

Scientific committee: Blašková M. (SK), Borkowski S. (PL), Gražulis V. (LT), Hittmár Š. (SK), Kucharčíková A. (SK), Kurtev I. (BG), Lyakin A. (RU), Rostášová M. (SK), Tomová A. (SK)

3. INFORMATION AND COMMUNICATION TECHNOLOGIES.

Scientific committee: Dado M. (SK), Klimo M. (SK), Kršák E. (SK), Matiaško K. (SK), Simunic D. (HR), Spalek J. (SK), Švadlenka L. (CZ), Vaculík J. (SK), Vaculík M. (SK), Vrček N. (HR)

4. ELECTRIC POWER SYSTEMS. ELECTRICAL AND ELECTRONIC ENGINEERING.

Scientific committee: Altus J. (SK), Brandštetter P. (CZ), Bury P. (SK), Čápová K. (SK), Dobrucký B. (SK), Janoušek L. (SK), Luft M. (PL), Szychta E. (PL), Špánik P. (SK), Vittek J. (SK)

5. MATERIAL ENGINEERING. MECHANICAL ENGINEERING TECHNOLOGIES.

Scientific committee: Adamczak S. (PL), Bolibruchová D. (SK), Cotetiu R. I. (RO), Dobrzanski L. A. (PL), Guagliano M. (I), Hadzima B. (SK), Konečná R. (SK), Kunz L. (CZ), Kuric I. (SK), Lukáč P. (CZ), Meško J. (SK), Neslušán M. (SK), Palček P. (SK), Takacs J. (H), Trojanová Z. (CZ), Ungureanu N. S. (RO)

6. MACHINES AND EQUIPMENT. APPLIED MECHANICS.

Scientific committee: Gerlici J. (SK), Chudzikiewicz A. (PL), Jandačka J. (SK), Medvecký Š. (SK), Mičieta B. (SK), Ochodek T. (CZ), Sága M. (SK), Žmindák M. (SK)

7. CIVIL ENGINEERING.

Scientific committee: Bujňák J. (SK), Grzeszczyk S. (PL), Ižvolt L. (SK), Malachova A. (RU), Melcer J. (SK), Nikolic R. (RS), Plášek O. (CZ), Segalini A. (I)

8. SOCIAL SCIENCES.

Scientific committee: Bálint V. (SK), Banáry B. (SK), Cabanová V. (SK), Dzhalladova I. (UKR), Jakubíková B. (SK), Khusainov D. (UKR), Kráľová Z. (SK), Marčoková M. (SK), Růžičková M. (SK), Schmeidel E. (PL)

9. SECURITY ENGINEERING. FORENSIC ENGINEERING.

Scientific committee: Kasanický G. (SK), Kohút P. (SK), Navrátil L. (CZ), Poledňák P. (CZ), Sventeková E. (SK), Šimák L. (SK), Weyde M. (D), Zagorecki A. (UK)

ORGANIZING COMMITTEE

CHAIRPERSONS

Čelko Ján, Bokůvka Otakar

EXECUTIVE SECRETARY

Vráblová Helena

MEMBERS

Antal M., Baďura Š., Barabáš J., Belan J., Blinova E., Brída P., Brumerčík F., Brůna M., Buc D., Bulej V., Cíba J., Dobeš P., Dulina L., Ďuranová L., Ďuríníková M., Fanfarová A., Gallíková J., Grajcaríková P., Hrbček J., Hyben B., Janík P., Januš P., Jůnová E., Kocifajová L., Kochláš M., Kubjatková M., Kuzmová M., Kvet M., Lieskovský A., Masárová G., Meško M., Michalková M., Nemček B., Nosek R., Pácha M., Plevková L., Pučková K., Sapieta M., Semanová Š., Sýkora P., Šimková I., Štefáníková L., Štůňová M., Šušlik L., Titko M., Vaško A., Ždánsky J., Žoltá L.



**SECTION 4 ELECTRIC POWER SYSTEMS
ELECTRICAL AND ELECTRONIC ENGINEERING**

REVIEWERS:

Altus Juraj
Babušiak Branko
Barabáš Ján
Beňová Mariana
Bracíník Peter
Brandštetter Pavel
Brandt Martin
Bury Peter
Čáповá Klára
Dobrucký Branislav
Ferková Želmíra
Frivaldský Michal
Gála Michal
Gombárska Daniela
Hockicko Peter
Höger Marek
Janoušek Ladislav
Kállay Fedor
Klimo Martin
Kúdelčík Jozef
Luft Miroslav
Pácha Matěj
Radil Roman
Skála Bohumil
Smetana Milan
Špánik Pavol
Šuch Ondrej
Vavruš Vladimír
Víttek Ján

Note: Authors are responsible for language contents of their papers.

CONTENTS

BAUER, JAN - HAUBERT, TOMÁŠ - LETTL, JIŘÍ, Prague, Czech Republic: Torque Control of Matrix Converter Fed Induction Machine Employing Fuzzy Logic.....	9
BIEL, ZDENO – VITTEK, JÁN – HRKEĽ, MICHAL – GOREL, LUKÁŠ, Žilina, Slovak Republic: dSPACE Implementation of Permanent Magnet Synchronous Motor Loss Minimization Control	13
BORIK, ŠTEFAN – ČÁP, IVO, Žilina, Slovak Republic: On the Analysis of Arterial Branching.....	19
DEŽELAK, KLEMEN - ŠTUMBERGER, GORAZD, Maribor, Slovenia: Evaluation of excessive transmission line losses caused by compact fluorescent lamps	23
DRGA, JOZEF – BURY, PETER, Žilina, Slovak Republic: Dielectric properties of transformer oil with dispersed magnetic nanoparticles	27
DÚBRAVKA, PETER – RAFAJDUS, PAVOL – HRABOVCOVÁ, VALÉRIA – MUŠÁK, MAREK, Žilina, Slovak Republic: Influence of Phase Winding Faults on Switched Reluctance Motor's Operation.....	31
FRÁTRIK, MILAN - BADURA, ŠTEFAN — ŽOLTÁ, LUCIE, Žilina, Slovak Republic: Fitting memristor models to observed behavior of TiO ₂ memristors	35
HAUBERT, TOMAS – MINDL, PAVEL, Praha, Czech Republic: Optimization of DC/DC Power Converter for Super-capacitor Charging and Discharging	43
HRUBOŠ, MARIÁN – JANOTA, ALEŠ, Žilina, Slovak Republic: Laser system based measurement of road surface and surrounding area.....	47
JURČÍK, JOZEF - GUTTEN, MIROSLAV - KORENČIAK, DANIEL, Žilina, Slovak Republic: Basics for compensation of FDS measurements for transformer insulation diagnostics.....	51
KAPUSTA, TOMAS - KOSCELNIK, JURAJ, Žilina, Slovak Republic: Electromagnetic interference of LLC resonant converter in different modes of operation	55
LUDWINEK, KRZYSZTOF – STASZAK, JAN – JURECKI, RAFAŁ – SADKOWSKI, WOJCIECH - MARCINIEWSKI, MATEUSZ – WIĘCKOWSKI, DAREK – KLIMONT, GRZEGORZ, Kielce, Poland: Moment of inertia influence on pulsation of rotational speed waveform in PMSM and SRM.....	59
MALÍKOVA, IVONA, Žilina, Slovak Republic: Mechanisms of non-thermal effects of low-frequency electromagnetic field on biological cells	65
MAŇAS, JAKUB – BILÍK, PETR, Ostrava, Czech Republic: The Application for Hybrid Power System Data Evaluation	69
MUŠÁK, MAREK – ŠTULRAJTER, MAREK – HRABOVCOVÁ, VALÉRIA – DÚBRAVKA, PETER, Žilina, Slovak Republic: Permanent Magnet Synchronous Motor Inductance Characteristics Investigation.....	75
OSTRICA, ĽUBOMÍR - GUTTEN, MIROSLAV, Žilina, Slovak Republic: Oxygen Gas Sensors for Automotive Application.....	81
PERNIŠOVÁ, VIERA - ČÁPOVÁ, KLÁRA, Žilina, Slovak Republic: Electromagnetic Non-destructive Testing Using Advanced Magnetic Sensors.....	85

PĚTVALDSKÝ, PETR – BILÍK, PETR, Ostrava, Czech Republic: Testing gapless measurement of PQA according to IEC 62586-2.....	89
RYBOVIČ, ANDREJ - PAŠKALA, MAREK - BYSTRICĀNOVÁ, ANNA, Źilina, Slovak Republic: Design control strategy for Inverted Pendulum.....	97
STAWCZYK, PAWEŁ, Kielce, Poland: The influence of the interphase reactor on the operation of 12 - pulse AC/DC thyristor rectifier	101
SZABÓ, DOMINIK - REGUŁA, MICHAL - HÖGER, MAREK, Źilina, Slovak Republic: Digital protection relay for 22 kV power line model.....	105
VAVRLA, TOMÁŠ – KOZIOREK, JIŘÍ, Ostrava, Czech Republic: Measurement and Data Acquisition from Technology of Thermal Borehole Polygons.....	109



Torque Control of Matrix Converter Fed Induction Machine Employing Fuzzy Logic

*Jan Bauer, *Tomas Haubert, *Jiri Lettl

*Czech Technical University in Prague, Faculty of Electrical Engineering, Department of Electric Drives and Traction, Technicka 2, 166 27- Praha 6, Czech Republic, bauerja2@fel.cvut.cz

Abstract. The matrix converter is a very popular topic because of its advantages in comparison with the indirect frequency converter [1]. The modulation strategy and control algorithm used are very important parts of the converter's controller. Recently modulation strategies based on a virtual DC-link space vector modulation are used, which works as a dependency injection [2]. That is why different approaches can be used to control both the output voltage and the input current at the same time. In this paper phase control of the input current in combination with a machine's torque fuzzy controller is presented. This enables us to overcome the traditional limitations of the output voltage without resigning from the input current control.

Keywords: Matrix Converter, Fuzzy Control, Induction Machine

1. Introduction

Modern electric drive can be comprehended as electro mechanic energy changer. The own change of electric energy to the mechanic energy is done by the electric motor. It needs for the demanded conversion proper voltage, currents or frequency on its terminals. In case of higher demands, like high dynamics of the motor is required, the converter is usually connected in front of the motor. The algorithms based on the separate control of the motor flux and torque are mostly used to obtain maximum performance from the induction machine [3].

From the point of control algorithm the Direct Torque Control (DTC) [3] is common high performance induction motor control method nowadays. In the DTC, the torque and flux are controlled directly by switching suitable voltage vectors. This is relatively close to sliding mode or fuzzy controller.

Origins of the Matrix Converter can be dated to late seventies [1]. In this contribution the name "Matrix Converter" means the symmetrical 3x3 topology consisting of nine bidirectional switches. Such converter belongs to the all silicon converter category. The modulation strategies based on virtual DC-link space vector modulation were developed [5]. Main advantage of this strategy is that different approaches can be used to control both the output voltage and the input current at the same time. In this paper the phase control of the input current in the combination with the fuzzy control of the output voltage is presented.

The research in the field of fuzzy control technique is carried out since 1974. The idea of the fuzzy controller is to design practical controller based on the qualitative knowledge of the system [4]. In the transferred meaning the fuzzy control then incorporates the experience and intuition of the designer. It does not need accurate mathematical model of the controlled system. That is why the fuzzy control perfectly fits for the systems with high degree of uncertainty or complex dynamics.

As was mentioned above the DTC algorithm is very popular in combination with IM, because it offers quick response with simple control structure. However it has several drawbacks like high torque ripple and variable switching frequency. To improve the performance of the DTC modern control approaches based on sliding mode or fuzzy control are used [6]. The main objective of this paper is to develop control strategy for the IM drive fed by matrix converter based on reduced state space model of the IM.

2. Reduced State Variable Model of the IM

The DTC algorithm need for proper and accurate function hardly measurable value of inner machine flux. Therefore machine models are used for determining the value of the flux from other measurable quantities. For establishing the machine equations will be used Γ -equivalent circuit (Fig. 1) in this paper. This choice simplifies the circuit by means of addition of the stator and stator leakage inductances into one inductance placed on the equivalent circuit rotor side without loss of information [7].

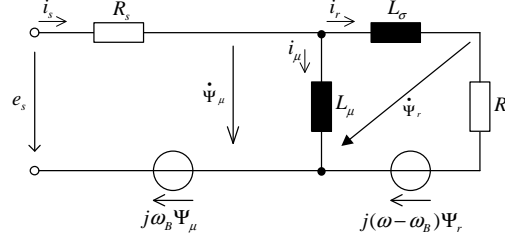


Fig. 1. Γ -equivalent circuit

The circuit in Fig. 1 can be described by equation (3) where \mathbf{A}_s represents the state matrix of the IM and the vector of inputs is \mathbf{b}_s .

$$\begin{pmatrix} \dot{\Psi}_\mu \\ \dot{i}_s \end{pmatrix} = \mathbf{A}_s \begin{pmatrix} \Psi_\mu \\ i_s \end{pmatrix} + \mathbf{b}_s(t). \quad (1)$$

where \mathbf{A}_s and \mathbf{b}_s - is (2),

$$\mathbf{A}_s = \begin{pmatrix} 0 & \omega_B & -R_s & 0 \\ -\omega_B & 0 & 0 & -R_s \\ \sigma_2 & \frac{\omega\sigma_3}{L_\mu L_\sigma} & \sigma_1 & \omega_B - \omega \\ -\frac{\omega\sigma_3}{L_\mu L_\sigma} & \sigma_2 & \omega - \omega_B & -\sigma_1 \end{pmatrix}, \quad \mathbf{b}_s(t) = \begin{pmatrix} e_{sa}(t) \\ e_{sb}(t) \\ \frac{e_{sa}(t)L_\mu + e_{sa}(t)L_\sigma}{L_\mu L_\sigma} \\ \frac{e_{sb}(t)L_\mu + e_{sb}(t)L_\sigma}{L_\mu L_\sigma} \end{pmatrix} \quad (2)$$

$$\sigma_1 = -\frac{R_r L_\mu + R_s L_\mu + R_s L_\sigma}{L_\mu L_\sigma}, \quad \sigma_2 = \frac{R_r}{L_\mu L_\sigma}, \quad \sigma_3 = L_\mu + L_\sigma.$$

From (2) it can be seen, that the induction machine is a 4th order system described by four linear differential equations. Here can set first simplifying assumption that the coordinate system is rotating with speed of flux. Therefore $\omega_B = \omega_1$, $\Psi_d = \Psi$ and $\Psi_q = 0$. Using this dynamically rotating coordinate system the original 4th order system will be reduced into a new 3rd order system. The Ψ_q component of the flux will be always zero. This will help when designing the control algorithm, because the torque of the machine will depend on Ψ_d and i_q components only. Because we aim to design fuzzy controller for the IM torque, we will set Ψ_d and i_q as our plane and all investigations will be related to this plane.

Based on the (2) can be analyzed also the transient behavior of the machine. This analysis is profitable especially for understanding the machine behaviour and lately when designing the controller. As a first step we can study the reaction of the machine to the application of some voltage vector. The results of such reactions are summarized in Fig. 2.

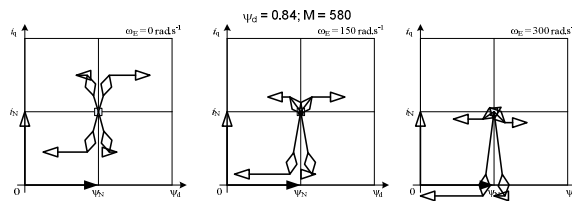


Fig. 2. Reaction of IM to applied voltage vector

3. Representation of the Matrix Converter

The absence of the DC-link and direct switching of the output phases to the input puts several restrictive conditions on the modulation strategy of the matrix converter. Firstly none of the input phases cannot be short-circuited, it means none of the output phases can be connected to two or more input phases at the same time. Secondly, because an inductive load is mostly connected to the output of the converter, there must be always available some conducting path at the output. To ensure this requirement, modulation strategies based on the virtual DC-link concept were developed for the matrix converter [2], [5]. It virtually splits matrix convert to input rectifier part and output inverter part. This enables to control both virtual parts quasi independently.

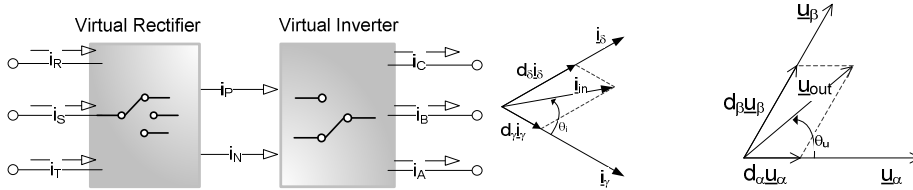


Fig. 3. Virtual DC-link concept

4. Fuzzy Controller Design

Returning to the above defined state variable plane Ψ_d and i_q we can define there two important points. First is desired torque Ψ_d^* and i_q^* and second is the current state of the machine state variables Ψ_d and i_q . The controller should move the current operation point to the desired operation point by the means of generating the proper voltage vectors. It is obvious that the fastest way of movement is direct line to from the current point to the desired one, however such voltage vector is not always available. Therefore the selection of the vectors will be on the fuzzy controller.

Using of reduced model of the IM leads to the fuzzy controller with two inputs and one output. First input variable is flux error, second is torque current component error. The output of the controller is then required voltage vector angle that will push the operation point to the desired one. Because the changing of the flux in the IM is relatively slow only three linguistic values, negative, zero and positive denoted as N, Z and P respectively are used to fuzzify flux linkage error domain. Because the change of the torque of the machine is faster than the change of the flux five linguistic values, negative high, negative, zero, positive and positive high denoted as NH, N, ZE, P and PH respectively are used to fuzzify torque error domain. Each fuzzy rule can be described using the two input linguistic variables $\Delta\Psi_d$, Δi_q and one output linguistic variable that represents desired angle of the converter's output voltage. In this paper, Mamdani's fuzzy rule base model is used to perform the function of proposed control algorithm [6]. The output membership function is designed based on the knowledge of machine reaction analysis to voltage vector (Fig. 2).

The output of the fuzzy controller is then used as input for selector of the nearest voltage vector available in the virtual inverter (Fig. 3).

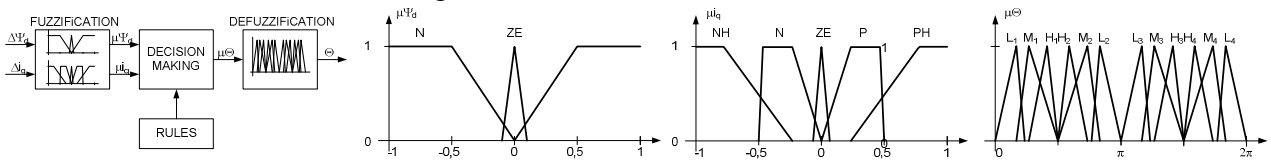


Fig. 4. Membership function mapping

5. Simulation Results

The model of the proposed control strategy was created in Matlab/Simulink. The simulation results of this control are depicted in Fig 4. Results of the simulation with the proposed control

strategy for the desired values of $\Psi_d = 0.84$ Wb, constant speed, and a different load torque are shown. The red line shows the desired torque and the green line represents the real torque. It can be seen that the controller tracks the desired value very quickly and without any oscillation in transitions. It's a movement of the desired machine state in the plane.

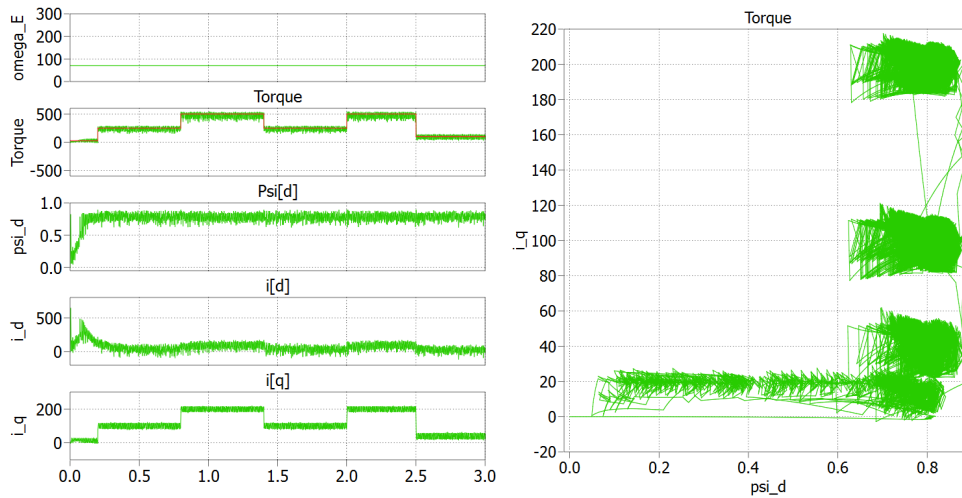


Fig. 5. Simulation results – reaction to torque steps

6. Conclusions

A control strategy of the matrix converter based on a virtual DC-link concept and fuzzy control of the torque was presented. The simulation results look very promising and show that the fuzzy control of the virtual inverter part can operate simultaneously with the independent input sinusoidal modulation. The responses of the controller to a change of the desired state are quick and without any overshoot. However, the real impact of the modulation can be evaluated first after the realization of the algorithm on the real converter prototype. Nevertheless, it is a solid basis for the further investigation and improvement of the suggested control concept for a matrix converter induction motor drive system.

Acknowledgment

The research was supported by the Grant Agency of the Czech Technical University, Prague, grant No. SGS13/073/OHK3/1T/13.

References

- [1] J.W. Kolar, T. Friedli, J. Rodriguez and P.W. Wheeler, "Review of three-phase PWM AC–AC converter topologies," *Industrial Electronics, IEEE Transactions on*, vol. 58, no. 11, pp. 4988-5006 2011.
- [2] Rodriguez, J.; Rivera, M.; Kolar, J.W.; Wheeler, P.W., "A Review of Control and Modulation Methods for Matrix Converters," *Industrial Electronics, IEEE Transactions on*, vol. 59, no. 1, pp. 58-70 2012.
- [3] P. Vas, *Sensorless vector and direct torque control*. Oxford, Oxford University Press, 1998.
- [4] Lee, C. C., "Fuzzy Logic in Control Systems: Fuzzy Logic Controller," *Power Electronics, IEEE Transactions on*, vol. 3, no. 4, pp. 420-429.
- [5] L. Helle, K.B. Larsen, A.H. Jorgensen, S. Munk-Nielsen and F. Blaabjerg, "Evaluation of modulation schemes for three-phase to three-phase matrix converters," *Industrial Electronics, IEEE Transactions on*, vol. 51, no. 1, pp. 158-171 2004.
- [6] Pujar, J.H.; Kodad, S.F., "Direct Torque Fuzzy Control of an AC Drive", in *Advances in Computing, Control, & Telecommunication Technologies, International conference on*, 2009.
- [7] J. Lettl, S. Fligl, J. Bauer, M. Vlcek, "Comparison of Gamma and T Models for Converter Controlled Induction Machine Drives", in *Proceedings of Piers 2012, Malaysia*, 2012.

dSPACE Implementation of Permanent Magnet Synchronous Motor Loss Minimization Control

*Zdeno Biel, *Ján Vittek, *Michal Hrkel, *Lukáš Gorel

*University of Zilina, Faculty of Electrical Engineering, Department of Power Electrical Systems,
Univerzitna 1, 01026 Zilina, Slovak Republic,
{Zdeno.Biel, Jan.Vittek, Michal.Hrkel, Lukas.Gorel}@fel.uniza.sk

Abstract. In this paper loss minimization control of permanent magnet synchronous motor is described. This method is based on equivalent circuit, which takes into account iron losses. Method for PMSM losses measurement is used to determine mechanical losses from measured data. Loss minimization control algorithm was implemented in dSPACE system and experimentally verified.

Keywords: Loss minimization, Permanent magnet synchronous motor, PMSM losses, dSPACE system.

1. Introduction

Electric motors are globally the largest consumers of produced electricity. Electric drives efficiency increase is very important not only for economy, but also for environment. The efficiency of the electric drives can be increased exploiting suitable types of electric machines as well as using suitable (*energy saving*) control strategies. Permanent magnet synchronous motors (PMSM) are characterized by high efficiency. Moreover interior PMSM offers advantages like high power density, wide speed range, mechanical robustness and wide range of flux weakening. However, maximum efficiency of these motors can be achieved via suitable control strategies. This paper describes interior PMSM loss minimization control algorithm, which is also experimentally verified.

2. Mathematical Model of PMSM Including Iron Losses

Dynamic d, q axis equivalent circuit of PMSM taking into account iron losses is shown in Fig.1. Iron losses are represented by resistance, R_i . Stator current components i_d, i_q are divided into iron loss currents, i_{di}, i_{qi} and magnetizing currents, i_{md}, i_{mq} .

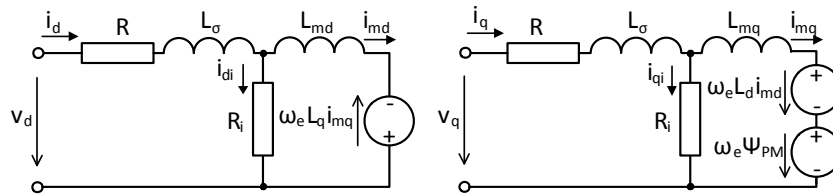


Fig. 1. Dynamic, rotor frame coupled equivalent circuit of PMSM taking into account iron losses.

Dynamic model of PMSM described in d, q rotating frame coupled to the rotor and respecting iron losses is described as follows:

$$v_d = R i_d + L_\sigma \frac{di_d}{dt} + L_{md} \frac{di_{md}}{dt} - \omega_e L_q i_{mq}, \quad (1)$$

$$v_q = R i_q + L_\sigma \frac{di_q}{dt} + L_{mq} \frac{di_{mq}}{dt} + \omega_e L_d i_{md} + \omega_e \Psi_{PM}, \quad (2)$$

$$\frac{d\omega_e}{dt} = \frac{p}{J} (T_E - T_L). \quad (3)$$

Iron loss currents, i_{cd} , i_{cq} , magnetizing currents, i_{md} , i_{mq} and electromagnetic torque, T_E are expressed as:

$$i_{di} = \frac{1}{R_i} \left(-\omega_e L_q i_{mq} + L_{md} \frac{di_{md}}{dt} \right), \quad (4)$$

$$i_{qi} = \frac{1}{R_i} \left[\omega_e (\Psi_{PM} + L_d i_{md}) + L_{mq} \frac{di_{mq}}{dt} \right], \quad (5)$$

$$i_{md} = i_d - i_{di}, \quad i_{mq} = i_q - i_{qi}, \quad (6)$$

$$T_E = \frac{3}{2} p [\Psi_{PM} i_{mq} + (L_d - L_q) i_{md} i_{mq}]. \quad (7)$$

3. PMSM Losses

Total PMSM losses consist of copper losses, iron losses, mechanical losses and stray load losses. Copper losses, P_{Cu} are generated by stator current flowing through stator winding resistance. Formula, which describes these losses is as follows:

$$P_{Cu} = \frac{3}{2} R (i_d^2 + i_q^2) = 3 R I_{rms}^2. \quad (8)$$

Iron losses P_i are divided into two components, hysteresis and eddy current losses. In equivalent circuit these losses are represented by resistance, R_i and can be expressed as:

$$P_i = \frac{3}{2} R_i (i_{di}^2 + i_{qi}^2) = \frac{3}{2} \frac{\omega_e^2}{R_i} (\Psi_d^2 + \Psi_q^2). \quad (9)$$

Mechanical losses, P_{mech} are caused by friction in the bearings. For motor with inner fan mechanical losses include also fan winding losses. Mechanical losses are expressed as:

$$P_{mech} = T_{mech} \omega_r, \quad (10)$$

where, T_{mech} is a friction torque and, ω_r is rotor angular speed.

Stray load losses are additional losses in a machine, which are not included as the sum of friction and fan winding losses, copper and core losses. The largest contribution to the stray load losses is produced by higher harmonics, which generate losses in the motor. Energies due to these losses are dissipated as currents in the resistance of copper windings, harmonic flux components in the iron parts, leakage flux in the laminated core.

3.1. Measurement of PMSM Losses

The methods for measurement of PMSM losses are described in [1], [2]. Experimental setup for losses measurement is shown in Fig. 2. PMSM is powered from voltage source inverter VSI, which is controlled by dSPACE system respecting applied vector control conditions. Load torque is generated by induction motor (IM) connected to the four quadrant inverter 4Q VSI capable of regenerative braking. Input power, P_{in} , RMS values of motor currents and voltages are measured by digital power meter DPM. Load torque is measured by torque transducer TT. Parameters of the tested PMSM used in the experiments are listed in Tab. 1. Copper losses can be calculated from (8) if RMS value of motor current is measured. The sum of iron, mechanical and stray load losses is expressed as:

$$P_l = P_{mech} + P_s + P_i = P_{mech} + P_s + \frac{3}{2} \frac{1}{R_i} \omega_e^2 (\Psi_d^2 + \Psi_q^2) = P_{in} - P_{out} - P_{Cu}. \quad (11)$$

The mechanical losses, P_{mech} , and stray load losses, P_s , are constant for constant operational speed and load torque. These losses, P_l can be regarded as the linear function to the squared speed-emf $\omega_e^2 (\Psi_d^2 + \Psi_q^2)$.

n_N	360 min ⁻¹	L_d	53.2 mH
T_N	50 Nm	L_q	106.2 mH
p	6	Ψ_{PM}	0.828 Wb
R_s	3.93Ω	R_c	2300Ω

Tab. 1. Motor parameters.

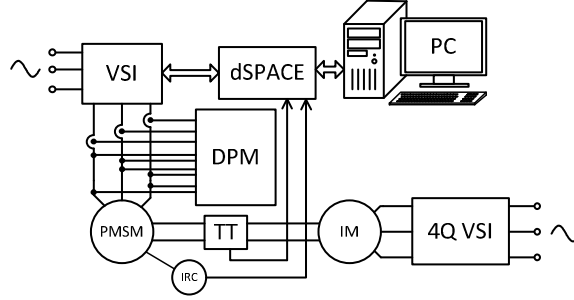


Fig. 2. Experimental setup for PMSM losses measurement.

Fig. 3.a shows the losses, P_l , input power and copper losses versus the square of speed-emf obtained by measuring in no-load condition at 360 rpm. The square of speed-emf can be calculated by using the electrical input power, P_{in} , RMS value of the armature voltage, V_{rms} , and RMS value of the armature current, I_{rms} :

$$\omega_e^2(\Psi_d^2 + \Psi_q^2) = (v_d - Ri_d)^2 + (v_q - Ri_q)^2 = V_{rms}^2 - 2RP_{in} + 3R^2I_{rms}^2. \quad (12)$$

Various values of speed-emf are obtained by changing of d-axes current, I_d .

In no-load condition, when output power is equal to zero, value of losses, P_l can be obtained by subtracting copper losses from measured input power. From (2) can be seen, that iron losses are equal zero, when $\omega_e^2(\Psi_d^2 + \Psi_q^2) = 0$. Therefore if, P_l values are interpolated by strength line, the intersection of this line with vertical axis corresponds to the sum of mechanical losses and stray losses. Taking into account, that stray losses are very small in no-load condition, then mechanical losses can be directly expressed. Measured mechanical losses as a function of motor speed are shown in Fig. 3.b.

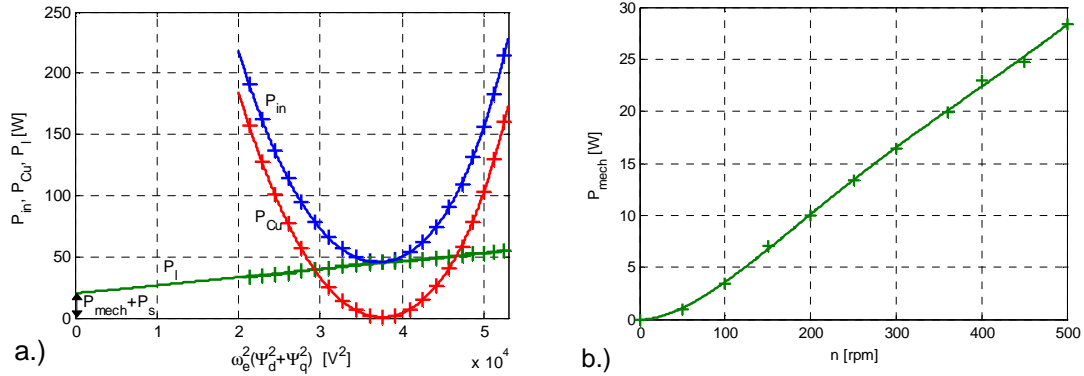


Fig. 3. a.) Losses vs. square of speed-emf for no-load state. b.) Mechanical losses vs. motor speed.

4. PMSM Loss Minimization Control Strategy

Electrical losses consist of copper and iron losses. These losses caused by the fundamental harmonic components of stator current and the total linkage flux can be minimized by appropriate control strategy. From equivalent circuit of Fig.1., the total electrical losses can be expressed as:

$$P_e = P_{Cu} + P_i = \frac{3}{2}R(i_d^2 + i_q^2) + \frac{3}{2}R_i(i_{di}^2 + i_{qi}^2). \quad (13)$$

After substituting equation (4), (5), (6), (7) into (13), the electrical losses can be expressed as a function of i_d , T_E and ω_e .

$$P_e(i_d, T_E, \omega_e) = P_{Cu}(i_d, T_E, \omega_e) + P_i(i_d, T_E, \omega_e). \quad (14)$$

In steady-state the motor torque, T_e and angular speed, ω_r are constant. Then the total electrical losses depend only on the value of, i_d . Fig. 4.a shows the total electrical losses, P_e , copper losses, P_{Cu} and iron losses, P_i as a function of current, i_d at the rated speed and the rated torque. The measured values are marked as +. Losses expressed from (4), (5), (6), (13) and (4) are represented

by solid curves. From Fig. 4.a it can be seen, that a minimum of electrical losses exists for define negative value of, i_d current. If d-axes current component is regulated to this optimal value, the motor efficiency for given speed and torque is maximal. However, the value of this optimal current varies with the motor speed and torque. Therefore it is necessary to express the optimal current, i_{d_opt} as a function of these parameters. Analytical solution can be obtained via fourth-order equation, which is not suitable for real time implementation. Therefore, other methods to determine i_{d_opt} were proposed. Work [3] suggest polynomial approximation of, i_{d_opt} as a function of, i_q for various motor speeds. Another way to determine, i_{d_opt} is described in [4]. A numerical algorithm that searches for the minimum of the function (14) is used to find optimal current, i_d . The variation of i_{d_opt} with load torque shows Fig. 4.b.

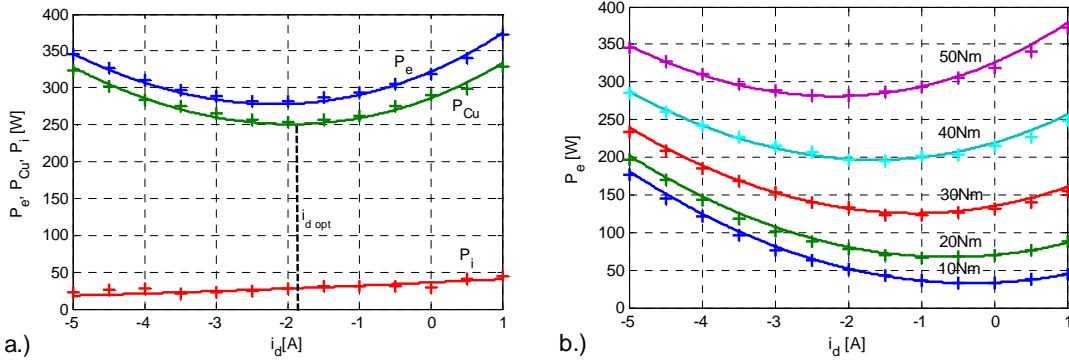


Fig. 4. a.) Motor losses as a function of i_d . b.) Variation of electrical losses with load torque.

Block diagram of vector controlled PMSM with implementation of the loss minimization algorithm is shown in Fig. 5. Desired optimal d-axis current, i_d and q-axis current component, i_q corresponding to the given torque and speed are calculated by loss minimization algorithm. Actual i_d , i_q currents are regulated to these optimal values by the vector control.

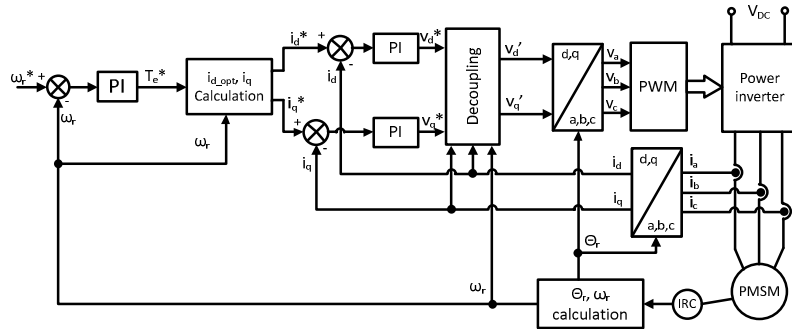


Fig. 5. Block diagram of PMSM vector control with implementation of the loss minimization algorithm.

5. Experimental Results

Overall control system block diagram respecting loss minimization is shown in Fig. 5. Whole control system was implemented in dSPACE for experimental verification of the proposed method. Parameters of interior PMSM used in experiments are in Tab. 1. The negative d-axis current produces a positive reluctance torque, and as a result armature current and copper loss, P_{Cu} are smaller if compared with control where $i_d=0$. Furthermore, the negative d-axis current reduces flux-linkage, and as a result also the iron losses, P_i are reduced.

Results obtained by experiments are shown in Fig. 6 and Fig. 7. Motor accelerates to nominal speed, than at time 0,4s nominal load torque is applied. Electrical losses for loss minimization control and ordinary vector control with $i_d=0$ are compared in Fig. 6.b. In Fig. 7 i_d , i_q current waveforms for loss minimization control and for $i_d=0$ are shown.

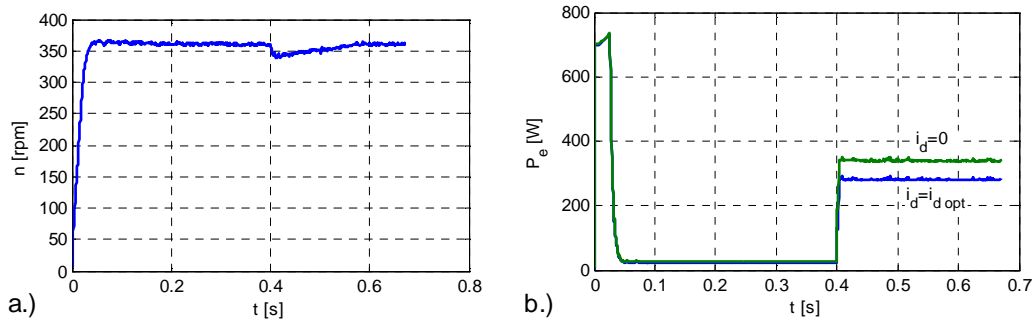


Fig. 6. a.) Motor speed response. b.) Electrical losses comparison.

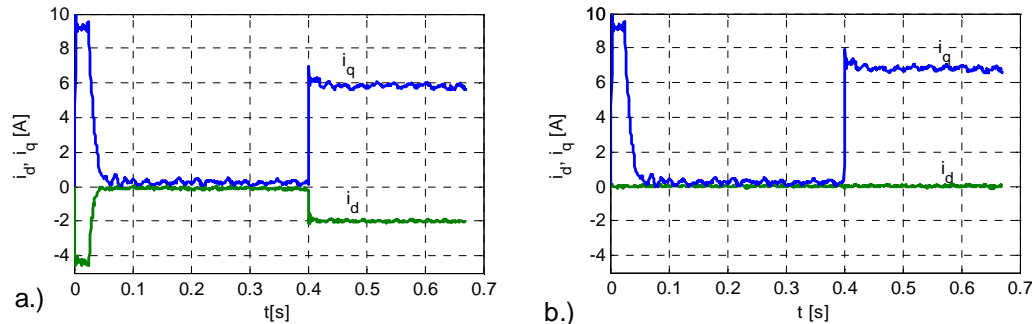


Fig. 7. a.) d, q-axes currents response for loss minimization control. b.) d, q-axes currents response for $i_d=0$ control.

6. Conclusion

PMSM loss minimization control technique was described and verified. This method was implemented via dSPACE control system. Loss minimization control strategy shows lower electrical losses, P_e at nominal load condition (about 60W) if compared with ordinary zero d-axes current control. As a result of losses reduction the motor efficiency was increased by 2.2% .

Acknowledgement

The authors wish to thank for support the Slovak Grant Agency VEGA 1/0355/11.

References

- [1] URASAKI, N., SENJYU, T., UEZATO, K. *An Accurate Modeling for Permanent Magnet Synchronous Motor Drives*, IEEE Transaction on Industrial Electronics, 0-7803-5864, 2000
- [2] SENJYU, T., KUWAE, Y., URASAKI, N., UEZATO, K. *Accurate Parameter Measurement for High Speed Permanent Magnet Synchronous Motors*, IEEE Transaction on Industrial Electronics, 0-7803-7067-8, 2001
- [3] MORIMOTO, S., TONG, Y., TAKEDA, Y., HIRASA, T. *Loss minimization control of permanent magnet synchronous motor drives*, IEEE Transaction on Industrial Electronics, No. 5, October 1994
- [4] CAVALLARO, C., DI TOMMASO, A. O., MICELI, R., RACITI, A., RICCO GALLUZZO, G. *Analysis a DSP implementation and experimental validation of a loss minimization algorithm applied to permanent magnet synchronous motor drives*, IEEE Industrial Electronic Society, April 2004



On the Analysis of Arterial Branching

Stefan Borik, Ivo Cap

University of Zilina, Faculty of Electrical Engineering, Department of Electromagnetic and Biomedical Engineering, Univerzitna 1, 010 26 Zilina, Slovak Republic, {stefan.borik, ivo.cap}@fel.uniza.sk

Abstract. This article deals with principles and dependences of arterial branching. It presents overview of theories which describe various principles causalities of arterial bifurcations. In this work detailed analysis of principle of minimum work and principle of minimum drag is performed and there are derived optimal arterial branching angles at symmetrical arterial bifurcation if assumed principle of minimum drag application.

Keywords: angle, arterial, bifurcation, branching, friction, shear stress, vessel.

1. Introduction

When we take a look back at the past we can find many authors pursuing after clarification of cardiovascular system functionality. We can find also the authors interested in research of arterial branching. The first steps were performed by [1], [2]. Murray assumed that arterial branching depends on the principle of the minimum work. On the other hand there are works dealing with principle of minimum blood volume [3], principle of minimum drag [4] or we can find also works based on the fractal properties of arterial branching [5], [6]. In this article we focus on the main aspects of these works.

2. Principle of minimum work

The principles of any physiological organization are based on the principle of minimum resources expended on its function. The principle of minimum work proposed by [1] assumes that the work needed for maintenance of blood flow and for cost of blood volume tends to be a minimum.

The blood is viscous fluid which is propagated from heart through arteries and the power needed for maintenance of blood flow and for cost of blood volume can be calculated as proposed Murray [1] from Poisseuille law:

$$p = \frac{8fl\eta}{\pi r^4}. \quad (1)$$

By multiplying both sides of equation (1) by flow f and adding $B = b \cdot l \cdot \pi \cdot r^2$ which represents power needed for maintenance of blood volume, we get equation for total power P . The cost of blood is represented by b .

$$P = pf = \frac{8f^2l\eta}{\pi r^4} + B. \quad (2)$$

We obtain condition for minimum needed power by first derivative calculation:

$$\frac{dP}{dr} = -\frac{32f^2l\eta}{\pi r^5} + 2b\pi lr = 0 \quad (3)$$

Then blood flow f can be expressed:

$$f^2 = \frac{b\pi r^6}{16\eta} \Rightarrow f = k r^3 \quad (4)$$

It follows that flow f is proportional to third power of blood vessel radius and this proportionality is called as Murray law for arterial branching when the work or power needed for maintenance of blood flow and for cost of blood volume tends to be a minimum. Arterial branching can be by this law expressed by the next equation:

$$r^3 = r_1^3 + r_2^3, \quad (5)$$

where r is radius of mother vessel which branches to 2 daughter vessels with radii r_1 and r_2 [1].

3. Principle of minimum drag

Another attempt to description of arterial branching principles can be found in work [7]. Author of this work introduces another view to arterial branching and assumes that arterial bifurcations are related to shear stress caused by blood flow in arteries. Shear stress can be expressed from Poisseuille law (see equation (1)) [4], [8]:

$$\tau = \frac{4\eta f}{\pi r^3} \quad (6)$$

Total shear force T on a vessel segment of length l is than defined:

$$T = 2\pi r l \tau = \frac{8\eta f l}{r^2} = t l \quad (7)$$

where t is shear force per unit length of a vessel.

A mother vessel with radius r_0 in cardiovascular system branches to two daughter vessels with radii r_1 and r_2 . Total shear force T described in equation (7) consists of components T_0 , T_1 and T_2 . Theory of minimum drag is based on assumption that junction point at arterial bifurcation is not tethered to another tissue but the single vessels are tethered to the tissue in certain distance from this point l_0 , l_1 and l_2 . Position coordinates of junction points are x , y and position of tethered places are x_0 , x_1 , x_2 and y_0 , y_1 , y_2 . The mother vessel bifurcation is shown in Fig. 1.

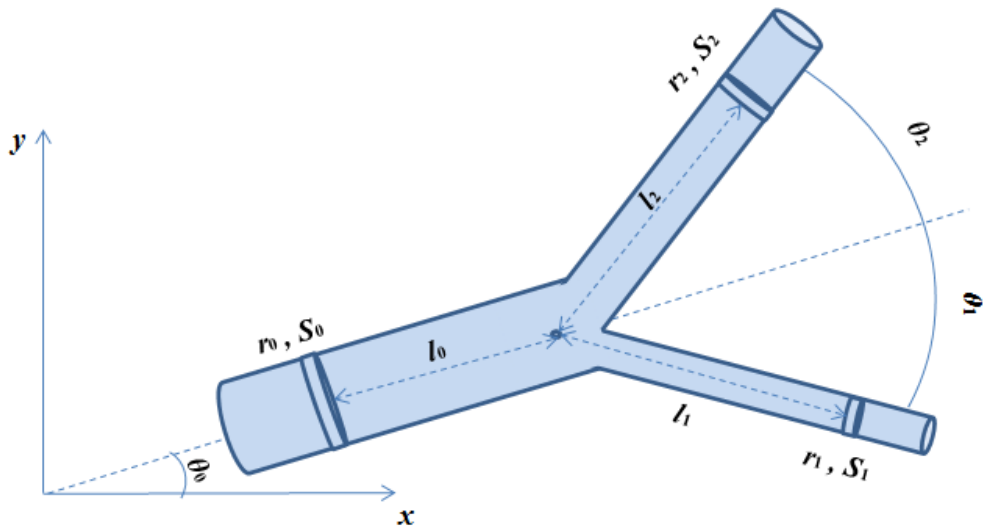


Fig. 1. Arterial bifurcation

As in the text above total shear force consists of vector sum of three components. By using geometrical relations it can be expressed by the following equations [4]:

$$T = t_0 l_0 + t_1 l_1 + t_2 l_2 \quad (8)$$

$$T = t_0 \sqrt{(x-x_0)^2 + (y-y_0)^2} + t_1 \sqrt{(x-x_1)^2 + (y-y_1)^2} + t_2 \sqrt{(x-x_2)^2 + (y-y_2)^2} \quad (9)$$

Minimal shear force condition can be obtained by its partial deriving according to space coordinates x , y which is similar procedure to Murray's work [1]. Equaling partial derivatives to zero we get equations for optimal branching geometry [4]:

$$2 \cos \theta_1 = \frac{R_1^2}{F_1} + \frac{F_1}{R_1^2} - \frac{F_2^2 R_1^2}{F_1 R_2^4} \quad (10)$$

$$2 \cos \theta_2 = \frac{R_2^2}{F_2} + \frac{F_2}{R_2^2} - \frac{F_1^2 R_2^2}{F_2 R_1^4} \quad (11)$$

where R and F are non-dimensional ratios of radii and flows defined as follows:

$$R_1 = \frac{r_1}{r_0}, \quad R_2 = \frac{r_2}{r_0} \quad (12)$$

$$F_1 = \frac{f_1}{f_0}, \quad F_2 = \frac{f_2}{f_0} \quad (13)$$

In case of symmetrical bifurcation, if $R_1 = R_2 = R$ and $F_1 = F_2 = 0.5$, equations (10) and (11) can be rewritten to the next forms:

$$\cos \theta_1 = R_1^2 \quad (14)$$

$$\cos \theta_2 = R_2^2 \quad (15)$$

Graphical interpretation of equations (14) and (15) is shown in the next figure:

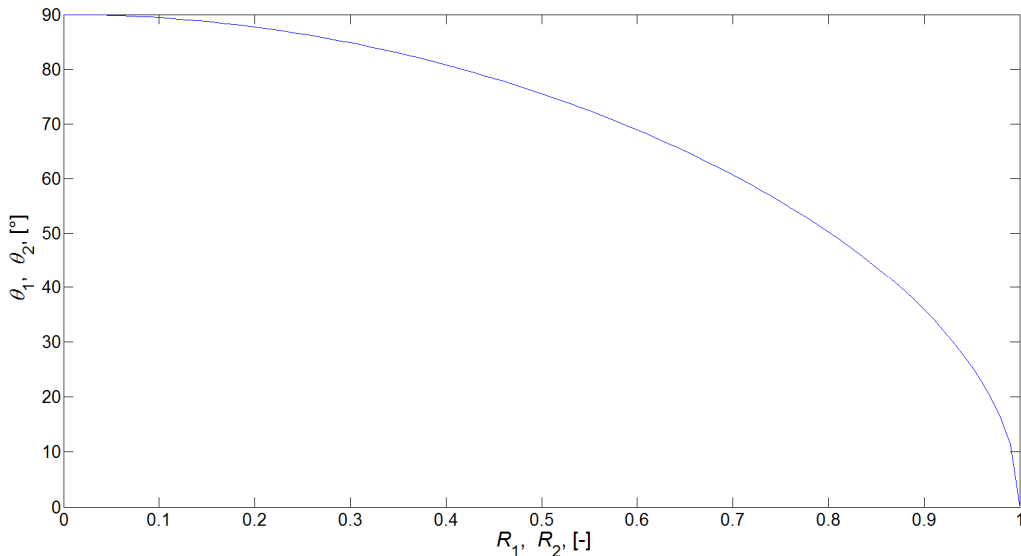


Fig. 2. Optimal arterial branching angle at symmetrical bifurcation

4. Conclusion

Within this article we analyzed two principles of arterial branching. The first principle was Murray's principle of minimum work [1]. The second principle was proposed by Zamir and its name is principle of minimum drag [4], [7]. By analysis of this principle the optimal arterial branching angles were derived. Optimality of branch angles depends on criteria of minimum drag which effects on arterial walls as shear force or shear stress. In case of symmetrical bifurcation equations for branching angles were derived, which are dependent on mother and daughter vessel radii [4], [7]. For example values of ratios of radii corresponding to bifurcation angles $\theta_1 = \theta_2 = 45^\circ$ are 0.84. This value corresponds to daughter vessel which radius is 70.7 % of mother vessel. Our future work will be focused on comparison of real measured data with theoretical results and implementation of non-symmetrical arterial branching to model of arterial system based on electromechanical analogy.

References

- [1] MURRAY, Cecil D. *The physiological principle of minimum work: I. The vascular system and the cost of blood volume*. Proceedings of the National Academy of Sciences of the United States of America, 1926, 12.3: 207.
- [2] MURRAY, Cecil D. *A relationship between circumference and weight in trees and its bearing on branching angles*. The Journal of General Physiology, 1927, 10.5: 725-729.
- [3] KAMIYA, A., TOGAWA, T. *Optimal branching structure of the vascular tree*. Bulletin of Mathematical Biology, 1972, 34.4: 431-438.
- [4] ZAMIR, M. *The role of shear forces in arterial branching*. The Journal of general physiology, 1976, 67.2: 213-222.
- [5] ZAMIR, M., et al. *On fractal properties of arterial trees*. Journal of theoretical biology, 1999, 197.4: 517-526.
- [6] ZAMIR, M. *Arterial branching within the confines of fractal L-system formalism*. The Journal of general physiology, 2001, 118.3: 267-276.
- [7] ZAMIR, M. *Shear forces and blood vessel radii in the cardiovascular system*. The Journal of general physiology, 1977, 69.4: 449-461.
- [8] WESTERHOF, N., STERGIOPULOS, N., NOBLE, M. *Law of Poiseuille*. Snapshots of Hemodynamics, 2010, 9-14.

Nomenclature

μ	=	blood viscosity
b	=	cost of blood
B	=	power needed for maintenance of blood volume
f	=	blood flow
F	=	flow ratio
l	=	vessel length
p	=	blood pressure
P	=	power
r	=	vessel radius
R	=	radii ratio
T	=	shear force
t	=	shear force per unit length
x, y	=	position coordinates
Θ	=	branching angle
τ	=	shear stress



Evaluation of excessive transmission line losses caused by compact fluorescent lamps

*Klemen Deželak, *Gorazd Štumberger

*University of Maribor, Faculty of Electrical Engineering and Computer Science, Power Laboratory,
Smetanova ulica 17, 2000 Maribor, Slovenia, {klemen.dezelak, gorazd.stumberger}@uni-mb.si

Abstract. In sense of using electricity more efficiently the number of the installed compact fluorescent lamps is increased, nowadays. Those compact fluorescent lamps have large impact on the power factor and consequently on the excessive losses in transmission lines, as well as on the voltage and current total harmonic distortion. In this paper aforementioned excessive losses in three-phases systems, loaded by different compact fluorescent lamps, are evaluated with orthogonal decomposition of currents. In that sense, the main impact is dedicated on the asymmetrical loading of phases in such a three-phase system.

Keywords: Orthogonal decomposition, compact fluorescent lamps, excessive losses, power factor.

1. Introduction

Possible solution for using electricity more efficiently is by using compact fluorescent lamps (CFLs) and light emitting diodes (LEDs) instead of conventional incandescent lamps [1]. A single CFL consumes approximately only one-third of electrical energy as an incandescent lamp, while providing the same light output [2]. Therefore, by using CFLs, consumers can save a large amount of money in the long-run with the reduced energy cost compared [2]. Because electronic ballasts of CFLs are nonlinear and consequently the current waveform that is rich in higher harmonics components is drawn [1]. This harmonic current flowing through the network causes a high power quality issues, especially in sense of the increased losses and the voltage waveform distortion [1]. Therefore, CFLs can produce severe problems on the distribution systems, like unacceptable voltage distortion levels [3], [4], destruction of power-factor capacitors and the malfunction of equipment [1], [4].

The main objective of this paper is to analyze the increased excessive losses in the three-phase low voltage lines where the loads are represented by CFLs. These losses depend on the root mean square (RMS) values of current and the load power [5] - [8], while for evaluation of excessive losses the orthogonal decomposition of currents is applied [6], [9]. Basically, this paper is related to [7], where instead of single-phase system, the entire research is performed for three-phase system. Therefore, the asymmetrical loaded phases, with higher current and voltage harmonic components, and their impact on total excessive losses are dealt within the proposed paper.

2. Orthogonal decomposition of currents

Firstly, the voltage and current vectors of three-phase system are represented together with the inner product. In such a way, the current vector component indispensable for energy transmission and the generalized power factor of the three-phase system are defined [6], [10].

Let $i_1(t)$, $i_2(t)$, $i_3(t)$ and $u_1(t)$, $u_2(t)$, $u_3(t)$ be the line currents and voltages of a three-phase system observed inside a selected time window $[0, T]$. Let us introduce the current vector $\mathbf{i}(t)$ and the voltage vector $\mathbf{u}(t)$ by (1).

$$\mathbf{i}(t) = \begin{bmatrix} i_1(t) \\ i_2(t) \\ i_3(t) \end{bmatrix}, \quad \mathbf{u}(t) = \begin{bmatrix} u_1(t) \\ u_2(t) \\ u_3(t) \end{bmatrix} \quad (1)$$

The inner product of current and voltage vectors is defined by (2), that is equal to total power of whole system P [10].

$$(\mathbf{u}, \mathbf{i}) = \frac{1}{t_2 - t_1} \int_{t_1}^{t_2} \mathbf{u}^T \mathbf{i} d\tau = \frac{1}{t_2 - t_1} \int_{t_1}^{t_2} (p_1(\tau) + p_2(\tau) + p_3(\tau)) d\tau = P_1 + P_2 + P_3 = P \quad (2)$$

In (2) p_1 , p_2 and p_3 stand for the instantaneous values of power in all three phases. Let us introduce root mean square values of the current vector I and voltage vector U by Euclidean norms of these vectors (3) and (4).

$$I^2 = \|\mathbf{i}\|^2 = \frac{1}{t_2 - t_1} \int_{t_1}^{t_2} (i_1(\tau)i_1(\tau) + i_2(\tau)i_2(\tau) + i_3(\tau)i_3(\tau)) d\tau \quad (3)$$

$$U^2 = \|\mathbf{u}\|^2 = \frac{1}{t_2 - t_1} \int_{t_1}^{t_2} (u_1(\tau)u_1(\tau) + u_2(\tau)u_2(\tau) + u_3(\tau)u_3(\tau)) d\tau \quad (4)$$

Therefore, the equivalent conductivity G of entire three-phase system is defined by (5) [10].

$$G = \frac{P}{U^2} \quad (5)$$

The G is required to define the current vector \mathbf{i}_u (6) that is collinear with applied voltage vector \mathbf{u} and is the only current vector indispensable for energy transmission [10].

$$\mathbf{i}_u = G\mathbf{u} = \frac{P}{U^2} \mathbf{u} \quad (6)$$

The generalized power factor of the three-phase system PF' can be now defined by (7). Finally, the square of generalized power factor, actually $1/PF'^2$, can be used as a measure for excessive transmission losses [6], [10].

$$PF' = \frac{|P|}{\|\mathbf{u}\| \|\mathbf{i}\|} \quad (7)$$

3. Numerical model based results

All results presented in this section are obtained by numerical model realized, described and confirmed by an appropriate measurements in paper [7]. In such a case the main output results of numerical model are the root mean square value of current, the power factor and the root mean square value of the current indispensable for energy transmission. Analysis is performed with two different compact fluorescent lamps, denote by CFL 1 and CFL 4 [7]. Voltages and currents waveforms, with proper higher order harmonics components for both are shown on Figs. 1 - 2. Additionally Fig. 3 shows current waveforms, where in each phase there are ten CFLs included. Afterwards, the system from Fig. 3 was modified, firstly in each phase five CFL 1 and five CFL 4 lamps were included - consequently symmetrical system were obtained (Fig. 4a). Secondly in the first phase ten CFL 1, in the second phase ten CFL 4, while in the third phase 5 CFL 1 and five CFL 4 lamps were included - asymmetrical system (Fig. 4b). Numerical values for each of aforementioned cases are shown in Tab. 1.

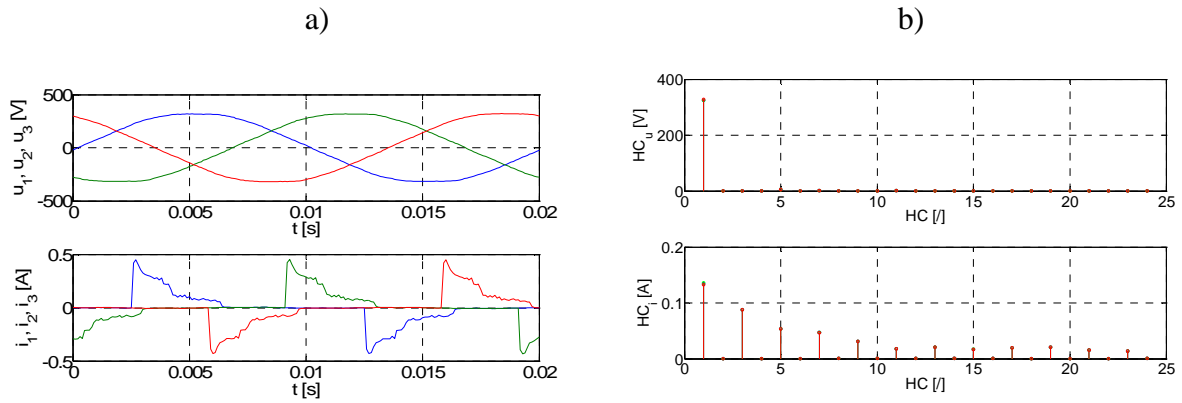


Fig. 1. Time dependent voltage and current waveforms of 3×1 CFL 1 a), and appropriate harmonic components b).

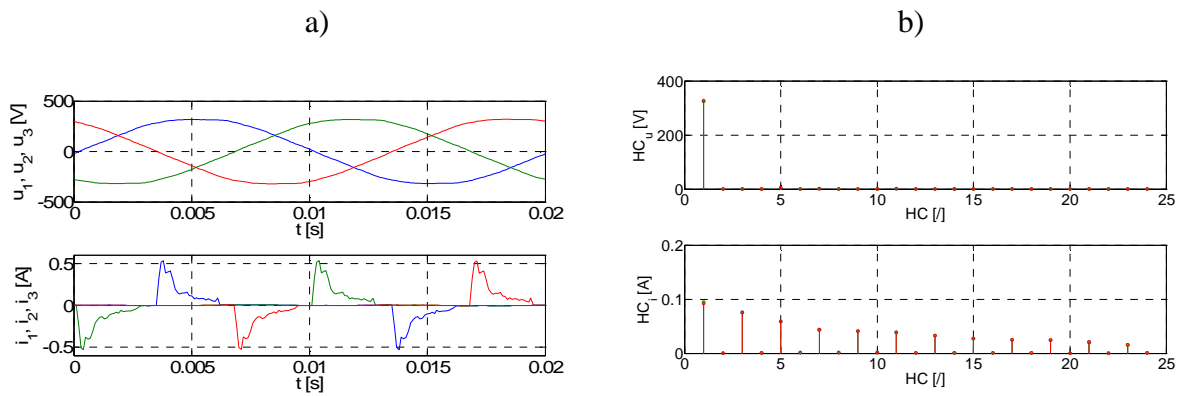


Fig. 2. Time dependent voltage and current waveforms of 3×1 CFL 4 a), and appropriate harmonic components b).

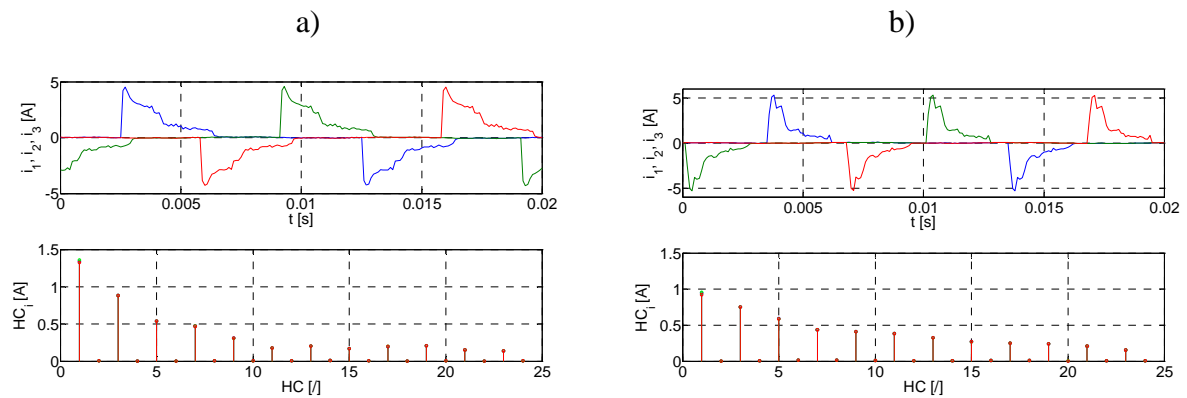


Fig. 3. Time dependent current waveforms and appropriate harmonic components of 3×10 CFL 1 a) and 3×10 CFL 4 b).

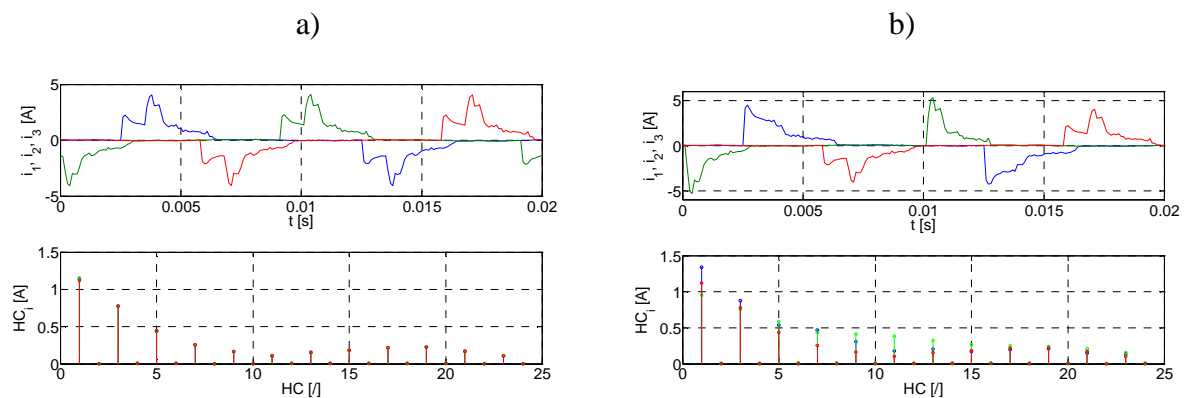


Fig. 4. Time dependent current waveforms and appropriate harmonic components of 3×5 CFL 1 + 3×5 CFL 4 symmetrical a) and asymmetrical b).

Case	Fig. 1	Fig. 2	Fig. 3a	Fig. 3b	Fig. 4a	Fig. 4b
P [W]	59.3	44.1	592.9	440.9	512.9	513.2
U [V]	398.8	398.8	398.7	398.7	397.7	397.7
I [A]	0.231	0.206	2.312	2.058	1.919	2.101
PF' [/]	0.644	0.538	0.643	0.537	0.672	0.614

Tab. 1. Calculated values of power, voltages, currents and generalized power factors.

It is obvious that CFL 1 has quite better generalized power factor of the three-phase system PF' as CFL 4 (0.644 versus 0.538). For example, in case of 3×10 CFL 1 the losses which cannot be avoided are equal to 0.534 W, while in case of 3×10 CFL 4 those are 0.424 W. In both cases we proposed ohmic resistance 0.1Ω [7]. In the first case the excessive losses are equal to 0.756 W, while in second case those are much higher 1.044 W, that is because of lower PF' . Additionally is shown, that combination of different CFLs could even improve the value of power factor and consequently reduced excessive transmission line losses [7]. In our case excessive losses are reduced to 0.447 W. Otherwise, the asymmetrical connected CFLs with different characteristics, leads to the increased excessive transmission line losses. In the proposed case to 0.728 W.

4. Conclusion

This paper evaluates excessive transmission line losses caused by nonlinear loads as compact fluorescent lamps are, connected to three-phase system. Basically, from the presented generalized power factor, of the three-phase system, it is obvious that excessive transmission line losses could be reduced if symmetrical loading of three phases system is applied. Ratio excessive losses divided by losses which cannot be avoided could be improved from 1.4 and more to 1.2. In case of asymmetrical loading aforementioned ratio is increased, in our case to approximately 1.7.

References

- [1] WATSON, N. R., SCOTT, T. L., HIRSCH, S. J. J., *Implications for Distribution Networks of High Penetration of Compact Fluorescent Lamps*, IEEE Transactions on Power Delivery, Vol. 24, No. 3, pp. 1528 - 1528, July 2009.
- [2] LAM, J., JAIN, P. K., A Simple Single Switch Electronic Ballast for Compact Fluorescent Lamps with Passive Power Factor Correction (PFC) and Soft Switching Capability, IECON 2012 - 38th Annual Conference on IEEE Industrial Electronics Society, pp. 4503 - 4508, October 2012.
- [3] CUNILL-SOLA, J., SALICHS, M., *Study and Characterization of Waveforms From Low-Watt (<25W) Compact Fluorescent Lamps With Electronic Ballasts*, IEEE Transaction on Power Delivery, Vol. 22, No. 4, pp 2305-2311, October 2007.
- [4] BLANCO, A. M., PARRA, E. E., *Effects of High Penetration of CFLs and LEDs on the Distribution Networks, Harmonics and Quality of Power (ICHQP)*, 14th International Conference, pp 1-5, September 2010.
- [5] CZARNECKI, L. S., SWIETLICKI, T., *Powers in nonsinusoidal networks: Their interpretation, analysis, and measurement*, IEEE Transactions on Instrumentation and Measurement, Vol. 39, pp. 340-345, 1990.
- [6] ŠTUMBERGER, G., POLAJŽER, B., TOMAN, M., DOLINAR, D., *Orthogonal decomposition of currents, power definitions and energy transmission in three-phase systems treated in the time domain*, Proceedings of the International conference on renewable energies and power quality (ICREPQ' 06), Spain, 2006.
- [7] DEŽELAK, K., SUKIČ, P., ŠTUMBERGER, G., *Impact of Compact Fluorescent Lamps on the Excessive Transmission Line Losses*, Proceedings of the International conference on renewable energies and power quality (ICREPQ' 12), Spain, 2012.
- [8] KHAN, N., ABAS, N. *Comparative study of energy saving light sources*, Renewable and Sustainable Energy Reviews, Vol 15, pp. 296 - 309, 2011.
- [9] CZARNECKI, L. S., *Orthogonal Decomposition of the Currents in a 3-Phase Nonlinear Asymmetrical Circuit with a Nonsinusoidal Voltage Source*, IEEE Transactions on Instrumentation and Measurement, Vol. 37, pp. 30-34, 1988.
- [10] DEŽELAK, K., ŠTUMBERGER, G., *Evaluation of excessive transmission line losses caused by unbalanced and nonlinear three-phase loads*, Proceedings of the International conference on renewable energies and power quality (ICREPQ' 08), Spain, 2008.



Dielectric properties of transformer oil with dispersed magnetic nanoparticles

*Jozef Drga, *Peter Bury

*University of Žilina, Faculty of Electrical Engineering, Department of Physics, Univerzitná 1, 01026 Žilina, Slovak Republic, jozef.drga@fel.uniza.sk

Abstract. This contribution deals with the investigation of a magnetic fluid based on the transformer oil Mogul placed in a magnetic field using dielectric spectroscopy. Dielectric parameters of the magnetic fluid were measured at frequency 1MHz and the magnetic field linearly increased up to 200 mT and then decreased to zero both during 1 hour. The tangent of the loss angle ($\text{tg } \delta$), the real and imaginary parts of permittivity were studied at a temperature 18°C. The observed results are discussed and compared with results observed by acoustic spectroscopy with regard to structural changes that occur in magnetic fluid.

Keywords. dielectric spectroscopy, magnetic fluid, transformer oil, magneto-dielectric effect

1. Introduction

Magnetic fluids (ferrofluids) are colloidal suspensions of magnetic nanoparticles covered by a surfactant in a base liquid. The magnetic nanoparticles usually of diameter 5 – 30 nm are magnetic monodomains [1]. They are mostly ferrites (oxides of iron). These magnetic fluids exhibit many fascinating phenomena. They are used in many applications in technic area and medicine. The choice of the base liquid and the surfactant depends on the purpose for which the suspension is used. Water or physiologic solution are used as base liquids in medicine applications. Some medicine applications are for example drug transport, hyperthermy, nuclear magnetic resonance etc. [2]. Important kinds of these fluids are magnetic fluids based on transformer oils as base liquids. These magnetic fluids used in transformers as a cooling medium improve the cooling efficiency compared to the case when a pure transformer oil is used. The magnetic nanoparticles suspended in a transformer oil have significant influence on dielectric breakdown [3].

The magneto-dielectric effect has been studied in various works theoretically [4] and experimentally [5]. The magnetic nanoparticles and the magnetic field affect the real and imaginary part of the permittivity and the tangent of the loss angle, as well. Many theories of the magneto-dielectric effect are based on the supposition of elliptical shape of the nanoparticles, postulated orientation of magnetic moments along the major axis of the ellipsoid and that there occurs no agglomeration into clusters. In this contribution the results observed by dielectric spectroscopy of magnetic fluid based on transformer oil Mogul are discussed and compared with structural changes obtained by acoustic spectroscopy [6].

2. Experimental

For our study of the magneto-dielectric effect in magnetic fluids we used an experimental arrangement (Figure 1) consisting of the electromagnet, the RLC meter Quadtech 7600 Plus, the magnetic field meter, the measuring cell with temperature stabilization and computer that managed the source of current for the electromagnet. The sample holder (a capacitor), shown of Figure 2, that was constructed just for the investigated magnetic fluids, allowed to measure dielectric parameters of high resistivity fluids and also enabled to change the angle between magnetic and electric fields.

The RLC meter is suitable for measuring the electrical (dielectric) parameters at frequencies in the range of 10 Hz – 2MHz. The thermostat ensured the temperature stabilization in the range of 15 – 35 °C with accuracy $\pm 0,1$ °C. The computer program developed on Department of Physics was used for collecting, storing and analyzing the measured data from RLC meter. For our investigation the 1 % magnetic fluid with diameter of nanoparticles $d \approx 11$ nm (manufactured from $\text{Fe}_2\text{O}_3 \cdot \text{FeO}$ – magnetite), the oil acid as surfactant and transformer oil Mogul as base liquid were used. The basic properties of this magnetic fluid, such as the density and saturation were equal to 0.85 g/cm^3 and 5,3 mT. The electric field was parallel to magnetic field and all measurements were carried out at temperature 18°C.

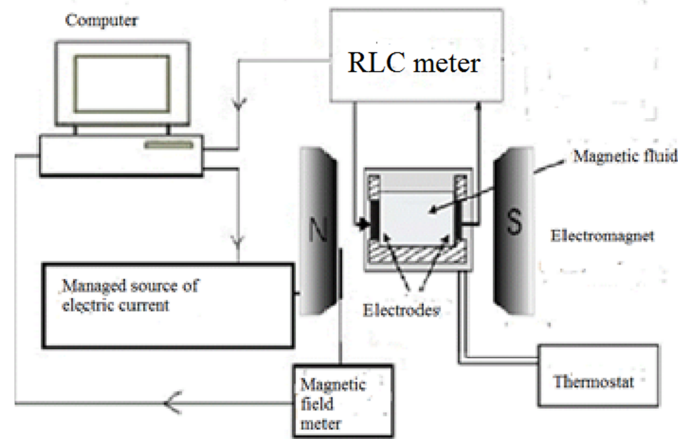


Fig. 1.The experimental arrangement

The measured dielectric parameters were real and imaginary part of the permittivity ϵ_r' and ϵ_r'' , respectively, that enable also the calculation of the tangent of loss angle. The real part of the relative dielectric permittivity ϵ_r' is given by the formula

$$\epsilon_r' = \frac{C}{C_0}, \quad (1)$$

where C is the capacity of the capacitor with the sample placed between holder electrodes and C_0 is the capacity of empty capacitor. For investigation of the imaginary part of the permittivity ϵ_r'' the relation

$$\epsilon_r'' = \frac{1}{\omega \cdot R \cdot C_0} \quad (2)$$

was used. The symbol ω represents the angular frequency of the electric field, R is the resistivity of the sample. The tangent of the loss angle ($\text{tg } \delta$) is obtained using then the relation

$$\text{tg } \delta = \frac{\epsilon_r''}{\epsilon_r'} \quad (3)$$

3. Results and discussion

Figure 3 shows our first measured dependence of the real part of the permittivity and the tangent of the loss angle on magnetic field. The magnetic field was linearly increased from 0 up to 200 mT during 1 hour

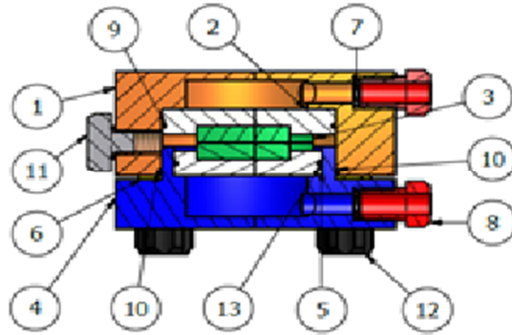


Fig. 2. The sample holder (capacitor): 1.Top part 2. Insulator, 3.Electrodes, 4. Bottom part, 5.Upside insulator, 6. Distance circle, 7. Gasket ring 7, 8. Passage screw, 9.,10.,12.,13. Gasket rings, 11.Plug,

The dependence of ϵ_r' and $\text{tg } \delta$ on the magnetic field decreasing at the same rate is shown, too. The increase of the magnetic field caused a slow increase of both ϵ_r' (maximum at ~ 100 mT, Fig. 2a) and the $\text{tg } \delta$ with two maxima (Fig. 3b) at ~ 90 mT and ~ 140 mT. In the case of decreasing magnetic field also the maximum at ~ 90 mT at $\text{tg } \delta$ dependence (ϵ_r' curve shows maximum at ~ 140 mT) was observed. The maxima are connected with the formation of clusters (chains) from nanoparticles residing near the electrodes [7]. These clusters reduce the effective distance between the electrodes and the effect of increasing the real part of the permittivity occurred. Similar effect was observed in case of the dependence of $\text{tg } \delta$.

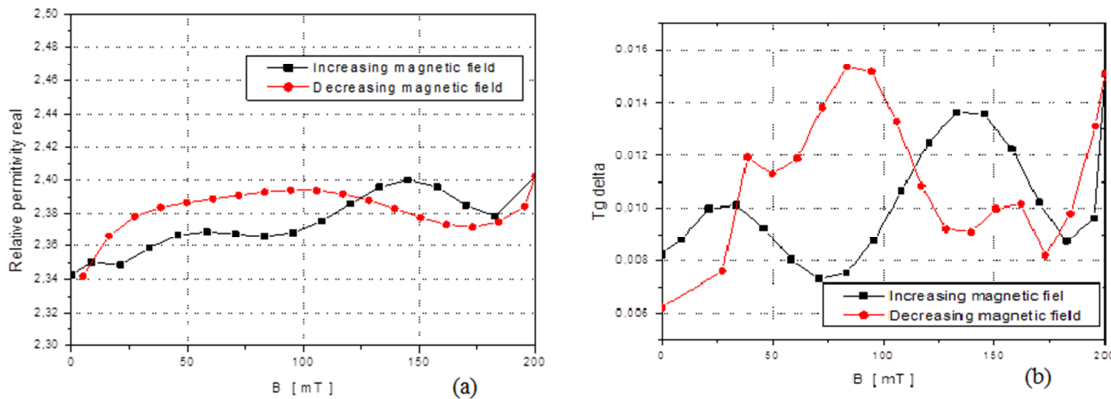


Fig.3. Dependence of real part of permittivity (a) and tangent of loss angle (b) on magnetic field

We can suppose that the maxima and minima of both curves are connected with structural changes in the created chains related to ellipsoidal shape of the nanoparticles. Fig. 4 shows the dependence of acoustic attenuation on the magnetic field [8] measured at the temperature 16°C . The changes of the attenuation with both increasing and decreasing magnetic field that have very similar character as our measurements of dielectric parameters are connected to the progressing aggregation of magnetic nanoparticles in clusters. The following decrease of the acoustic attenuation (ϵ_r' and $\text{tg } \delta$) is caused by clusters destruction by thermal Brown motion [9]. The existence of the two maxima is probably a consequence of further reconstruction of the magnetic fluid structure.

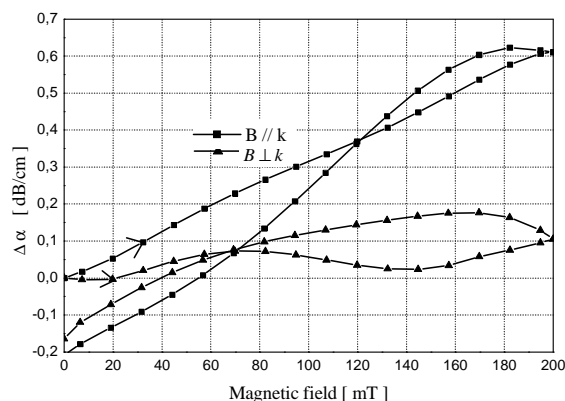


Fig. 4. The dependence of the acoustic attenuation on magnetic field with magnetic field parallel (■) and perpendicular (▲) to wave vector.

4. Conclusion

The interaction between the magnetic moments of nanoparticles and the biasing magnetic field leads to the creation of long chains – clusters. The presented results show that the structural changes represented by the cluster creation can be detected by the dielectric spectroscopy as well as acoustic spectroscopy. The magneto – dielectric effect can then be related to the elliptical shape of the nanoparticles and the presence of the clusters.

Acknowledgement

The authors wish to thank for the support to R&D operational program Centre of excellence of power electronics systems and materials for their components II. No. OPVaV-2009/2.1/02-SORO, ITMS 26220120046 funded by European regional development fund (ERDF).

References

- [1] ODENBACH, S. *Ferrofluids - magnetically controlled suspensions*, Colloids and Surfaces A: Physicochemical and Engineering Aspects, vol. 217, p. 171-185, 2003
- [2] LEAMY, P. J. *A dissertation*, University of Florida, 2003
- [3] KOPČANSKÝ, P., TOMČO, L., MARTON, K., KONERACKÁ, M., POTOČOVÁ, I., TIMKO, M. *The experimental study of the DC dielectric breakdown strength in magnetic fluids*, Journal of Magnetism and Magnetic Materials, vol. 272-276, Part 3, p. 2377-2401, 2004
- [4] COUPER C., MARIN, C.N., FANNIN, P: C. *Biasing Field effect on Microwave Dielectric Properties of Magnetic Fluids*, Physics Procedia vol. 9. p. 58 -62, 2010
- [5] TIMKO M., KOPČANSKÝ, P., MOLČAN, M., TOMČO, L., MARTON, K., MOLOKAC, S., RYBAR, P., STOJAN, F., HOLOTESCU, S., TACULESCU, A. *Magnetodielectric properties of Transformer Oil Based Magnetic Fluids*, Acta Physica Polonica A, vol 121, no.5- 6, p. 1253 – 1256, 2012
- [6] HOCKICKO, P.: *High Frequency Acoustic Spectroscopy of Perspective Materials for Electrotechnics*, Acoustics vol. 17. no. 1, p. 10-17, 2012
- [7] KÚDELČÍK, J., BURY, P., KOPČANSKÝ, P., TIMKO, M. *Dielectric breakdown in mineral oil ITO 100 based magnetic fluid.*, Physics Procedia, vol. 9, p. 78-81, 2010
- [8] KÚDELČÍK J., BURY P., DRGA, J., ZÁVIŠOVÁ, V., TIMKO, M., KOPČANSKÝ P. *Structure properties of transformer oil based magnetic fluid*, Physic of the materials 2012, Proceedings of international conference, Košice, p. 63 -67, 2012
- [9] JOZEF CZAK, A., SKUMIEL, A., LABOWSKI, M.: *Effects of biocompatible coating of nanoparticles on acoustics property of the magnetic fluid*, Journal of Magnetism and Magnetic Materials, vol.290, p. 265-268, 2005



Influence of Phase Winding Faults on Switched Reluctance Motor's Operation

*Peter Dubravka, *Pavol Rafajdus, *Valeria Hrabovcova, *Marek Musak

*University of Žilina, Faculty of Electrical Engineering, Department of Power Electrical Systems, Univerzitna 2, 01026 Žilina, Slovak Republic, {peter.dubravka, pavol.rafajdus, valeria.hrabovcova, marek.musak}@fel.uniza.sk

Abstract. This paper deals with phase winding electrical faults of Switched Reluctance Motor (SRM). The static parameters of SRM are obtained by Finite Element Method (FEM) and verified by measurements. The static parameters of SRM as phase inductance, flux linkage and torque of defined phase winding are investigated for health and fault motor by FEM and they are used in dynamic simulations. The dynamic simulations of health SRM and SRM under fault conditions are compared.

Keywords: Switched Reluctance Motor, Finite Element Method, Fault conditions

1. Introduction

The Switched Reluctance Motor (SRM) belongs to the simplest electrical machines. SRM is characterized by robustness and the manufacturing costs are lower in comparison with others electrical machines [1].

The SRM has simple construction. It is electrical machine which has salient poles on both the rotor and the stator. The two coils are wound on opposite stator poles and excited simultaneously, see Fig. 1a. It leads to the generation of the magnetic flux. The torque is produced by tendency of its moveable part (rotor) to move into a position where the inductance of the excited winding is maximized [2].

Many applications require drive reliability which is very important from the point of view of fault operation. During the SRM operation can occur mechanical, magnetical or electrical fault. In [3], [4], [5], there are some studies of electrical faults which can be: short circuit in one coil of a phase (all turns or some turns), a whole coil is bridged by a short circuit, the whole phase is short circuited, open circuit in one coil of a phase, a short circuit between two different phases, a short circuit from one winding to ground.

In this paper, the static and dynamic faults of real 12/8 SRM, 540V, 3000 rpm, 3700W, where each phase comprises four coils connected in series, are investigated by simulations for health and fault operated SRM. The specific faults are: one, two and three short circuited coils of phase winding and one opened coil. The static parameters of health and fault SRM are obtained by finite element method and used in dynamic simulations.

2. Mathematical model of SRM

For the mathematical model of SRM static parameters are needed as input parameter because of solving transients. The static parameters obtained by means of FEM and verified by measurement are: phase inductance, flux linkage and electromagnetic torque [6], [7]. These parameters are used in dynamic simulations to calculate following variables: phase current, speed, voltage and dynamic torque during normal and fault condition.

The mathematical model of SRM consists of following equations, if: leakage inductances between phases are neglected, iron losses are neglected, phase inductance and torque depends on phase current and rotor position.

The voltage equation of one phase is:

$$v = Ri + \frac{d\psi}{dt} \quad (1)$$

where R is phase resistance, i is phase current and ψ is flux linkage. The flux linkage depends on both parameters: phase current and rotor position ($\psi = f(i, \Theta)$).

The phase current is calculated from:

$$\frac{di}{dt} = \frac{v - \left(R + \frac{dL(i, \Theta)}{d\Theta} \omega \right) i}{L(i, \Theta)} \quad (2)$$

where L is phase inductance and ω is angular speed.

The angular speed is calculated from equation:

$$\frac{d\omega}{dt} = \frac{1}{J} \left(\sum_{j=1}^m T_j(\Theta, i) - T_{load} \right) \quad (3)$$

where J is the moment of inertia and T_{load} is load torque.

The SRM is controlled on the base of rotor position Θ , therefore it is as following:

$$\Theta = \int \omega dt \quad (4)$$

3. Dynamic simulations of health SRM and SRM with winding faults

The dynamic simulation was created under Matlab software. The model of one SRM phase is shown in Fig. 1b.

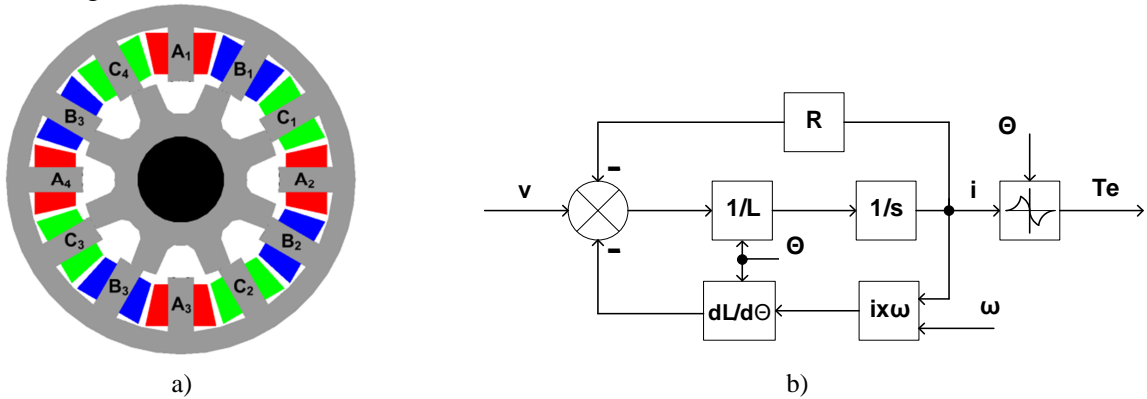


Fig. 1. SRM: a) cross section area, b) model of one SRM phase.

The PI controller in discrete version is used for control of rotor speed. The control signal is given as:

$$u(k) = K_p [e(k) + \frac{T}{T_i} \sum_{i=0}^{k-1} e(i)] \quad (5)$$

where k is a discrete time instant, K_p is a proportional gain e is an error and T is a sampling time.

For the current control a hysteresis controller was used. The phase voltage in (1) is given by DC voltage source, which supplied the converter of SRM. By this control strategy the voltage can have three values, if the voltage drops on the transistors and diodes of power converter are neglected:

- a) $v = +V_s$, if the phase current i is lower than low limit of the hysteresis value,
- b) $v = 0$, if the phase current is higher than high limit of the hysteresis value,
- c) $v = -V_s$, if the phase current is switched off

The control structure which was used in order to simulate SRM's transients is shown in Fig. 2. The coefficients of PI controller were tuned by trial and error method.

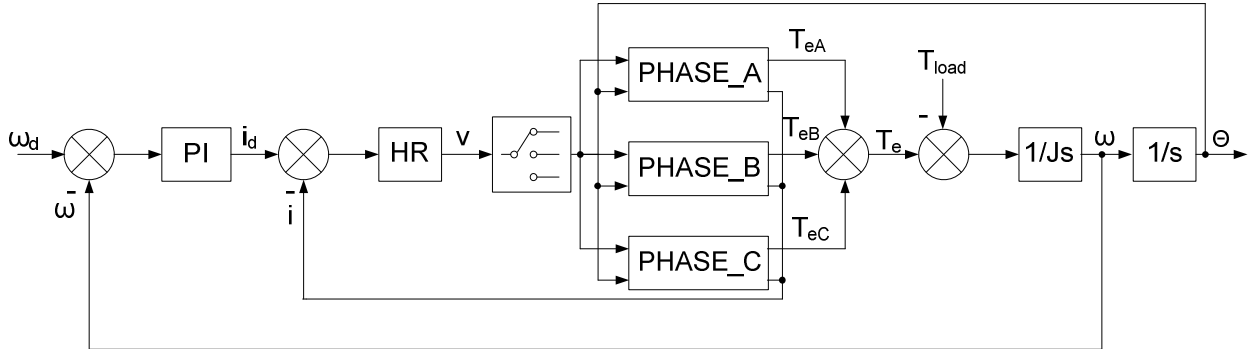


Fig. 2. The block diagram of SRM speed control.

The simulations of SRM with health phase winding – zero short circuited coils (0 CS), one, two, three short circuited coil (1 CS), (2 CS), (3 CS) and one open phase (1 OF) were done respectively. Fig. 3 shows waveforms of phase currents, torque and speed during normal operation and in time 0,0465s the three coils of phase A has been short circuited. From this Fig.3 seems to be current in phase A higher and torque lower. It is caused by low inductance of the phase A and only one fourth of phase A winding contributes to the generation of electromagnetic torque.

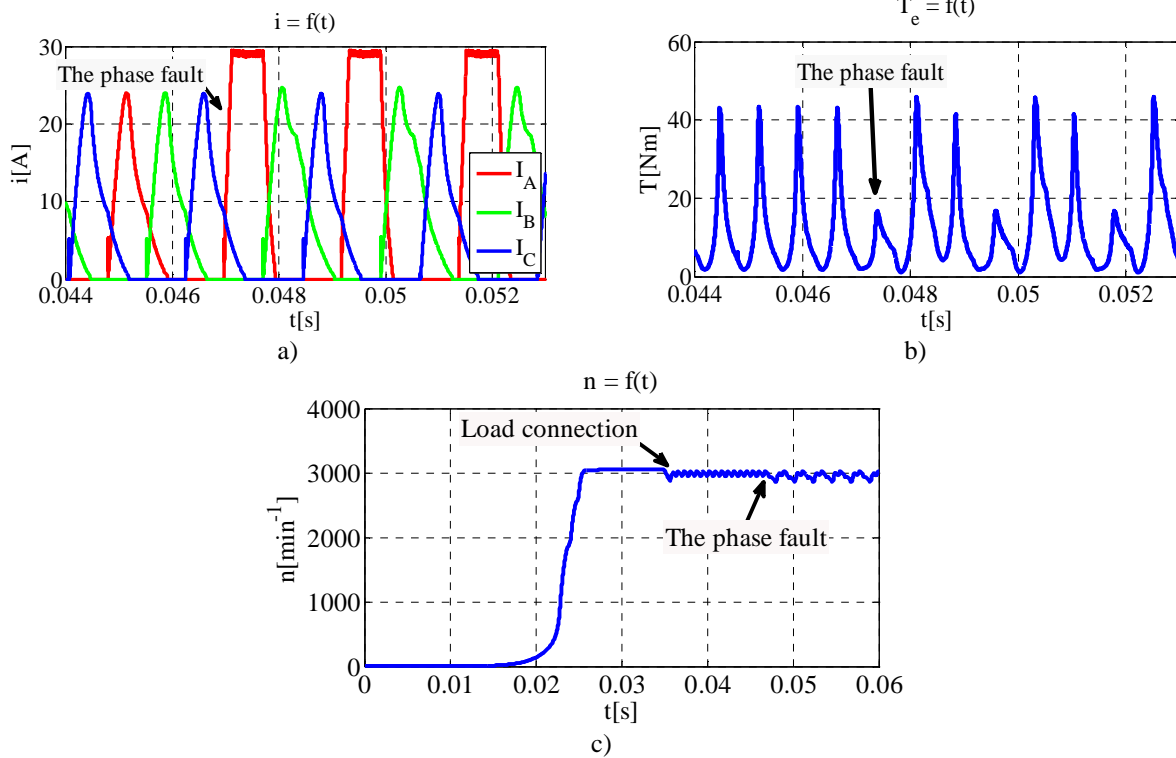


Fig. 3. SRM waveforms: a) phase currents, b) torque, c) speed

For better comparison of all defined faults, torque and speed ripple has been calculated. Torque ripple is calculated according:

$$\Delta T_e = \frac{T_{eMAX} - T_{eMIN}}{T_{eAV}}. \quad (6)$$

where T_{eMAX} is maximum value of torque, T_{eMIN} is minimum value of torque and T_{eAV} is average value of torque calculated from:

$$T_{eAV} = \frac{1}{T} \int_0^T T_e dt. \quad (7)$$

The speed ripple was calculated by the same way.

The results are shown in Fig. 4. It can be seen that speed and torque ripple of SRM under fault condition with one and two coils short circuited is comparable with the health one. The torque and speed ripple is more noticeable when the three coils of one phase are short circuited and the worst case is for one open phase.

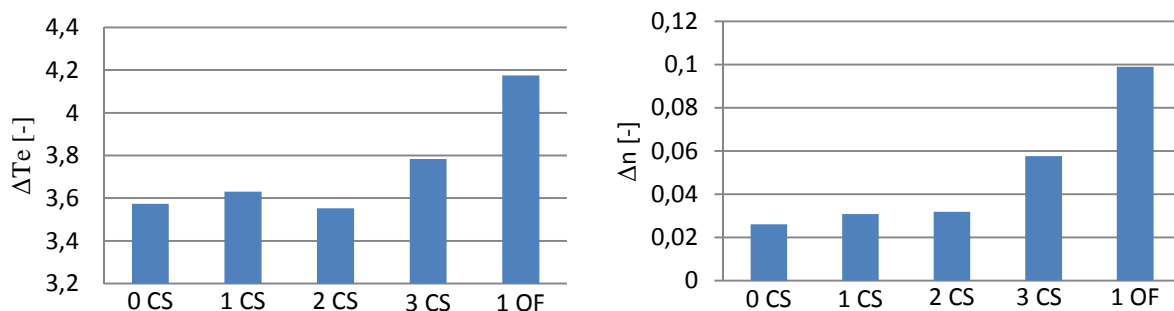


Fig. 4. a) Torque ripple with respect to number of short circuited coils, b) Speed ripple with respect to number of short circuited coils.

4. Conclusion

In this paper the analysis of phase winding electrical faults and their influence on the SRM operation has been presented. The SRM static parameters were calculated by means of FEM for health SRM and SRM under defined fault conditions. The parameters were used in dynamic simulation created from mathematical model of SRM. Torque and speed ripple was investigated according the number of short circuited coils of phase and for one open phase.

Through simulation results there can be proposed some solutions for safety increase when this type of faults will occur.

Acknowledgement

This work was supported by the VEGA (Scientific Grant Agency of the Slovak Republic) No.1/0940/13.

References

- [1] T.J.E. Miller, *Electronic Control of Switched Reluctance Machines*. Oxford (U.K.): Newnes, 2001.
- [2] Pyrhonen, J.; Jokinen, T.; Hrabovcova, V.: *Design of rotating electrical machines*, John Wiley & Sons, 2008
- [3] B. Schinnerl and D. Gerling, "Analysis of winding failure of switched reluctance motors," in Proceedings of the IEEE International Electric Machines and Drives Conference (IEMDC '09), Miami (USA), pp. 738-743.
- [4] Loránd SZABÓ, Mircea RUBA: *On Fault Tolerance Increase of Switched Reluctance Machines*, EUROCON 2009, 18-23 May 2009
- [5] Kacanka, V., Rafajdus, P., Makys, P., Vavrus, V., Szabo, L.: Static and Dynamic Fault Analysis of Switched Reluctance Motor, International conference ELEKTRO 2012, Rajecke Teplice, May 2012, Slovakia, IEEE Xplore
- [6] Pavol Rafajdus, Valeria Hrabovcova, Peter Hudak: *Investigation of Losses and Efficiency in Switched Reluctance Motor*, EPE-PEMC 2006, Portoroz, Slovenia
- [7] Rafajdus P., Sekerak P. Kalamen L., Hrabovcova V., Chen H.: *Static and Dynamic Analysis of Linear Switched Reluctance Machine*, Communications – Scientific Letters of the University of Žilina, 4/2011



Fitting memristor models to observed behavior of TiO₂ memristors

*Milan Frátrik, *Štefan Badura, *Lucie Žoltá

*University of Žilina, Faculty of Management Science and Informatics, Department of InfoComm Networks, Univerzitná 8215/1, 01026 Žilina, Slovak Republic, {milan.fratrik, stefan.badura, lucie.zolta}@fri.uniza.sk

Abstract. Memristors may find their use in many applications – mainly as memory or logic, fuzzy systems or neuromorphic systems. High amount of scientific papers shows that the research of memristors recently draws a lot of attention. This paper presents the theoretical overview of memristors and it is followed by measurements of these elements. This paper can be divided into two parts. The first part describes existing memristor models, based on memristive system definition. The second part focuses on the measurements of memristors and finding the parameters for the selected model.

Keywords: memristor, memristor models, modeling, measurement, fitting.

1. Introduction

It has been a long time since Leon O. Chua published his article [1] where the fourth passive two-terminal electrical component – memristor. Memristor should represent the relation between electric charge (q) and magnetic flux linkage (φ) (1).

$$d\varphi = M dq \quad (1)$$

The first memristors were developed a long time ago for several times, but the scientists did not know, that they had developed a memristor [12]. The scientists had been looking for material for many years, which could represent the relation in equation (1). HP team led by R. S. Williams invented memristor, because he had not been searching for a device, which has charge – magnetic flux relation, but they had been searching for a device which is a resistor with a state. This work was published in [3] and it contains the first relations for memristor modeling. A memristive system defined in [2] is formally represented by (2) and (3).

$$v(t) = R(w, i) \cdot i(t) \quad (2)$$

$$\frac{dw}{dt} = f(i) \quad (3)$$

The memristor models based on TiO₂ may be divided into two categories. Into the first category belong models, where two regions of oxide and doped oxide are represented as two resistors in series with common slider (see Fig.1). Models, with more complicated physical model represent the second category [10].

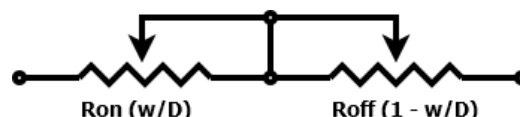


Fig. 1. The basic physical model of memristor.

2. Memristors models

2.1. Linear Ion Drift Model

As it was mentioned in introduction, this model had been published for the first time in [3]. It is derived from the physical properties of the device, developed in HP laboratories. A device with width D contains two regions. The first region with width w (state variable) has high concentration of dopants (oxygen vacancies of TiO_{2-x}), while the second region ($D - w$) is TiO_2 [3]. This device is shown in Fig. 2. The basic assumption is that conductance, ion drift and the ions have equal average ion mobility μ_v . Then the equations of memristive system can be written in form (4), (5).

$$v = \left(R_{ON} \frac{w(t)}{D} + R_{OFF} \cdot \left(1 - \frac{w(t)}{D} \right) \right) \cdot i \quad (4)$$

$$\frac{dw}{dt} = \mu_v \frac{R_{ON}}{D} \cdot i(t), \quad (5)$$

where R_{ON} is the resistance in state $w(t) = D$ and R_{OFF} is resistance in state when $w(t) = 0$.

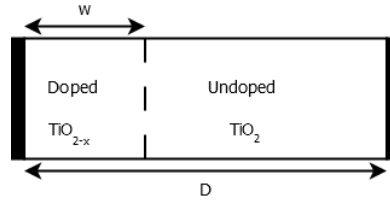


Fig. 2. Linear Ion Drift model.

2.1.1. Window Functions

Obviously from the previous model, the state variable can achieve values from the interval $\langle 0, D \rangle$. If the state variable should be in the interval $\langle 0, 1 \rangle$, the equation (2) must be multiplied with so called window function g (6) or (7) in case of Biolek window.

$$\frac{dw}{dt} = g(w) \cdot f(i) \quad (6)$$

$$\frac{dw}{dt} = g(w, i) \cdot f(i) \quad (7)$$

The simplest way is to multiply the equation (3) with a rectangular window. Another possibility is to influence the velocity of the change of state variable close to the bounds, because this function is nonlinear – nonlinear ion drift phenomenon is present. In Tab. 1, window functions are shown.

Window name	Joglekar [4]	Biolek [5]	Prodromakis [6]
Window function	$g(w) = 1 - \left(\frac{2w}{D} - 1 \right)^{2p}$	$g(w, i) = 1 - \left(\frac{w}{D} - \text{stp}(-i) \right)^{2p}$	$g(w) = j \cdot \left\{ 1 - \left[\left(\frac{w}{D} - 0.5 \right)^2 + 0.75 \right]^p \right\}$
Parameters	p – integer	p – integer	j – real p – integer

Tab. 1. Window functions.

2.2. Nonlinear Ion Drift Model

When the memristors were measured, the scientists found out that the linear model or model completed by window function does not fulfill the needed properties. The main deficiencies are: the

switching speed between R_{ON} and R_{OFF} states, the absence of threshold and the symmetry in these models.

Nonlinear Ion Drift Model is a mathematical model, using which the authors [15] could fit experimental values. The equation (8) can be divided into two parts. The first part (*sinh*) is active when the device is in state ON and the state variable is close to 1. The second part (*exp*) is active when the device is in state OFF and the state variable is close to the 0. The second equation looks similarly to the ideal diode model.

$$i(t) = w(t)^n \cdot \beta \cdot \sinh(\alpha \cdot v(t)) + \chi \cdot (\exp(\gamma \cdot v(t)) - 1), \quad (8)$$

where $\alpha, \beta, \gamma, \chi$ are fitting constants as real numbers and n is integer value. The state drift derivative (10) was proposed in [9].

$$\frac{dw}{dt} = a \cdot g(w) \cdot \sinh(b \cdot v(t)), \quad (9)$$

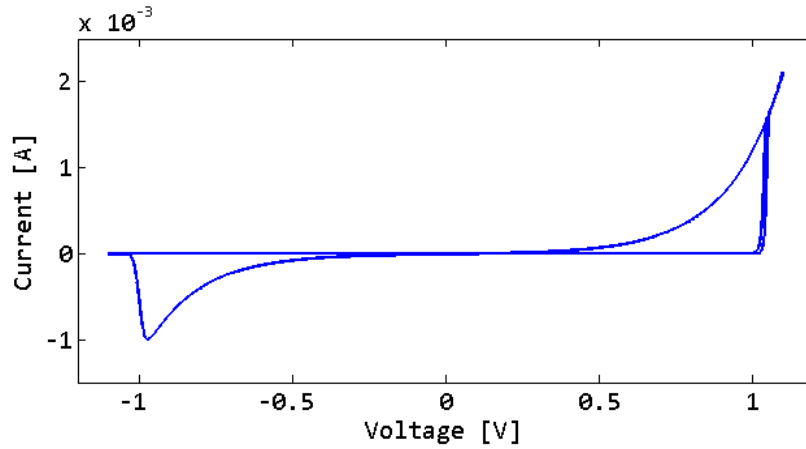


Fig. 4. V-I characteristics of Nonlinear Ion Drift Model. Parameters: $\alpha=5.6, \beta=9, \chi=0.01, \gamma=4, n=6, a=17.9, b=15$. Sinusoidal input voltage, $f=1\text{MHz}$, $V_{pp} = 2.2\text{V}$

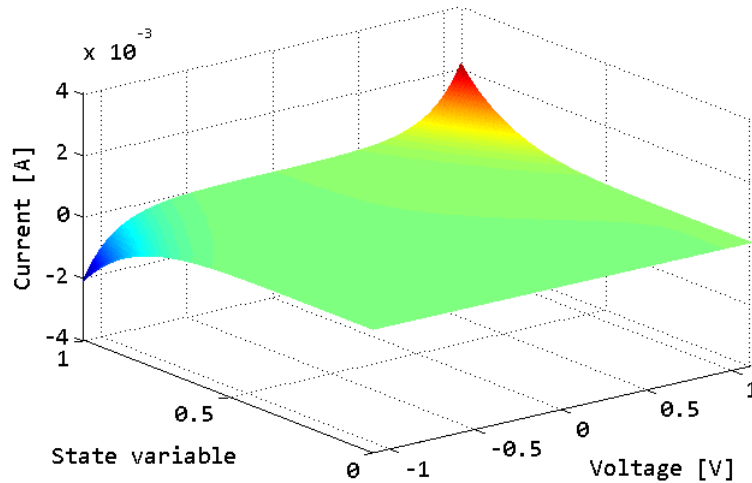


Fig. 5. Current depends on the state variable and input voltage, with the same parameters as in Fig 4.

2.3. Simmons Tunnel Barrier Model and TEAM

Simmons tunnel barrier model is the first model, which assumes more complicated inner structure as two resistors connected in series [11]. It is the most accurate physical model of memristive device [10]. The modeling equations are more complicated than in previous models. Only block structure will be represented for this model in next figure – Fig. 6.

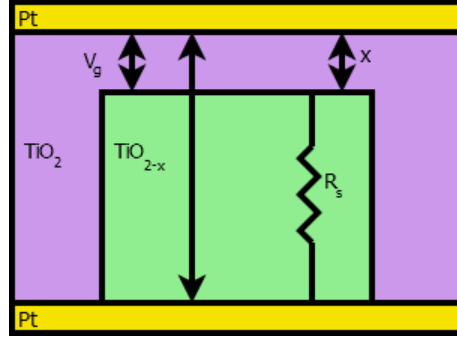


Fig. 6. Physical model of Simmons tunnel memristive device.

Because of the Simmons Tunnel Barrier Model is too complicated and the simulation is computationally complex, the TEAM (ThrEshold Adaptive) model has been developed and it behaves the same way as Simmons Tunnel Barrier Model. The state variable derivate is defined as:

$$\frac{dx(t)}{dt} = \begin{cases} k_{off} \cdot \left(\frac{i(t)}{i_{off}} - 1 \right)^{a_{off}} \cdot f_{off}(x), & 0 < i_{off} < i \\ 0, & i_{on} < i < i_{off} \\ k_{on} \cdot \left(\frac{i(t)}{i_{on}} - 1 \right)^{a_{on}} \cdot f_{on}(x), & i < i_{on} < 0 \end{cases} \quad (10)$$

where k_{on} , k_{off} , a_{off} , a_{on} are constant, i_{off} and i_{on} is current threshold and x is the internal state variable. Functions f_{off} and f_{on} are window functions [10]. Thus memristance is dependent on tunneling effect the V-I relation is defined according to (2) in terms

$$v(t) = R_{ON} \exp\left(\frac{\lambda}{x_{off} - x_{on}}(x - x_{on})\right) \cdot i(t), \quad (11)$$

where λ is a fitting parameter and R_{ON} and R_{OFF} are resistance at the bounds.

3. Measurements and their relation to models

The measurements of memristive devices took place at Ilmenau University of Technology. Those measurements were done in laboratory environment using Keithley 4200-SCS Semiconductor Characterization System with three SMUs (Source–measurement unit). The measurements were done for both single and double structures. Double structure is shown in Fig 7. Anti-parallel connected memristors (double structures) can be used as *min* or *max* operators [13], depending on their polarity. Large memristor network, with those connections, can be used in different areas i.e. in tasks of signal processing – audio-visual speech recognition [17].

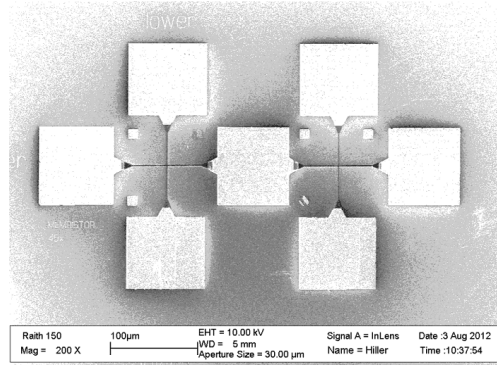


Fig. 7. Measured double memristor structure.

3.1. Basic measurement

All structures were measured using triangle wave as voltage input at first. Using these measurements, it was possible to identify if the measured V-I characteristics looks like pinched hysteresis loop (memristive device) or not. In Fig. 8 results obtained for a “good” structure are shown.

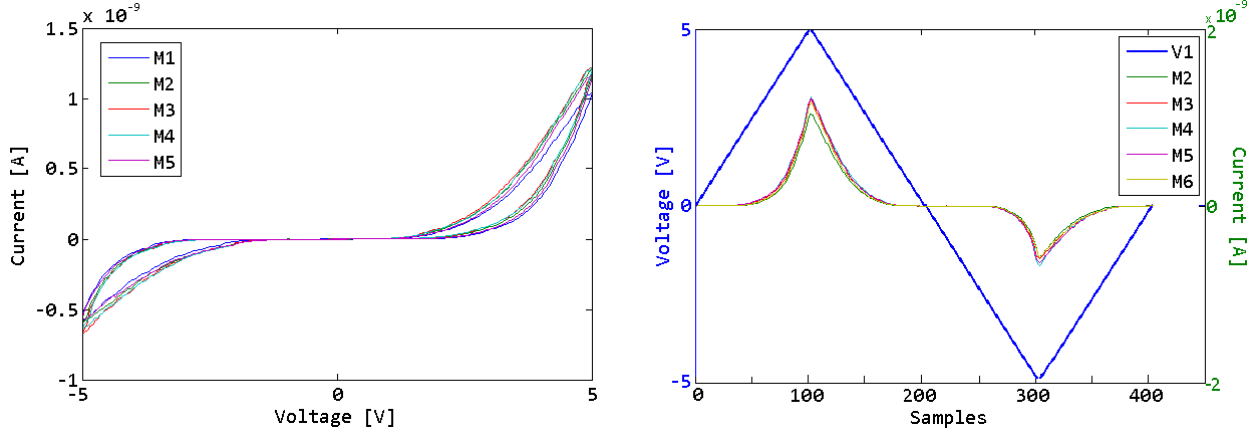


Fig. 8. V-I characteristics – pinched hysteresis loop on the LHS and the measurement in time domain on RHS

Except for the basic measurements using triangle wave, some more measurements with rectangular voltage on some selected devices have been executed. The measurement took long time at the constant value which leads to gradual degradation of the built conductive channel. This fact is one of characteristic properties of bipolar memristors. These measurements were later modified to staircase function and its modifications. The results of experiments with rectangular input and staircase function are shown in Fig. 9.

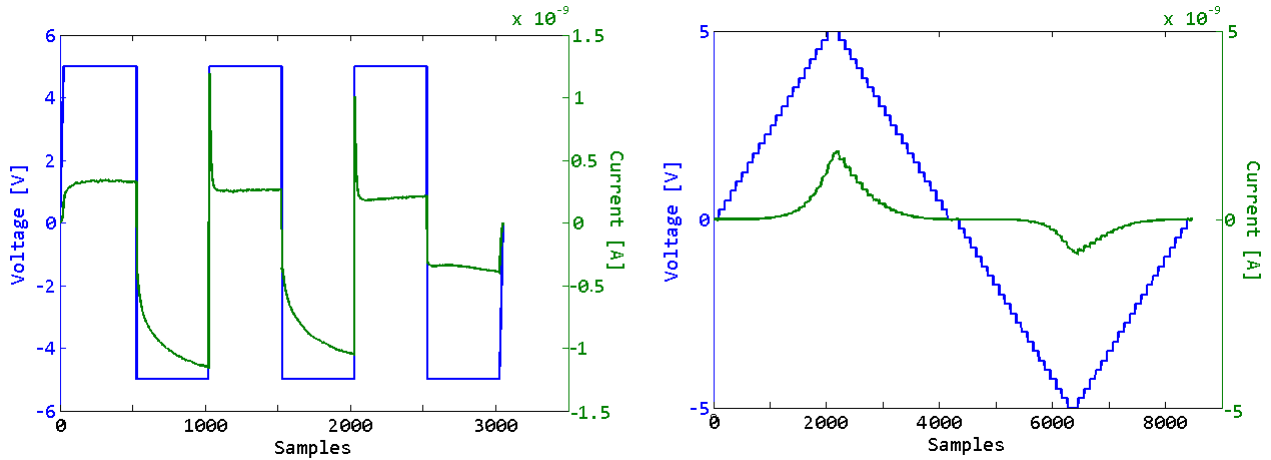


Fig. 9. V-I characteristics – pinched hysteresis loop on the LHS and the measurement in time domain on RHS

3.2. Finding appropriate model to the measured values

The device does not respond to input voltage levels below certain threshold as shown in measurements results provided in Fig. 8. Based on this fact it is obvious, that linear models are absolutely unsatisfactory. Maybe the most universal model is the Nonlinear Ion Drift Model, with lots of fitting parameters. Using these, it is possible to influence dynamic properties as well as threshold value.

Data used for fitting were from the measurements with modified staircase function. The part of data, where built conductive channel is degraded was neglected. For the purpose of finding right parameters, a simple GUI application was programmed. Using this application it is possible to set and modify all necessary parameters.

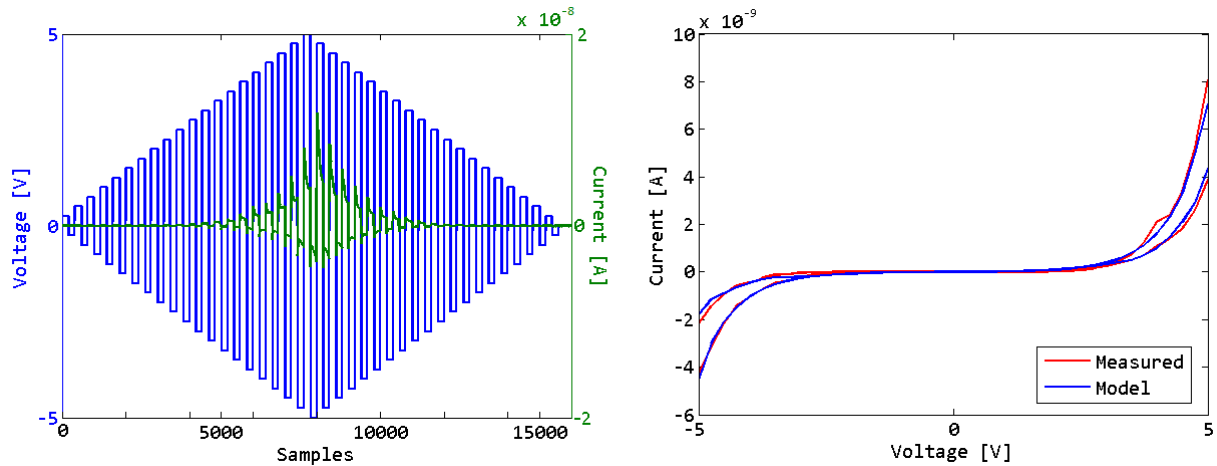


Fig. 10. On LHS there is the modified staircase function with measured values. On RHS is fitted function. Fitting parameters for (8) and (10): $\alpha=1.4$, $\beta=13.4$, $\chi=1.4$, $\gamma=1.5$, $n=0.6$, $a=1.25$, $b=2.4$.

4. Conclusion

As Fig. 10 shows we have succeeded in finding such model parameters. These parameters describe measured values sufficiently. When the polarity of voltage is changed, the current value starts at the same value where it stopped. The switching in OFF- \rightarrow ON direction takes longer time than switching in ON- \rightarrow OFF direction. The main defect of those structures is a small ratio between R_{ON} and R_{OFF} – Fig. 9. – 1:2.5.

Fitting results and acquired data shows that the Nonlinear Ion Drift Model allows fitting of more kinds of memristive devices produced in different ways. This mathematical model is much simpler than the physical model, but allows considerably good approximation of the device behavior for simulation purposes. Another advantage of this model is its simple simulation for large memristor networks.

Acknowledgement

Research stay at Ilmenau University of Technology was financed by the IPID program. Thanks to the Institute of Micro- and Nanotechnologies at TU Ilmenau.

References

- [1] CHUA, L. O. *Memristor – The Missing circuit Element*. IEEE Transactions on Circuit Theory, Vol. CT-18, No. 5, pp. 507-519, 1971
- [2] CHUA L.O., KANG S. M. *Memristive Devices and Systems*. Proceedings of the IEEE, Vol. 64, No. 2, pp. 209-223, 1976
- [3] STRUKOV, D. B., SNIDER G. S., STEWART D. R., WILLIAMS R. S. *The missing memristor found*. Nature, Vol. 453, pp. 80-83. 2008
- [4] JOGLEKAR Y. N., WOLF S. J. *The elusive memristor: Properties of basic electrical circuits*. Eur. J. Phys., Vol. 30, No. 4, 2009
- [5] BIOLEK Z., BIOLEK D., BIOLKOVA V. *SPICE model of memristor with nonlinear dopant drift*. Radioengineering, Vol. 18, No. 2, pp. 210–214, 2009
- [6] PRODROMAKIS T., PEH B. P., PAPAVALASSILIOU C., TOUMAZOU C. *A Versatile Memristor Model with Non-linear Dopant Kinetics*. IEEE Transactions on Electron Devices, Vol. 58, No. 9, pp. 3099-3105, 2011
- [7] YANG J. J., PICKETT M. D., LI X., OHLBERG D. A. A., STEWART D. R., WILLIAMS R. S. *Memristive Switching Mechanism for Metal/Oxide/Metal Nanodevices*. Nature Nanotechnology, Vol. 3, pp. 429-433, 2008
- [8] STRUKOV D. B., WILLIAMS R. S., *Exponential Ionic Drift: Fast Switching and Low Volatility of Thin-Film Memristors*. Applied Physics A: Materials Science and Processing, Vol. 94, No. 3, pp. 515-519, 2009

- [9] LEHTONEN E., LAIHO M. *CNN Using Memristors for Neighborhood Connections*. Proceedings of the International Workshop on Cellular Nanoscale Networks and their Applications, pp. 1-4, 2010
- [10] KVATINSKY S., FRIEDMAN E. G., KOLODNY A., WEISER U.C. *TEAM: ThrEshold Adaptive Memristor Model*. Circuits and Systems I: Regular Papers, IEEE Transactions on, Vol. 60, No.1, pp. 211-221, 2013
- [11] PICKETT M. D., STRUKOV D. B., BORGHETTI J. L., YANG J. J., SNIDER G. S., STEWART D. R., WILLIAMS R. S. *Switching Dynamics in Titanium Dioxide Memristive Devices*. Journal of Applied Physics, Vol. 106, No. 7, pp. 1-6, 2009
- [12] DEARNALEY G., STONEHAM A. M., MORGAN D. V. *Electrical phenomena in amorphous oxide films*. Rep. Prog. Phys. 33, pp. 1129-1191 1970
- [13] KLIMO M., SUCH O. *Memristors can implement fuzzy logic*. arXiv preprint arXiv:1110.2074, 2011
- [14] WASER R. *Nanoelectronics and Information Technology*. 3rd edition, ISBN: 978-3527409273, p. 1040, 2012
- [15] YANG J. J., PICKETT M. D., LI X. M., OHLBERG D. A. A., STEWART D. R., WILLIAMS R. S. *Memristive switching mechanism for metal/oxide/metal nanodevices*. Nature Nanotechnology, Vol. 3, pp. 429-433, 2008.
- [16] PRODROMAKIS T.; TOUMAZOU C. *A review on memristive devices and applications*. Electronics, Circuits, and Systems (ICECS), 2010 17th IEEE International Conference on , pp. 934-937, 2010
- [17] FOLTÁN S. *Speech recognition by means of fuzzy logical circuits*. MENDEL 2012: 18th international conference on soft computing, ISSN 1803-3814, pp. 100-105, 2012.

Optimization of DC/DC Power Converter for Super-capacitor Charging and Discharging

Tomas Haubert, Pavel Mindl

*Czech Technical University in Prague, Faculty of Electrical Engineering, Department of Electric Drives and Traction, Technicka 2, 16627 Praha, Czech Republic, {tomas.haubert, mindl}@fel.cvut.cz

Abstract. The article discusses design of mathematical model of the buck and boost converter from the point of optimal frequency of PWM signal for IGBT control. The converter is dedicated for charging and discharging of hybrid car drive super-capacitor energy storage. The main role of the converter is to optimize energy content in super-capacitor storage used for vehicle acceleration and deceleration. Mathematical model in MATLAB/Simulink has been designed and converter prototype built with Freescale Digital Signal Processor 56F8257. In the end of the article simulated and measured results on the convertor specimen are discussed.

Keywords: DC/DC converter, Hybrid Electric Vehicle, Super-capacitor

1. Introduction

Increasing of living standards increased needs for people transport. Gas emissions and fossil fuel consumption are actual problems for global environment quality on the Earth. Gas emission of car internal combustion engines (ICE) brings many ecological problems in big cities specially. Electric vehicles are tackling this problem, because they do not produce gas emissions. On the board needed electric energy can be stored in batteries, but their disadvantages are limited capacity and inconvenient ratio capacity to mass. Due to driving area of electric vehicles (EV) is lower to compare with vehicles equipped by ICE. The compromise between vehicles driven by ICE and EV are hybrid electric vehicles (HEV). HEV combines the ICE and electric motor for motion [1]. The experimental stand of hybrid drive on Department of Electric Drives and Traction has been created. This stand represents the physical model of combined hybrid drive with electric power splitter. The schematic of this stand is depicted in the fig. 1. The parts of this drive are two identical induction motors. The first motor substitutes an ICE. The second motor operates like traction load (BRAKE). The electric power splitter (EPS) is a special synchronous machine, which has two rotating parts - two rotors. The first rotor (internal) contains permanent magnets and is driven by ICE. The second rotor (external) contains three-phase windings, which is connected by brushes to the input of the AC/DC converter. By means of this converter it is possible to control the output DC voltage in range 0 - 500 V. The DC bus is connected to the DC/DC converter for super-capacitor charging or discharging. DC bus followed to the DC/AC inverter. DC/AC inverter supplies traction motor (TM). More information concerning to experimental stand can be find in [2] and [3].

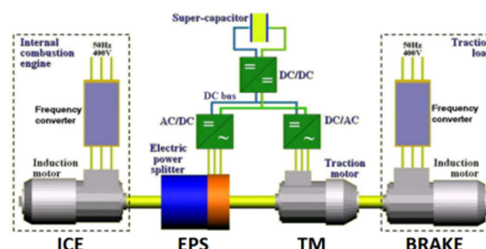


Fig. 1: Schematic of experimental stand of hybrid drive

2. Mathematical Model of Buck/Boost Converter

The DC/DC converter is used for super-capacitor charging and discharging. It is needed to transfer energy from DC bus high side to the super-capacitor low side and in the opposite direction. Therefore converter must be bi-directional. The converter is able to transfer the energy from DC bus higher voltage level V_{PRI} to the super-capacitor lower voltage level V_{SEC} and on the opposite.

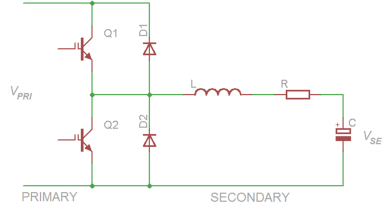


Fig. 2: Schematic of bi-directional DC/DC converter

For controllers design previously models in MATLAB/Simulink has been created. This simulation should test whether it is possible to create the functional model and should present how it will actually work.

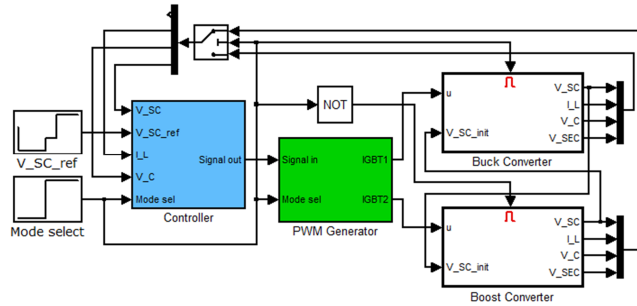


Fig. 3: Model of DC/DC converter in MATLAB/Simulink

The MATLAB/Simulink model is shown in the fig. 3. The model has three main parts. First part represents mathematical models of buck and boost converter. Second part is a PWM generator. The PWM generator transfers reference signal to PWM signal for IGBT transistors. The third part is controller which includes both controllers. The output from this block is signal for PWM generator.

3. Analysis of PWM Frequency for Boost Converter

For switching frequency optimization in boost mode an analysis is needed, if optimal energy amount is stored in the inductor before the transistor is switched off. The circuit, when the transistor Q2 is switched on, can be described by following equations (we are setting the resistor $R = 0$):

$$v_{SC}(t) = \frac{\partial i_L(t)}{\partial t} \cdot L \quad (1)$$

$$-i_L(t) = \frac{\partial v_{SC}(t)}{\partial t} \cdot SC \quad (2)$$

And setting the conditions at the time $t = 0$:

$$v_{SC}(0) = V_0, i_L(0) = 0 \quad (3)$$

The result of this equations are the equations for current through inductor i_L and the voltage on super-capacitor v_{SC} .

$$-i_L(t) = \frac{\sqrt{SC} \cdot V_0 \cdot \sin\left(\frac{t}{\sqrt{SC \cdot L}}\right)}{\sqrt{L}} \quad (4)$$

$$v_{SC}(t) = V_0 \cdot \cos\left(\frac{t}{\sqrt{SC \cdot L}}\right) \quad (5)$$

From equations (4) and (5) we are able to calculate the power which describes how energy is being transferred to inductor.

$$p(t) = v_{SC}(t) \cdot i_l(t) = \frac{\sqrt{C} \cdot V_0^2 \cdot \cos\left(\frac{t}{\sqrt{SC \cdot L}}\right) \cdot \sin\left(\frac{t}{\sqrt{SC \cdot L}}\right)}{\sqrt{L}} \quad (6)$$

The next step is to enumerate the function of mean value of power with dependence on time during the transistor is switched on t_{ON} .

$$P_{MEAN}(t_{ON}) = \int_0^{t_{ON}} \frac{p(t)}{t_{ON}} dt \quad (7)$$

$$P_{MEAN}(t_{ON}) = \frac{C \cdot V_0^2 \cdot \sin\left(\frac{t_{ON}}{\sqrt{SC \cdot L}}\right)}{2 \cdot t_{ON}} \quad (8)$$

The result is plotted in the fig. 4 ($L = 5 \text{ mH}$, $C = 100 \text{ F}$, $V_0 = 50 \text{ V}$).

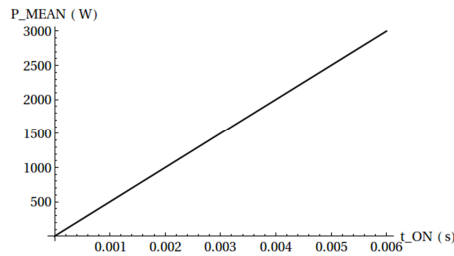


Fig. 4: Graph of power mean value as function t_{ON}

It is clear from the figure, that the maximal time t_{ON} the maximal mean power. At the same time maximal system current must be taken into account. Therefore time $t_{ON} = 0.005\text{s}$ has been used for following calculations. The switching frequency of boost mode is $f = 100\text{Hz}$.

4. Prototype of DC/DC Converter and Experimental Results

The specimen of DC/DC converter was developed for simulation results validation. The control algorithm is programmed in Freescale Digital Signal Processor using processor board of Freescale TOWER System. Freescale TOWER System is modular development platform with possibility to combine different processor platforms and different peripheral modules. The processor is equipped by 56F8257 processor.

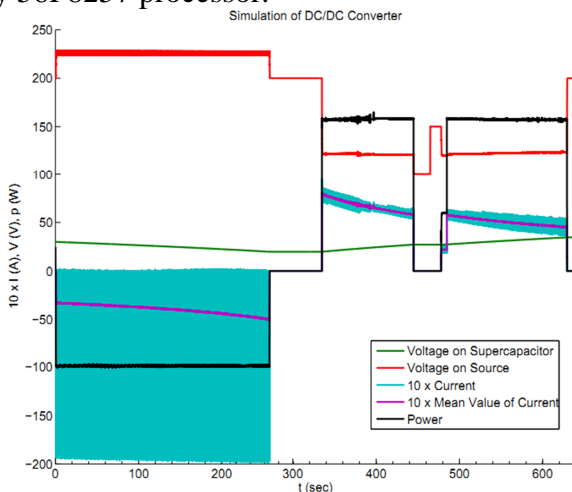


Fig. 5: Results of DC/DC converter simulation

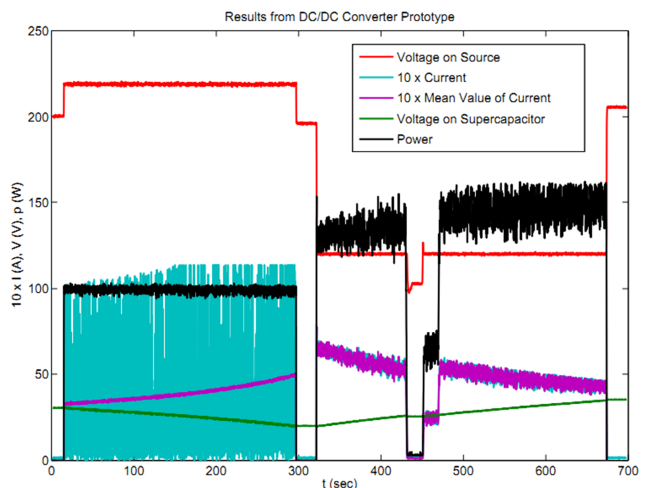


Fig. 6: Results of DC/DC converter prototype

Results of the simulation have been experimentally verified. The experiment was realized under following conditions: Super-capacitor initial voltage 35 V, voltage of DC BUS 200 V. In the time 1 s discharging of super-capacitor by the power 100 W is started. The super-capacitor reference voltage is 20 V. In the time 320 s the charging by power 150 W is started with voltage reference 25 V. In the time 450 s charging by power 150 W with voltage reference 38 V is started.

The result of simulation is shown in the fig. 5. From 1 s to 300 s super-capacitor is discharged by power 100 W. The source in model is simulated like ideal part with zero internal resistance. The discharging is stopped when the voltage on super-capacitor is 20 V. The next regime is buck mode with over-current protection. The controller limits the current if the voltage is lower than minimal value 120 V on the DC BUS. In time 420 s the source voltage was lower than minimal value, therefore charging was stopped and the next charging was started in time 465 s, when the voltage was greater than minimal value. The result for prototype is shown in the fig. 6. Measuring on the prototype has the same conditions as simulation. The inductor current is not for boost converter negative because the current probe is set to measure in one direction.

5. Conclusion

The result from simulation and result obtained from measurement are in very good accordance. Therefore it is possible to state the controller was designed correctly and the buck/boost converter with the super-capacitor can be implemented to the hybrid drive prototype model.

Acknowledgement

This research has been realized using the support of Technological Agency, Czech Republic, programme Centres of Competence, project # TE01020020 Josef Božek Competence Centre for Automotive Industry and was supported by the Grant Agency of the Czech Technical University in Prague, grant No. SGS13/073/OHK3/1T/13.

This support is gratefully acknowledged.

References

- [1] CE ROV S K Y, Z.; MI N D L , P. Hybrid electric cars, combustion engine driven cars and their impact on environment, SPEEDAM 2008, Italy: Sorrento, 2008. ISBN 978-1-4244-1663-9
- [2] CU N D E V, D.; MI N D L , P. European Driving Schedule of Hybrid Electric Vehicle with Electric Power Splitter and Supercapacitor as Electric Storage Unit Proceedings of the 2008 International Conference on Electrical Machines, Portugal: Vilamoura, 2008. ISBN 978-1-4244-1735-3
- [3] CU N D E V, D.; CE ROV S K Y, Z.; MI N D L , P. Modelling of the hybrid electric drive with an electric power splitter and simulation of the fuel efficiency, EPE '09, Spain: Barcelona, 2009. ISBN 978-1-4244-4432-8
- [4] D.M. Bellur and M.K.Kazimierczuk, DC-DC converters for electric vehicle applications. Nashville, TN, USA: Electrical Insulation Conference and Electrical Manufacturing Expo, 2007
- [5] CA M A R A , M.B.; GUA L O U S , H.; GU S T I N , F.; BE R T H O N , A.; DA K Y O , B. DC/DC Converter Design for Supercapacitor and Battery Power Management in Hybrid Vehicle Applications - Polynomial Control Strategy, IEEE Transactions on Industrial Electronics, vol.57, pp. 587-597, 2009.
- [6] CA M A R A , M.B.; GUA L O U S , H.; GU S T I N , F.; BE R T H O N , A. Control strategy of Hybrid sources for Transport applications using supercapacitors and batteries, Power Electronics and Motion Control Conference - IPEMC 2006, China: Harbin, 2006. ISBN 1-4244-0448-7
- [7] YI M I N G.; EH S A N I , M. Design and Control Methodology of Plug-in Hybrid Electric Vehicles, IEEE Transactions on Industrial Electronics, vol.57, pp. 633-640, 2010.



Laser system based measurement of road surface and surrounding area

*Marián Hruboš, *Aleš Janota

*University of Žilina, Faculty of Electrical Engineering, Department of Control and Information Systems, Univerzitná 2, 01026 Žilina, Slovak Republic, {marian.hrubos, ales.janota}@fel.uniza.sk

Abstract. The paper is aimed at presentation of the first results obtained in the process of designing, constructing and experimental testing of the laser measurement system based on the 2D laser scanner of the LD-OEM1000 type in road applications. The obtained clouds of measured points are further processed and visualized to get a starting point for future analysis of the scene, fusion of data obtained from multi-source measurement systems and design of future applications.

Keywords: Laser scanner, LD-OEM1000, measurement unit, C++ Builder 3D view.

1. Introduction

The ever-increasing intensity of road transport has adverse effects on the quality of communications. Different types of disturbances resulting from road surface damages such as cracks, potholes, longitudinal and transverse bumps, wavy surface, local declines or beaten longitudinal gauge have adverse effect on ride comfort and cause increased damage of certain parts of motor vehicles.

To measure the deformation of road surface many methods and measuring equipment have been developed so far. One large group of measuring devices used for measuring the deformation of road surface are laser measuring systems. These measurement systems use contactless measurement methods based on measurement of the laser pulse time of flight. With these methods we can measure a distance between the laser measuring device and the road surface.

Our system is based on usage of the 2D laser scanner LD-OEM1000 from the SICK Company.

2. Measurement process

A measurement unit is primarily designed to measure changes in geometrical parameters of the road and degradation of road surface over time. The secondary function of this unit is to measure surrounding area and environment around the measured road as a part of the actual measurement performed. The concept of the measurement unit is based on obtaining measured data and their rapid processing.

The core of the unit responsible for data acquisition is the laser scanner mentioned above. The control program ensures processing of individual measured data and getting individual values based on a selected algorithm. The output of the measuring unit is in the form of coordinates of individually detected points in space that are stored in the output file.

2.1. Laser scanner LD-OEM1000

The LD-OEM 1000 is an electro-optical laser measurement system that electro-sensitively scans the perimeter of its surroundings in a plane with the aid of laser beams. It measures its surroundings in two-dimensional polar co-ordinates. If a measuring beam is incident on an object, the position is determined in the form of distance and direction. The LDOEM emits pulsed laser

beams using a laser diode. If such a laser pulse is incident on an object, it is reflected at its surface. The reflection is detected in the laser measurement system's receiver using a photodiode. The distance to the object is calculated from the propagation time that the light requires from emission to reception of the reflection at the sensor. The laser beams emitted are deflected using a mirror in the scanner head and scan the surroundings in a circular manner. The measurements are triggered at regular angular steps using an angular encoder. The scanner is connected to the evaluation unit with an Ethernet interface. The laser scanner works as a TCP / IP server.



Fig. 1. Laser scanner LD-OEM1000

2.2. On-line data processing

Method for on-line processing of measured data is based on the use of communication functions in a computer program. Communication function implements these following operations:

- Follow-up communication with the laser scanner;
- Setting of the parameters for measuring laser scanner;
- Communication with the laser scanner;
- After receipt of the measured data initiation of the computational algorithm;
- Calculation of coordinates of the measured points stored in the output file.

The advantage of the indicated method is the ability to access the calculated coordinates of measurement points during the measurement.

2.3. Method of 3D measurement

The method of 3D measurement with incremental definition of a third axis is the manual method. The user defines the points at which measurements are made. Then it is possible to create a three-dimensional object composed of several measured sections.

Mathematical equations for this method are based on circle parametric equations. To calculate the x , y coordinates of the point of-interest we use circle parametric equations and calculate x , y coordinates based on the radius angle. The z -axis value is incremented in each measurement. The distance between measured sections is assumed to be the same.

Circle parametric equations are in the form (1):

$$\begin{aligned}
 x_n &= \cos(\alpha) * r \\
 y_n &= -\sin(\alpha) * r \\
 z_n &= n .
 \end{aligned}
 \tag{1}$$

The laser scanner provides these data about measurement points: initial angle, number of measured points, angular difference between two adjacent points and distances between the laser scanner and measured points. It is necessary to adjust the parametric equations of the circle to calculate the i -th measured point in the n -th measurement profile. The computation is performed for every measured point. The sequence number of the measured point is incremented with every calculation cycle in every measurement profile. The value of z -coordinates is incremented in each

measurement. The modified parametric equations for calculation of the i -th measured point in the n -th profile are given below (2):

$$\begin{aligned} x_{in} &= \cos[(\alpha_{0n} + i * \Delta\alpha_n + 90) * \pi * 2 / 360] * d_{in} \\ y_{in} &= -\sin[(\alpha_{0n} + i * \Delta\alpha_n + 90) * \pi * 2 / 360] * d_{in} \\ z_{in} &= n . \end{aligned} \quad (2)$$

where x_{in} , y_{in} and z_{in} are coordinates of the i -th measurement;

α_{0n} is a value of the initial angle;

i is a serial (sequential) number of the current point;

$\Delta\alpha_n$ is a value of the angular increment for the given measurement profile;

d_{in} is a distance between the i -th point and the laser scanner head;

n is a serial (sequential) number of measurements and this value is incremented cyclically.

The speed of calculation of measured point coordinates is the main advantage of the 3D measurement with the incremental definition of the third axis. Designed and created evaluation software is based on the on-line processing of data obtained from the measurement unit (see the screen view in Fig. 2, based on the previously performed work [1]). It has been programmed in C++ Builder6. Processing is carried out based on the analytical analysis of the packet content. The first practical results have already been obtained: Fig. 3 shows a visualized cloud of points of the road scanned inside the university campus containing the surrounding area (buildings), Fig. 4 shows the scanned road together with some trees and vegetation around it. These images can further be analyzed with the help of own classification algorithms to distinguish between individual objects such as the road surface, road furniture, trees, etc.

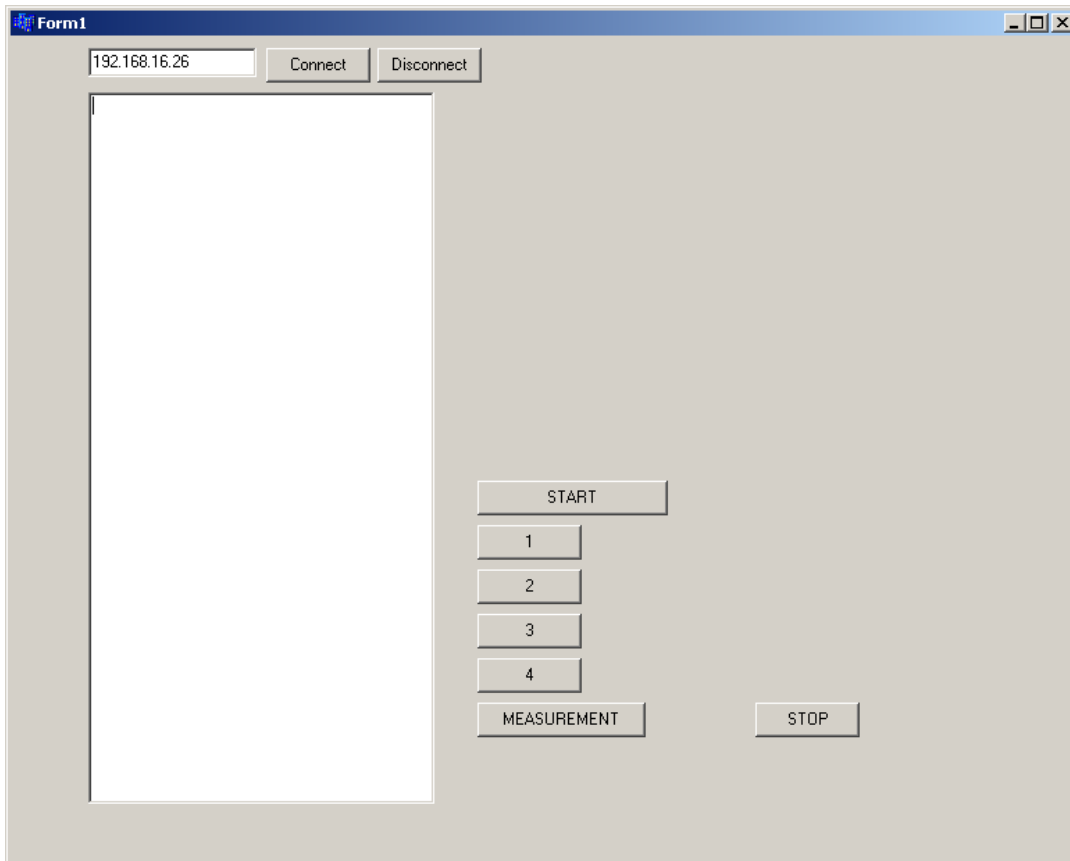


Fig. 2. Example of the evaluation software screen

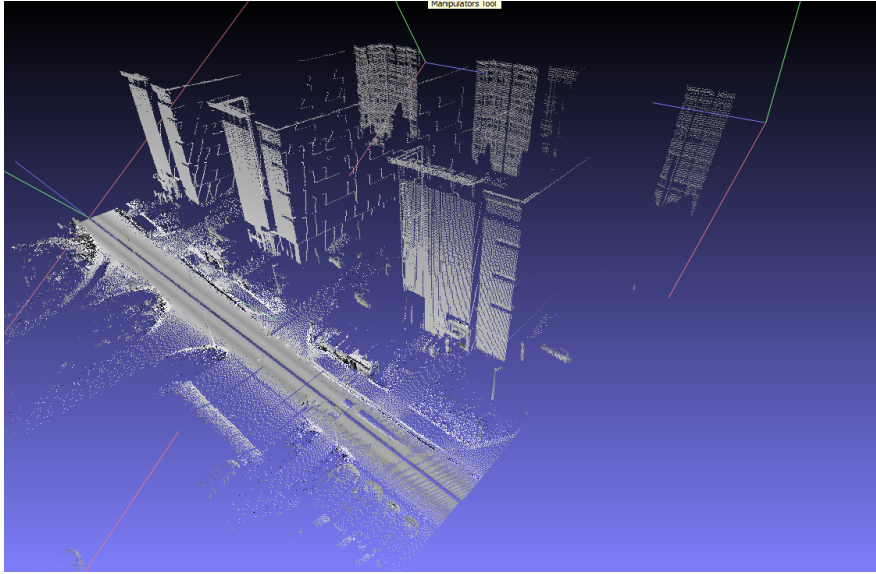


Fig. 3. A cloud of measured points representing the building

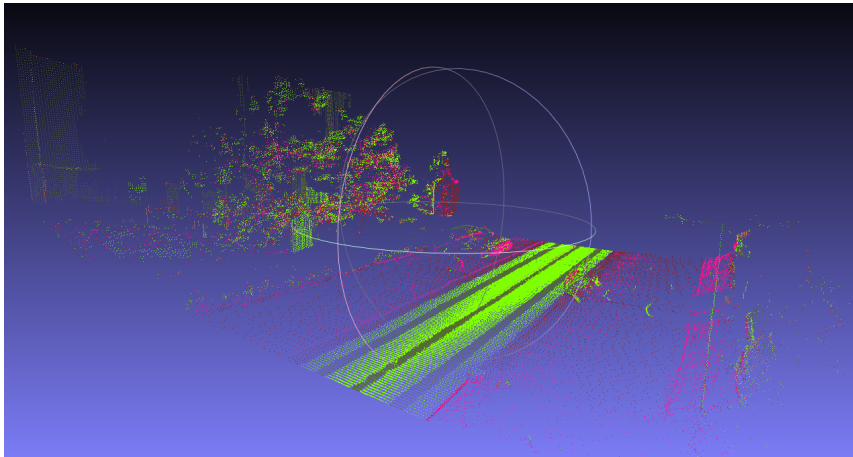


Fig. 4. A cloud of measured points representing the tree

3. Conclusion

The primary use of the unit is a measurement of the road surface characteristics; however its functionality has been extended to cover the ambient space, too. The presented results represent the first practical findings in the PhD thesis solved by the 1st and supervised by the 2nd author. Future work will be concentrated on fusion of measured data with data from other measurement systems.

Acknowledgement

The paper was elaborated with support of the Slovak grant agency VEGA, grant No. 1/0453/12 "Study of interactions of a motor vehicle, traffic flow and road".

References

- [1] HRUBOŠ, M. Nástroj na zistenie stavu degradácie vozovky v čase. MSc. thesis, University of Žilina, 2012
- [2] User manual - BALDOEM1000en_8011504_20090115.pdf
<https://www.mysick.com/eCat.aspx?go=FinderSearch&Cat=Row&At=Fa&Cult=English&FamilyID=344&Category=Produktfinder&Selections=34390,34243>, available online 1.5.2013

Basics for compensation of FDS measurements for transformer insulation diagnostics

*Jozef Jurčák, *Miroslav Gutten, *Daniel Korenčiak

*University of Žilina, Faculty of Electrical Engineering, Department of Measurement and Applied Electrical Engineering, Univerzitna 1, 01026 Žilina, Slovak Republic, {jozef.jurcik, miroslav.gutten, daniel.korenciak}@fel.uniza.sk

Abstract. In this paper we describe how to calculate activation energy for hopping mechanism for oil impregnated pressboard in transformer insulation. This energy is added to insulation from temperature from environment in transformer operation. Linearization of the activation energy is the first step to calculate thermal compensation in FDS measurement in operation.

Keywords: Pressboard, insulation, transformer, FDS, oil, measurement.

1. Introduction

Measurement of insulation state of transformer winding is helpful for maintain and its reliable operation. There are many of operational statuses and working condition for transformer. Transformer insulation is in different environment when we want to measure its condition. All these surroundings have influence to immediate state of transformer insulation.

If we measure some values in frequency methods (in our case FDS¹ is used) for the same transformer in different times the environment case differences between measured values. But these values are not pointing to change in operation state but only in change in environment (temperature, weather etc.).

We present proposition for calculation of unification basic for measured values. We bring measured values and calculate activation energy for Hopping phenomena. This is basic step for temperature compensation of FDS measurement.

2. Entry conditions for measurements

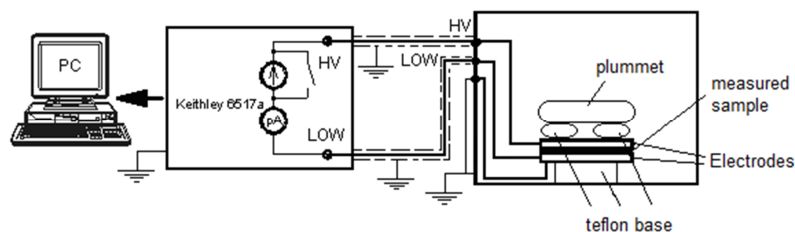


Fig. 1. Schematic of measurement apparatus.

Values, which were used in this article, are from oil impregnated pressboard T-IV which is manufactured by Weidmann. Weidmann is the global leader in electrical insulation for transformer manufacturers and transformer users. Sample had these dimensions: $1 \times 215 \times 215 \text{ mm}^3$. Next step was drying the samples in vacuum chamber at $353,15^\circ\text{K}$ temperature. When the weight was stop falling the moisture was determined and its value was $X = 0,55 \div 0,6\%$ of weight. Next step

¹ Frequency Domain Spectroscopy

was feeding sample with moisture contained in air. This process was in progress at temperature of room (it means 293,15°K) at $\zeta = 65 \div 75\%$ of relative humidity. Then the sample was impregnated with insulation oil in vacuum chamber for 72 hours at $T = 348,15^\circ\text{K}$ temperature and $\zeta = 15\%$ of relative humidity. Measured values are showed in “Fig. 2”.

So the surrounding conditions are represented by these curves. Each of these curves is measured for the same sample at different temperatures. This figure shows bad condition for comparison of one insulation system in different conditions caused only by environment.

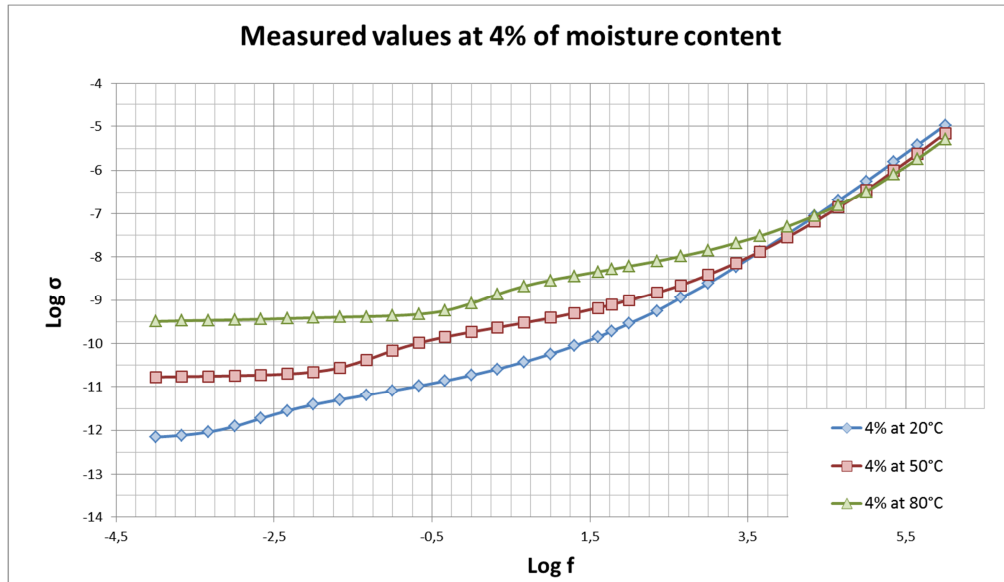


Fig. 2. Measured values of conductivity at 4% of moisture content in oil impregnated paper pressboard.

3. Analysis of the AC - conductivity

In analysis of the “Fig. 2” shows non-frequency dependence in ultra-low frequency for conductivity (e.g. slope 4% at 80°C). This area is like in time domain. But in frequency about $f = 10^{-1}\text{Hz}$ (for 4% at 80°C slope) the conductivity starting rise. In measurement the conductivity is rising with rising of frequency in [1]. In this case is characteristic hopping phenomena and this phenomena could be written by expression “(1)”:

$$\sigma \propto f^\alpha. \quad (1)$$

In [1] α is depending on form of pass-over of charge. In tunnel pass-over charge is $\alpha_T \leq 0,8$. But in hopping phenomena the size of potential barrier is $\alpha_B > 0,8$. The expectation for calculating with this value is regarded to constant value. This value is similar for jumping charge exchange in alternating and static magnetic field which was showed in later models in [2] and coefficient in “(1)” is frequency function. Its value $\alpha(f)$ could be determined by computer simulation [3]. These results show non-dependence of frequency in low frequency and $\alpha(f) \cong 0$. But in frequency range is observed rising of $\alpha(f)$ to its maximum value. In [2] - [4] the value of $\alpha_{max}(f)$ is function of probability p in charge skipping from second to third well in electric field direction is showed. In big values of probability $p \cong 0,5$, when is the probability of skipping of charge from second to third well and probability of skipping the charge from second to first well is approaching to $\alpha_{max}(f) \cong 0$ and conductivity is not depend on frequency. But in other side for $0 < p < 0,5$ are values $0 \leq \alpha_{max}(f) \leq 2$. In [2] - [4] are introduced models related observed conduction limits, which are swaying to constant value in time domain.

We could present $\alpha(f)$ from our measurement. So the curves had following shapes:

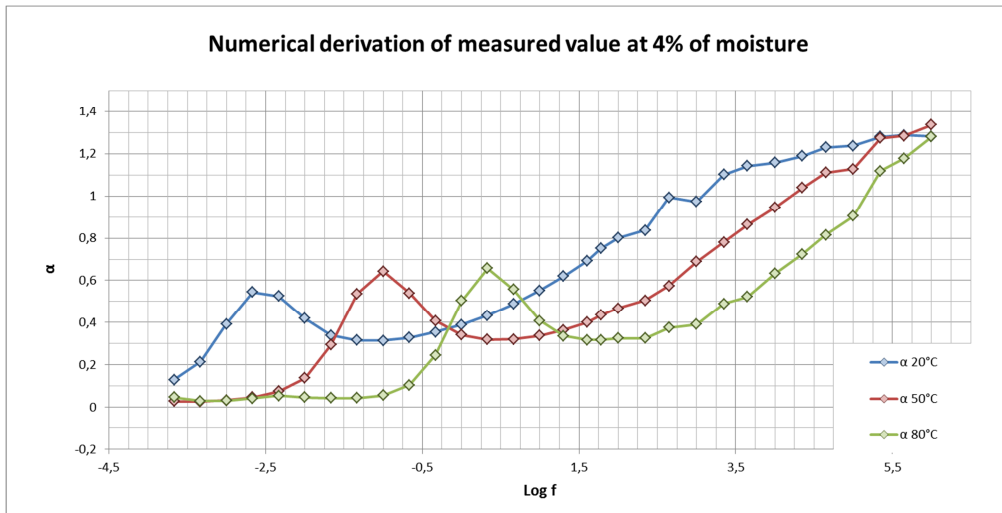


Fig. 3. Values of numerical derivation at 4% of moisture content in oil impregnated paper pressboard.

On “Fig. 3“ we could observe three typical points. But we must adjust curves for better results because the measured values are presented only small assemblage of points. So the derivation is very roughing for this reason. Now we approximate the measured behavior in Matlab and then make a numerical derivation. The shape of curves is more confidential and similar to reality. Approximated and then derivated curves are on “Fig. 4“.

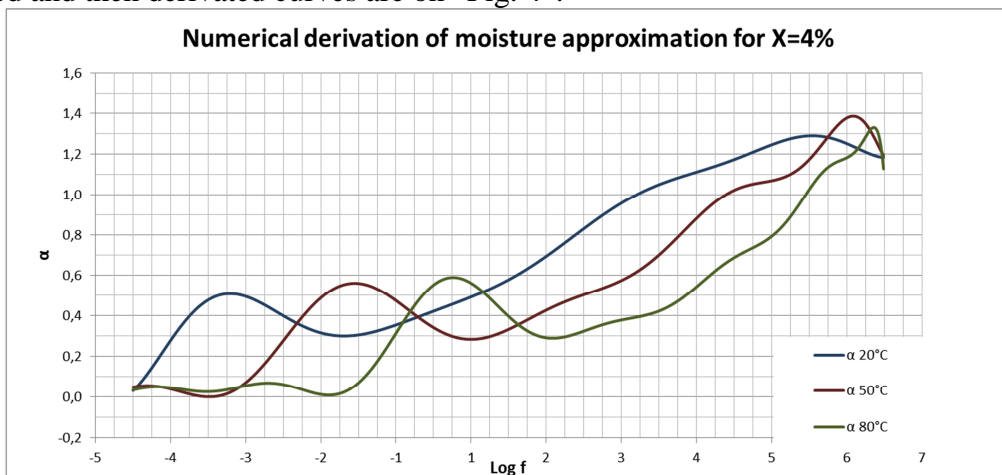


Fig. 4. Approximation of numerical derivation at 4% of moisture content in oil impregnated paper pressboard.

We had typically points for next calculating in this step. This points seems to be the best way to curve fitting for calculation of activation energy. In next step we must show some equations for calculating $\Delta E(\sigma)$.

4. Determination of the activation energy

On the direct-current conductivity basis is showed tunnel phenomena between two closer neighbours [5] in wet oil impregnated pressboard. Major influence on conductivity had value of activation energy of conductivity in this case. We can obtain it as follows:

$$\sigma(T) = \sigma_0 \exp - \frac{\Delta E(\sigma)}{kT} \quad (2)$$

From equation (2) rewritten for two elements of temperature we obtain:

$$\Delta E(\sigma) = \frac{k}{\left(\frac{1}{T_1} - \frac{1}{T_2}\right)} \cdot (\ln \sigma (T_1) - \ln \sigma (T_2)) \quad (3)$$

From last equation (3) we could obtain graphic dependence for $\Delta E(\sigma)$.

4.1. Compensation

We had activation energy, derivation and measured values now. So we must slide between measured curves to linearize the activation energy dependence on frequency. For this operation are needed typical points obtained from derivation. These local extremes are terminative for sliding the curves for best fit. Then we obtain next behaviours:

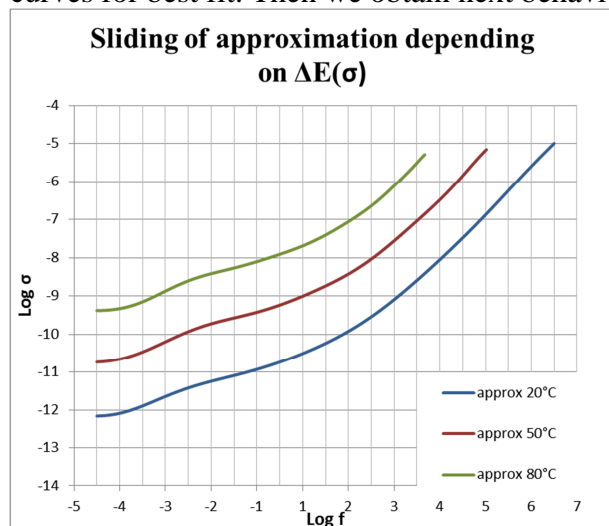


Fig. 5. Slided curves depended on $\Delta E(\sigma)$.

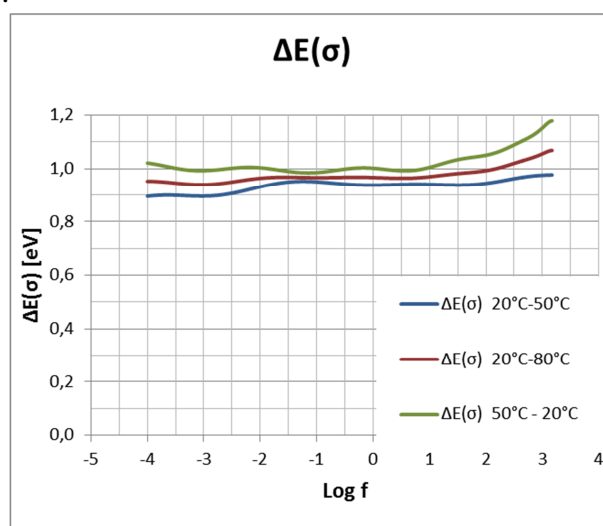


Fig. 6. $\Delta E(\sigma)$ after sliding.

5. Conclusion

This method is summary of optimization for FDS measurement and its compensation for operation. We could be able to compare state of insulation in operation at any environmental condition when we obtain an measured values and then apply this method. This is basic step for unification of FDS measurement and its consequential use in practice.

Acknowledgement

This work was supported by the Grant Agency VEGA from the Ministry of Education of Slovak Republic under contract **1/0624/13**.

References

- [1] N. F. Mott a E. A. Davis, „Electron Processes in Non – Crystalline Materials,“ rev. Clarendon Press, Oxford, 1979.
- [2] P. Zhukowski, T. Kołtunowicz, J. Partyka, P. Węgierek, F. F. Komarov, A. M. Mironov, N. Butkievith a D. Freik, „Dielectric Properties and Model of Hopping Conductivity of GaAs Irradiated by H⁺ Ions,“ *Vacuum*, zv. 81, %1. vyd.1, pp. 1137-1140, 2007.
- [3] P. Żukowski, T. Kołtunowicz, J. A. Fedotova a A. V. Larkin, „An effect of annealing on electric properties of nanocomposites (CoFeZr)_x(Al₂O₃)_{1-x} produced by magnetron sputtering in the atmosphere of argon and oxygen beyond the percolation threshold,“ *Przegląd Elektrotechniczny*, zv. 86, %1. vyd.7, pp. 157-159, 2010.
- [4] P. Żukowski, T. Kołtunowicz, J. Partyka, P. Węgierek, M. Kolasik, A. V. Larkin, J. A. Fedotova, A. K. Fedotov, F. F. Komarov a L. A. Vlasukova, „Model przewodności skokowej i jego weryfikacja dla nanostruktur wytwarzanych technikami jonowymi,“ *Przegląd Elektrotechniczny*, zv. 1, %1. vyd.3, pp. 247-249, 2008.
- [5] P. Zhukowski, M. Szrot a J. Subocz, „Przegląd Elektrotechniczny,“ *Przegląd Elektrotechniczny*, zv. 88, %1. vyd.11, pp. 361-363, 2012.



Electromagnetic interference of LLC resonant converter in different modes of operation

*Tomáš Kapusta, *Juraj Koscelník

*University of Žilina, Faculty of Electrical Engineering, Department of Mechatronics and Electronics,
Univerzitna 1, 01026 Žilina, Slovak Republic, {tomas.kapusta, juraj.koscelnik}@fel.uniza.sk

Abstract. This paper deals about electromagnetic compatibility and electromagnetic interference of resonant converter, type LLC, switching with frequency 300 kHz. Authors focus at different operation mode of resonant converter which usually works with frequency near or little bit bellow of resonant frequency. The main advantages of resonant converters are included in paper. The one is good control characteristic and this is reason of different mode operations.

Keywords: Electromagnetic compatibility, high frequency converter, LLC resonant converter

1. Introduction

Electromagnetic compatibility is relative new area of electrical engineering which has an important role in power electronics systems, industry but also in medicine e.g. EMC belong in everyday life. In every household also we can find many of electrical equipment which contains many switching mode power supplies working with high switching frequency with middle levels of output power. Every device working with high frequency especially devices in which large derivation of currents (di/dt) or voltage (du/dt) we can find. Any such device can be significant source of interference. The main idea is not only electromagnetic interference and its reducing to minimal level but the second important role is to ensure electromagnetic susceptibility of devices. One of these devices is resonant converter.

2. Resonant converters

Ones of the needs modern switching mode power supplies is high efficiency, high power density. This is reason of ever-increasing levels of switching frequencies of these devices. Increasing switching frequency is causing increasing of loss in switching components in main circuit of converter. Depending on the output power interferences increases. The next generation of converters reducing switching loss and interferences is resonant converter. Concept of the resonant converters is nowadays great expanded and used in various applications, such as power supplies for laptops, LCD televisions and the supplies for telecommunication devices.

Resonant components applied in main circuit of converter affect time course of currents and voltages. During commutation of semiconductor switches create largest loss and converter produce electromagnetic interferences. All of resonant converters work with the same principles. Rectangular course of voltage in resonant circuit cause high frequency circulating of energy which is transformed through HF transformer to output. Resonant circuit can be designed for operation in soft switching mode and this is one of main advantages of these topologies. There are several basic topologies of converters with:

- serial resonant circuit,
- parallel resonant circuit,
- serial-parallel resonant circuit,
- multi resonant circuit.

3. LLC resonant converter

The fundament of the LLC resonant converter is series-parallel LLC resonant circuit, placed on the primary side of the converter and ensures ZVS technique for main switches. Great property of this dc/dc converter in comparison with conventional series resonant converters is, that LLC converter can operate in the soft switching mode with switching frequency under and among the resonant frequency. The ZVS switching technique used on the main switching elements is reached using accumulated energy in magnetizing inductance of the transformer. This energy makes possibility of operation of the converter to apply soft switching on the wide range of load.

The LLC resonant converter has two resonant frequencies. The operating point is moving between these two points depending on the converters' input voltage and the load. The principal scheme of the above mentioned converter is shown on the Fig. 1.

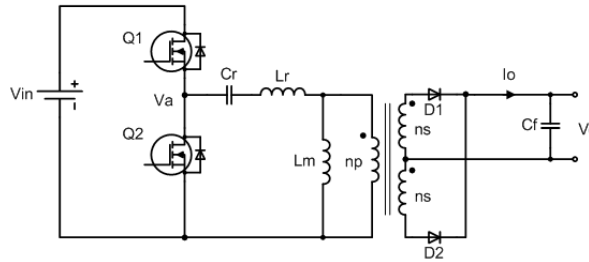


Fig. 1. Half bridge LLC resonant converter.

Two resonant frequency of LLC are given by components in main circuit. The first resonant frequency is determined by resonant inductor L_r , leakage inductance L_σ of HF transformer and resonant capacitor C_r (1).

$$f_1 = \frac{1}{2\pi\sqrt{(L_r + L_\sigma)C_r}} \quad (1)$$

Second resonant frequency is determined resonant inductor L_r , leakage inductance L_σ and magnetizing inductance of HF transformer and resonant capacitor C_r (2).

$$f_2 = \frac{1}{2\pi\sqrt{(L_r + L_\sigma + L_m)C_r}} \quad (2)$$

Figure 2. is DC characteristic of LLC resonant circuit. The axis-x is ratio of resonant frequency and switching frequency and the axis-y is gain of resonant circuit. Point f_s/f_r where value is equal 1 is resonant frequency f_1 . Frequency f_2 is under this point.

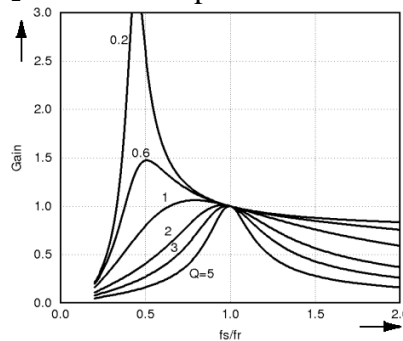


Fig. 2. DC characteristic of LLC resonant circuit

Mathematical expression of DC characteristic is equation (3) and (4) where gain is M , n is transformer ratio, $V_{o,i}$ output and input voltage, m is ratio of resonant and magnetizing inductance and Q is quality of resonant circuit [2].

$$M = \frac{2nVo}{Vi} = \left| \frac{\left(\frac{\omega^2}{\omega_0^2}\right)\sqrt{m(m-1)}}{\left(\frac{\omega^2}{\omega_0^2}-1\right) + j\left(\frac{\omega}{\omega_0}\right)\left(\frac{\omega^2}{\omega_0^2}\right)(m-1)Q} \right| \quad (3)$$

$$M = \frac{V_o}{V_i} = \frac{1}{2n\sqrt{\left[1 + \frac{1}{m}\left(1 - \frac{f_i^2}{f^2}\right)\right]^2 + \left[\left(\frac{f_1-f}{f}\right)\frac{Q}{f_1}\right]^2}} \quad (4)$$

4. Analysis and measurement of 300 kHz LLC resonant converter

We recognized LLC resonant converter with 300 kHz resonant circuit at different values of switching frequency it useful to research impact to electromagnetic interference. In normal operation mode is converter switching with frequency near main resonant frequency (in resonance is impedance of resonant tank near zero and in this condition is gain independent of the load. But during control of LLC converter might happen condition when switching frequency is under (above) resonant.

From point of view electromagnetic compatibility especially interference and impact to other devices is important shape of input current and related current in resonant circuit. Parameters of the recognized converter are:

- $V_{in}=280-380$ V, $V_{out}=48$ V, $I_{out}=4$ A, $f_{sw}=300$ kHz

4.1. Operation mode of 300kHz LLC resonant converter and electromagnetic interference in different modes of operation

Operation modes (Fig. 3) of LLC converter can be divided depending resonant frequency:

- switching frequency equals resonant frequency – $f_{sw} = f_r$,
- switching frequency is under resonant frequency – $f_{sw} < f_r$,
- switching frequency is above resonant frequency – $f_{sw} > f_r$.

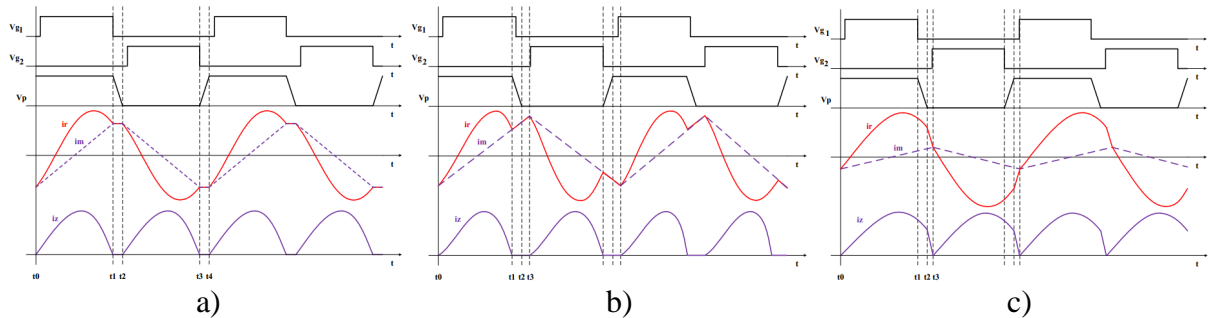


Fig. 3. Theoretical currents i_p (primary), i_m (magnetizing) and voltages $V_{g1,2}$ courses in operation mode a) $f_{sw}=f_r$, b) $f_{sw}<f_r$, c) $f_{sw}>f_r$

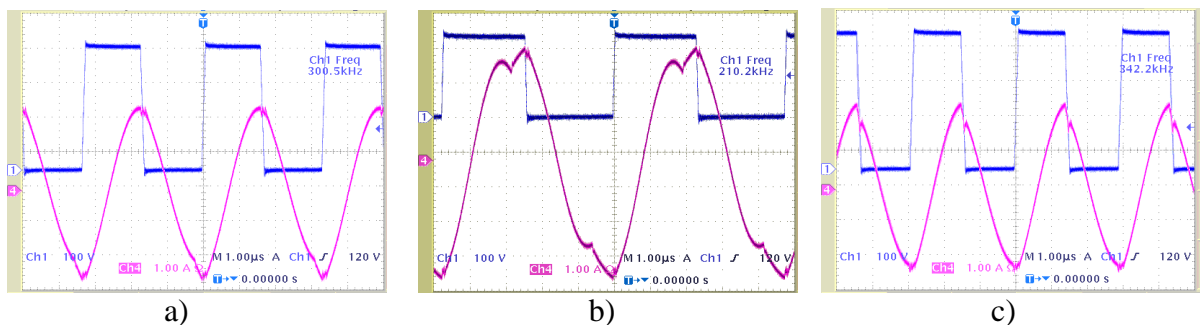


Fig. 4. Measured current i_p (primary) and voltage v_p (primary) courses in operation mode a) $f_{sw}=f_r$, b) $f_{sw}<f_r$, c) $f_{sw}>f_r$

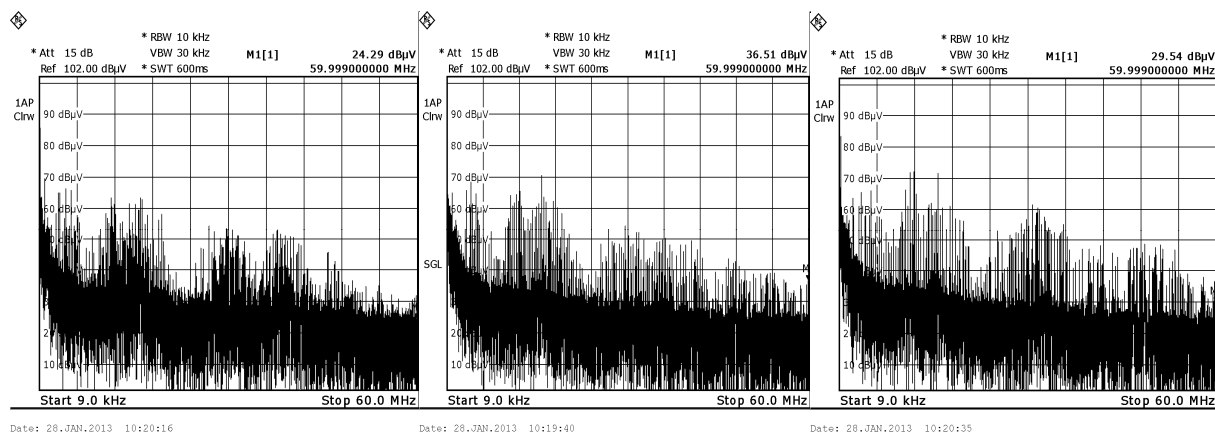


Fig. 5. Measured electromagnetic interference using LISN in operation mode a) $f_{sw}=f_r$, b) $f_{sw}<f_r$, c) $f_{sw}>f_r$

Fig. 4 is derived to three parts. Part *a* is measurement of primary current and primary voltage in operation mode when switching frequency equals main resonant frequency (300 kHz). The shape of primary current is sinusoidal with little ringing during switch-on and switch-off MOSFET transistors. Part *b* is figure of primary current and voltage with switching frequency 210 kHz so about 90 kHz under resonance. Under resonance mode we can find distortion of primary current. When magnetizing and resonant current achieve equality, magnetizing inductance begin supports current in circuit and so high frequency transformer is reason of this distortion. Part *c* is with switching frequency 340 kHz, about 40 kHz above resonant frequency. This is the worst case because in addition to shape of input current output rectifier diode switch-off with high di/dt .

5. Conclusion

Figure 5 is measurement of electromagnetic interferences (EMI) in three modes of operation. The peak voltage measured at line impedance stabilizing network (LISN) connected between supply and LLC resonant converter is displayed on spectrum analyzer in $dB\mu V$. We can see impact of different mode of operation to spectrum in frequency range 9 kHz-60 MHz. International standards prescribes conducted interferences measured in frequency range between 9 kHz (150 kHz) and 30 MHz. The best case from electromagnetic conducted interference point of view is mode when switching frequency is equals resonant frequency or slightly less, near resonance. Influence of control technique can be positive in this case when used frequency modulation, known as jittering. The way how we can improve EMI is also using passive filtering. EMI filter can be placement behind power line at the input of SMPS. Using passive components as inductor, capacitor and resistor we can insert required value of filter loss in required frequency range.

Acknowledgement

The author wish to thank to project VEGA no.1/0943/11 and project OPVaV-2008/2.1/01 SORO 262220120003

References

- [1] CHLEBIŠ, P.: Soft Switching Converters, Monograph, VŠB-TU Ostrava, Ostrava, Czech republic, 2004
 - [2] SPANIK, P., KANDRAC, J., FRIVALDSKY, M., DRGONA, P., Verification of operation modes of design LLC resonant converter, Communications, Scientific letters of University of Zilina, 2°, 2011
 - [3] KOVACOVA, I., KANUCH, KOVAC, D., EMC z hlediska teorie a aplikace, ISBN 80-7300-202-7, BEN technická literatura, 2006
 - [4] CACCIATO, M., CONSOLI, A., et. al., Reduction of common mode currents in PWM inverter motor drives, IEEE IAS'97, vol.1, pp. 707-714, 5-9 Oct. 1997.
- KOSTOV, K.: Design and Characterization of Single-Phase Power Filters, dissertation, ISBN (pdf) 978-952-248-187-0, Helsinki University of Technology, Department of Electrical Engineering



Moment of inertia influence on pulsation of rotational speed waveform in PMSM and SRM

Krzysztof Ludwinek¹, Jan Staszak¹, Rafał Jurecki², Wojciech Sadkowski², Mateusz Marciniewski²,
Darek Więckowski³, Grzegorz Klimont¹

Kielce University of Technology, Al. Tysiąclecia P. P. 7, 25–314 Kielce, Poland,

¹ Department of Electrical Machines and Mechatronic Systems, tel.: +48 41 3424225, fax: +48 41 3424207
e-mail: melkl@tu.kielce.pl, meljs@tu.kielce.pl, g.kimont@tu.kielce.pl,

² Department of Automotive Vehicles and Transport, tel.: +48 41 3424285, fax: +48 41 3424726,
e-mail: rjurecki@tu.kielce.pl, w.sadkowski@tu.kielce.pl, m.marciniewski@tu.kielce.pl

³ Automotive Industry Institute, ul. Jagiellońska 55, 03-301 Warszawa; d.wieckowski@pimot.org.pl

Abstract. The paper presents results of works concerning evaluation of moment of inertia influence on PMSM and SRM electromagnetic torque waveforms in the motors frequently used in power electronic and mechatronic systems. Simulation models of PMSM and SRM and comparison of simulation dynamic states at starting condition on electromagnetic torque waveforms have been carried out.

Keywords: PMSM, SRM, pulsation, rotational speed, moment of inertia.

1. Introduction

Utilization of permanent magnets (PM) in Brushless Direct Current Motors (BLDCM), Brushless Alternating Current Motors (BLACM) or frequently the machines are named Permanent Magnet Synchronous Motor (PMSM) and Switch Reluctance Motors (SRM) in mechatronic systems at present is developed very dynamically [3, 4]. Through the electrical and mechanical good properties, these motors are found wide application in different type of light vehicles with electric drive (cycles and motorcycles, wheel-chairs, light delivery vans, etc) automatics, power electronic systems or generally in mechatronic systems. In these systems the best achievements are getting with adaptation of modern construction technology of electric motors with permanent magnets, power electronic converter with suitable control system and with the suitable selection of power supply sources (e. g. battery). However, about the choice of the driving system decide not only the advantages of the electrical motors, but also properties of the all driving mechatronic system with electronic converter, power supply source and of course a moment of load inertia. Driving system should be designed with components which assure possibly the efficiency of the driving mechatronic system as high as possible. For the purpose of optimum–projecting of the driving system, is necessary acquaintance of the angular frequency (hunting) of electrical rotors which appear in SRM and PMSM. The paper presents results of works concerning evaluation of moment of inertia influence on waveforms of PMSM and SRM rotational speed.

2. PMSM model for simulation tests

PMSM control model is built based on the voltage equations in axis d and q [1, 2]:

$$u_{sd} = R_s i_s + \frac{d\Psi_{sd}}{dt} - \omega \Psi_{sq} \quad (1)$$

$$u_{sq} = R_s i_s + \frac{d\Psi_{sq}}{dt} + \omega \Psi_{sd} \quad (2)$$

The flux Ψ_{sd} and Ψ_{sq} are defined as:

$$\Psi_{sd} = L_s i_{sd} + \Psi_m \quad (3)$$

$$\Psi_{sq} = L_s i_{sq} \quad (4)$$

where: u_{sd} , u_{sq} – respectively, stator voltage in the d and q axes; i_{sd} , i_{sq} – respectively, stator current in the d and q axes, Ψ_m – the magnetic flux of permanent magnet; R_s – stator winding resistance, L_s – stator winding inductance.

A system of equations (1) and (2) is completed by motion equation:

$$\frac{J}{p} \frac{d\omega}{dt} = T_e - T_m - \frac{D}{p} \omega \quad (5)$$

where: T_m – mechanical load torque, D – viscous friction coefficient, T_e – PMSM electromagnetic torque while

$$T_e = \frac{3}{2} p (\Psi_{sd} i_{sq} - \Psi_{sq} i_{sd}) \quad (6)$$

To build the PMSM model, the block of PMSM is used. The block is located in SimPowerSystemstolbox in Matlab/Simulink packet.

3. SRM model for simulation tests

SRM control model is built based on the voltage equation [1, 2]:

$$U_{ph} = R_s i_s + \frac{d\Psi_s(i_s, \vartheta)}{dt} \quad (7)$$

where: R – resistance per phase; i_s – phase current; L_s – inductance per phase; ϑ – rotor position, Ψ_s – flux linkage per phase, where:

$$\Psi_s = L_s(i_s, \vartheta) i_s \quad (8)$$

taking into consideration the relationship (8), equation (7) can be written as:

$$U_{ph} = R_s i_s + L(i_s, \vartheta) \frac{di_s}{dt} + e \quad (9)$$

where: e is induced emf, where

$$e = \frac{dL(i_s, \vartheta)}{d\vartheta} \Omega i_s = K_b \Omega i_s \quad (10)$$

where: $\Omega = \frac{d\vartheta}{dt}$ – angular speed, $K_b = \frac{dL(i_s, \vartheta)}{d\vartheta}$ – constant coefficient.

Equation (9) should be supplemented by the equation of motion (5), where the electromagnetic torque of a SRM is defined as [5, 6]:

$$T_e = \frac{1}{2} i_s^2 \frac{dL_s(\Theta, i_s)}{dt} \quad (11)$$

4. Calculation of rotational speed waveforms

Block diagrams of the Permanent Magnet Synchronous Motor and Switch Reluctance Motor drive system used in simulations is shown in Fig. 1 and Fig. 2. The presented block diagrams of PMSM and SRM are built in Matlab/Simulink system. In Fig. 1 the fundamental element of mechatronic system is PMSM with three-phase star-connected windings rated data as follows: nominal power $P_N = 100$ W, nominal voltage $U_N = 240$ V, rated speed $n_N = 3000$ rpm.

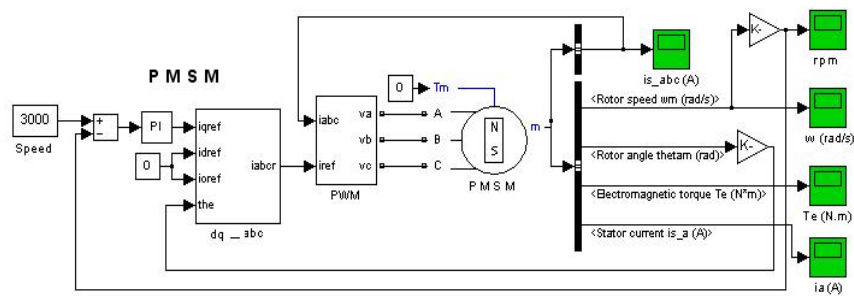


Fig. 1. Block diagram of a PMSM drive system

In Fig. 1 the PMSM model for simulation studies is equipped with the following elements:

- *Proportional-Integral* controller – responsible for decreasing the difference between the reference speed and the actual speed,
- *dq_abc* block – implementing inverse Park's transformation,
- *PWM* block through which stator windings are powered,
- *PMSM* block,
- the output – enabling observation of the selected output signals.

In Fig. 2 the fundamental element of mechatronic system is SRM with three-phase star-connected windings rated data as follows: nominal power $P_N = 100$ W, nominal voltage $U_N = 240$ V, rated speed $n_N = 3000$ rpm.

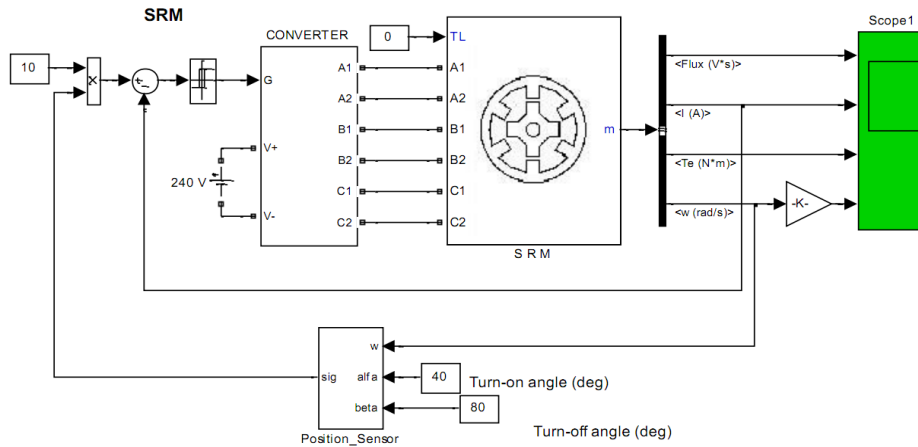


Fig. 2. Block diagram of the PMSM and SRM drive system

The simulation result of moment of inertia influence on PMSM and SRM rotational speed waveforms in case of $J=7.5758 \times 10^{-6} \text{ kgm}^2$, $64.13 \times 10^{-6} \text{ kgm}^2$ and $256.52 \times 10^{-6} \text{ kgm}^2$ are shown respectively, in Fig. 3 and Fig. 4.

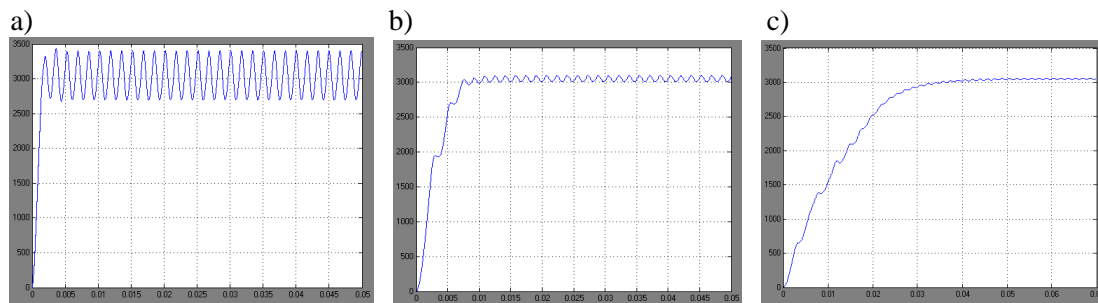


Fig. 3. Moment of inertia influence on PMSM rotational speed waveforms a) $J=7.5758 \times 10^{-6} \text{ kgm}^2$, b) $J=, 64.13 \times 10^{-6} \text{ kgm}^2$, c) $J= 256.52 \times 10^{-6} \text{ kgm}^2$

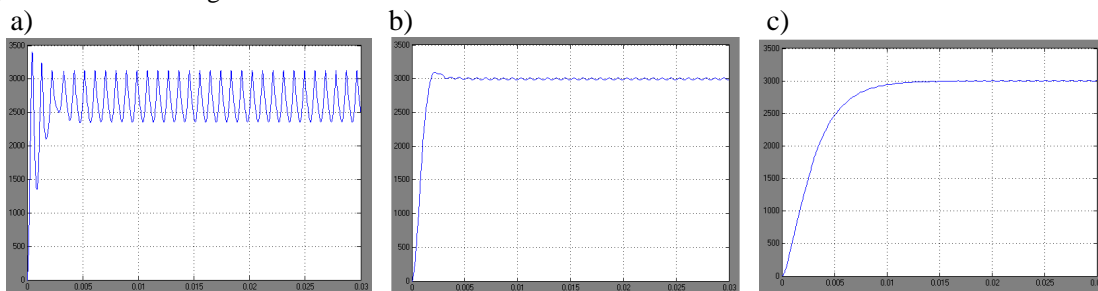


Fig. 4. Moment of inertia influence on SRM rotational speed waveforms a) $J=7.5758 \times 10^{-6} \text{ kgm}^2$, b) $J=, 64.13 \times 10^{-6} \text{ kgm}^2$, c) $J= 256.52 \times 10^{-6} \text{ kgm}^2$

In Table 1 are presented value of coefficients which were used to evaluate the influence of the moment of inertia on the rotational speed waveforms of PMSM and SRM. Where: J – moment of inertia (moment of inertia), δ – over-regulation overshoot, t_r – time of regulation, t_{nr} – rise time of rotational speed (rise time speed), A_1 – magnitude of rotational pulsation angular speed in steady state (pulse amplitude of speed in steady state).

J [kgm ² ·10 ⁻⁶]	δ [%]		t_r [s]		t_{nr} [s]		A_1 [rpm]	
	PMSM	SRM	PMSM	SRM	PMSM	SRM	PMSM	SRM
7.58	46	14.3	7.9	8.6	0.38	1.52	382.5	352.5
26.61	13.7	7.3	8.8	10.2	0.84	2.75	37.7	109.1
45.37	5.3	0.2	9.4	14.1	1.32	4.65	21.5	63.5
64.13	3.1	~0	10.2	17.2	1.81	7.35	15.3	45.3
128.26	0.7	~0	11.5	29.8	4.84	17.32	7.4	22.2
256.52	~0	~0	21.1	58.3	15.9	34.05	3.7	11.8

Tab. 1. Value of coefficients which were used to evaluate the influence of the moment of inertia on motor rotary speed route a) PMSM b) SRM.

5. Conclusion

The paper presents results of works concerning evaluation of moment of inertia influence on rotational speed waveforms for PMSM and SRM with three-phase winding. Simulation models of PMSM and SRM and comparison of simulation dynamic states at starting condition on rotational speed waveforms have been carried out. Both PMSM and SRM motors generate torque pulsation, which results from the stepped change in the angle between the axis of the resultant flow of armature winding and the axis of excitation flux. In case of SRM torque pulsation is greater because of greater mechanical stator and rotor asymmetry. The problem of torque ripples is still investigated by the research team and the results will be presented in papers, which will follow later on.

References

- [1] Kirshnan R., *Switched reluctance motor drives*. CRC Press LLC, 2001.
- [2] Miller T.J.E., *Switched Reluctance Motors and Their Control*. Magna Physics Publishing and Clarendon Press, Oxford 1993.
- [3] Roman Nadolski, Krzysztof Ludwinek, Jan Staszak, Marek Jaškiewicz: Utilization of BLDC motor in electrical vehicles, *Electrical Review*, R. 88 NR 4a/2012 p. 180 - 186.
- [4] SimPowerSystem. Matlab 2010a, version 7.10.
- [5] Jan Staszak, Krzysztof Ludwinek, Marek Jaškiewicz, Marek Gaj: Influence of moment of inertia on PMSM and SRM rotational speed transients. Problems of maintenance of sustainable technological systems, Tom IV, Komitet Budowy Maszyn, Sekcja Podstaw Eksploatacji. pp. 152-164, Kielce 2012.
- [6] M. Jaškiewicz, K. Ludwinek, J. Staszak, T. Suliga.: Possibilities of Graphical Environment Application for Determining Parameters of the Mechanical System, *Journal of KONES Powertrain and Transport* Vol. 18, No. 4, pp. 151-164, Warszawa 2011, ISSN 1231-4005.



Mechanisms of non-thermal effects of low-frequency electromagnetic field on biological cells

* Ivona Malíková,

* Department of Electromagnetic and Biomedical Engineering, Faculty of Electrical Engineering, University of Žilina, Univerzitná 2, 01026 Žilina, Slovakia, ivona.malikova@fel.uniza.sk

Abstract. The article discusses non-thermal effects of low frequency electromagnetic field. Mechanisms by which low-frequency electromagnetic field affect cells of biological systems vary a lot. This review explains selected roles of magnetic field in the cells metabolism. In this paper, there is the basic explanation of ion cyclotron resonance, but it also deals with the theory that considers ion parametric resonance in a cell membrane.

Keywords: low-frequency electromagnetic field, biological cell, ion cyclotron resonance, ion parametric resonance

1. Introduction

Life on the Earth is connected with electric and magnetic fields since inception. The life would be impossible without their activity. If there were no magnetic field of the Earth, the entrance of any essential molecules to the cell would be impossible. This field enables metabolism, transfiguration and excreting products in a cell.

In these days electromagnetic field and its radiation acquires increasing attention with growing use of electric machines and devices. When electric current flows in a conductor or coil, an artificial magnetic field arises around them. Vice versa, if variables of magnetic field effect on conductor or also on alive neural, muscular or another cell, electric field appears here. This phenomenon (electromagnetic flux density) has major role in explaining of effect of magnetic field on biological structure [1].

Considerable effects of electromagnetic field are thermal and non-thermal effects. The thermal effect is evident, but theories about the non-thermal effects diverge. This particle is focused on non-thermal effects and particularly on two theories considering ions that are influenced by low-frequency electromagnetic field.

2. Non-thermal effects of low frequency electromagnetic field

Even weak electromagnetic field (EMF) can give biological effects without generating consequential heat. EMF reduces the stability of living cells membranes which have mostly negatively charged molecules intermingled with positive charged ions that bind them together. In biological tissue there are some metallic ions, e.g. calcium, potassium, magnesium. For example potassium with monovalent ions (having one charge) has lower impact on binding than calcium with divalent ions (with two charges) [2]. It has been showed that EMF can remove calcium ions from cell membranes, what can reduce their stability, but in next experiments, it has been found that the effect occur only in very weak EMF and only in certain 'amplitudes windows', below and above which there is no effect. Next researchers, Tsejšlier et al., monitor adenosine triphosphatase (ATPase) activity. After short time exposure of protein solution the effect of extremely low EMF was decreasing on ATPase activity comparing to control samples, which weren't exposed to an artificial

EMF. This effect can be explained by EMF influence on dynamic properties of actomyosin solutions based on spontaneous dynamic formation of structure [3].

2.1. Ion cyclotron resonance

The cyclotron resonance is named after an early type of particle accelerator – cyclotron. The basic principle is illustrated in Fig.1. The magnetic force that is induced by two electromagnets at top and bottom bends the moving charge between the two halves (dee). The charge at each gap is accelerated by square wave electric field. The charge spirals outward increasing in speed. The time for completing one orbit is called cyclotron frequency. Ion cyclotron resonance (ICR) occurs when ions move in a static magnetic field such as magnetic field of the Earth. They are deflected sideways by the magnetic field and go into orbit around its lines of force at a frequency that depends on the charge to mass ratio of the ion and the strength of the static field [4]. If they are concurrently exposed to an alternating field at this frequency, they absorb its energy and the diameter of their orbits is increased, which multiply their energy of motion and chemical activity. Potassium is the massive positive ion in cell sap, where it outnumbers calcium by approximately 10.000 to 1. This makes potassium resonance in ICR particularly important. This ion is the most likely to replace any calcium that has been lost by electromagnetic exposure. The increasing of potassium chemical activity will increase its ability to replace calcium, so the rate of calcium loss from the membrane is higher what reduce its stability [4].

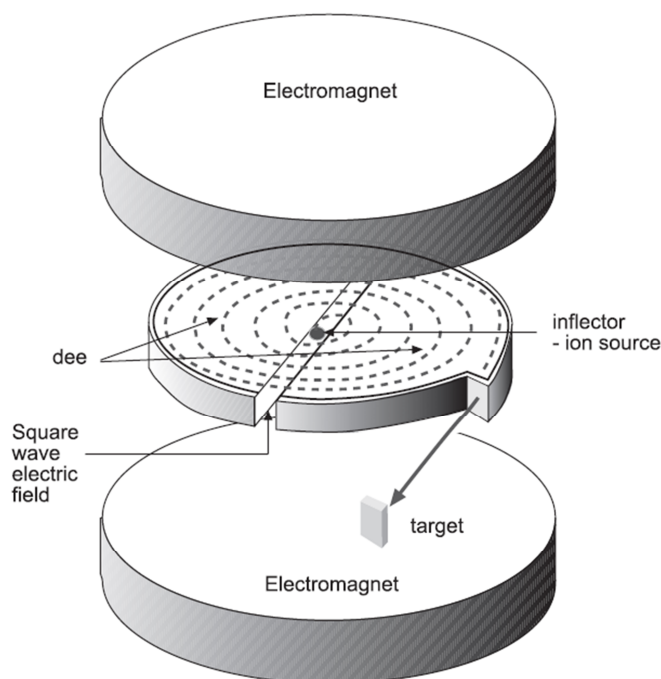


Fig. 1. The principle of cyclotron resonance.

Liboff claims, that ion channels in the cell membrane would shelter the ions from the strong thermal motion outside the membrane. In this part, external forces as cyclotron resonance would be able to decrease the signal-noise ratio. The model works with cyclotron frequency, which is able to accelerate a Ca^{2+} ion moving on curved pathway. The force is based on the Lorentz force. This force tends to bend the path of a charged ion moving in constant magnetic field (MF). If the charges start to circulate, they can gain energy from an alternating field and MF strength. This resonance occurs at frequencies of 10 – 100 Hz for Ca^{2+} ions [5].

2.2. Ion parametric resonance

The ion parametric resonance (IPR) model predicts that distinct patterns of field-induced biological responses will occur at particular magnetic field combinations which establish ion resonances. An important characteristic of resonance is the bandwidth response of the system, in part because it determines the required tolerances of the test system. Initial development of the IPR model used literature data to estimate the bandwidth for any ion resonance to be $\pm 10\%$ of its exact resonance.

Lednev's theory uses the phenomenon of Zeeman splitting of excited states of bound ions by a static MF (nonlinear effect). A model in the outline of the radical pair mechanism in hydrogen is shown in Fig.2. The spectral lines of the transition from $n = 3$ to 2 divide (into three lines at 0 or at two lines at 1 or -1) when an external MF is applied. The transition is according to the selection rule which does not allow a change of more than one unit in the quantum number m_1 .

Extremely low frequency (ELF) EMF might modulate these states, and thus be a mechanism for MF interaction with Ca^{2+} and other cations bound to biomolecules. Binhi in 1997, suggested the ion interference model, based on the interference of nonlinear energy states of bound Ca^{2+} [4].

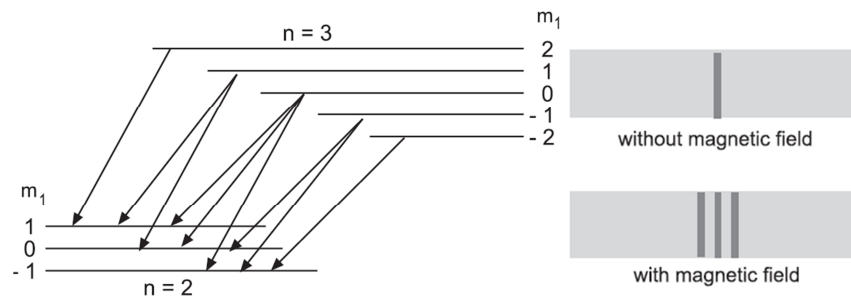


Fig. 2. Principle in Zeeman effect in hydrogen.

There are also a critics of IPR and allege some critical failures of the IPR. One of them is Adair in 1992. One of the deficits he noted is that the forces that contain the ion must be spherically symmetric. In heterogeneous environment of biological systems, such symmetry is not credible and the states that are split by the Zeeman effect are not split in different ways with larger magnitudes what destroy any IPR effect.

After this criticism, in 1995, Blackman and Blanchard improved this model of IPR. They predict different MF interactions with biological systems based on selective relation among four factors: flux density of static MF, frequency and flux density (B_{ac}) of parallel alternating current MF, and charge-to-mass ratio of ions in biological relevance [6]. Their research with nerve cells demonstrates that MF can interact with biological systems. The result supports model of IPR and its ability to predict relative changes in inhibition for each cycle and the intensities when the null effect occurs.

3. Conclusion

The effect of electromagnetic field with low frequencies is still much discussed. It has potential to be used in medicine or in other fields of studies of biological cells. The models of ICR and IPR, we mentioned in this article, are two models from many theories how EMF might influence biological system. ICR deals with cyclotron frequency and IPR covers invoke precession of ions depending on the orientation of the MF what are two different points of view. That's why supplementary work is needed. In the future it should be found out which one of these theories is closer to right and what is actually happening in cell during the exposition of EMF.

References

- [1] CHVOJKA, J. *Magnetoterapie v teorii a praxi*. Praha: Professional Publishing, 2000. 99s. ISBN 808-641-9010
- [2] GOLDSWORTHY, A. *The Biological Effects of Weak Electromagnetic Fields*. 2012 <http://www.hese-project.org/hese-uk/en/niemr/resonance1.php>
- [3] TSEĬSLIER, I. *Effect of electromagnetic field of extremely low frequency on ATPase activity of actomyosin*. *Ukrainskiĭ biokhimicheskiĭ zhurnal*, vol. 84, p.62-7, Sept-Oct 2012
- [4] BLACKMAN, C. F., BLANCHARD, J. P. *Experimental determination of hydrogen bandwidth for the ion parametric resonance model*. *Bioelectromagnetics*, vol. 20, p.5-12, 1999
- [5] FUNK, R. H.W., MONSEES, T., Ozkucur, N. *Electromagnetics effects – From cell biology to medicine*. *Progress in Histochemistry and Cytochemistry*, vol.43, p.177-264, 2009
- [6] BLACKMAN, C. F., BLANCHARD, J. P. *The ion parametric resonance model predicts magnetic field parameters that affect nerve cells*. *The FASEB Journal*, vol.9, p.547-550, April 1995



The Application for Hybrid Power System Data Evaluation

*Jakub Maňas **Petr Bilík

* VŠB- TU Ostrava, Faculty of Engineering and Computer Science, Department of Cybernetics and Biomedical Engineering, 17. listopadu 15, Czech Republic, {Jakub.Manas}@vsb.cz

** VŠB- TU Ostrava, Faculty of Engineering and Computer Science, Department of Cybernetics and Biomedical Engineering, 17. listopadu 15, Czech Republic, {Petr.Bilik}@vsb.cz

Abstract. In conference EPE 2011 was presented the monitoring system to measure and visualize the performance parameters of the hybrid power system. Now we would like to present data analysis results computed by developed application. The application reads the measurement data (it has been acquired for more than year) from the monitoring system. This data is transformed to power flows in the individual branches, equipment's power factors and performance parameters in the graphs. The application is currently used for hybrid power system review. The paper describes achieved results and needs for further improvements of such solution.

Keywords: Hybrid Monitoring System, Data Analysis, SW.

1. Introduction

A hybrid power system consisting of two photovoltaic and two wind power stations came to existence last year at VŠB-TU Ostrava. As its behaviour has to be monitored, the need for measurement and visualization at the hybrid system arose. The article describing the monitoring system was presented at Conference EPE 2011 and its brief summary is found in Part 2. Now, the hybrid system has been in operation for more than year and a lot of valuable data have been collected since then. Therefore, the application for evaluation of the measured data, which this article wants to cover, has been created.

2. The hybrid power system by VŠB-TU Ostrava

The hybrid power system consists of two photovoltaic and two wind power stations that together charge the accumulator battery. The battery is also used for the feed of two lamps of the public lighting. The block diagram of the system is in Fig. 1.

The hybrid system uses two photovoltaic panels of whose performance is 130 W (FV1) and 200 W (FV2). The transmission of the energy from the FV panels to the batteries is controlled by the regulator (REG). The wind power station VT1 uses for the conversion of wind energy to electrical energy a 200 W generator with a built-in regulator of charging, so the regulator can be connected directly to the batteries. At VT2 is, on the other hand, used a 200 W synchronous 3-phase system generator, whose performance is transferred to the battery via the rectifier and the regulator (the block with the diode, see Fig. 1). The appliances in the system are represented by two lamps of the public lighting (VO1 and VO2). VO1 is an LED lamp with the input of 40 W and VO2 is a sodium-vapour lamp with the input of 50 W. Both lamps are operated with the voltage of 230 VAC, which is supplied there by the DC/AC converter. The battery consists of NiCad accumulators and its resulting capacity is 340 Ah at the nominal voltage of 12 VDC. [1]

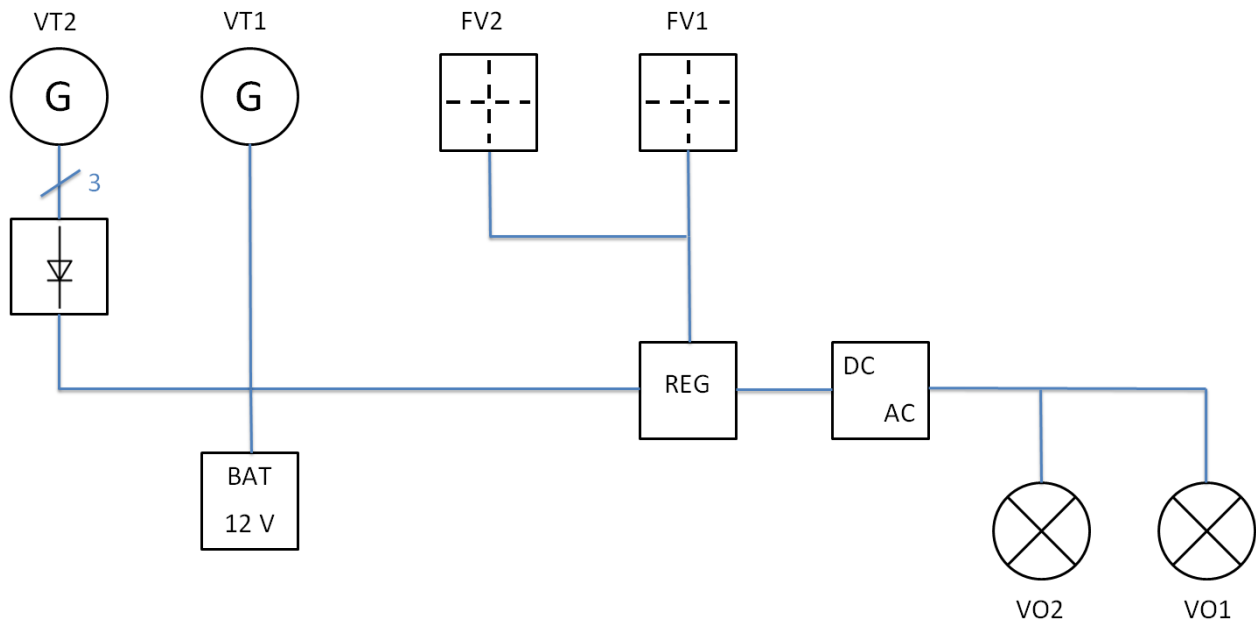


Fig. 1. The block diagram of a hybrid power system [1].

3. The monitoring system of the hybrid power system

The monitoring system is built on the HW platform NI CompactRIO. The voltage and currents in all branches of the circuit are measured, except for the appliances (the input of VO1 and VO2 is measured together). The individual measuring points are shown in Fig. 2. The monitoring system does not take any electrical energy from the batteries of the hybrid power system; its feeding is dealt with separately and provides uninterrupted operation (UPS). [1]

All the measuring HW is located in the existing outdoor distribution box where there is the whole electrical equipment of the hybrid power system. This box provides protection against weather conditions, but it is not thermally insulated. This places increased demands on the operating temperature of each component. All the components are placed on a metal structure located in the box. The dimensions of the free internal space of the box must be taken into consideration when choosing the components and the layout design. [1]

The measured data are stored in text files (daily records). The current measured data are visualized on the website by means of a web server (Fig. 3), which is operated on a remote PC. The data are also backed up on the PC and can be downloaded by authorized users with the help of the FTP access.

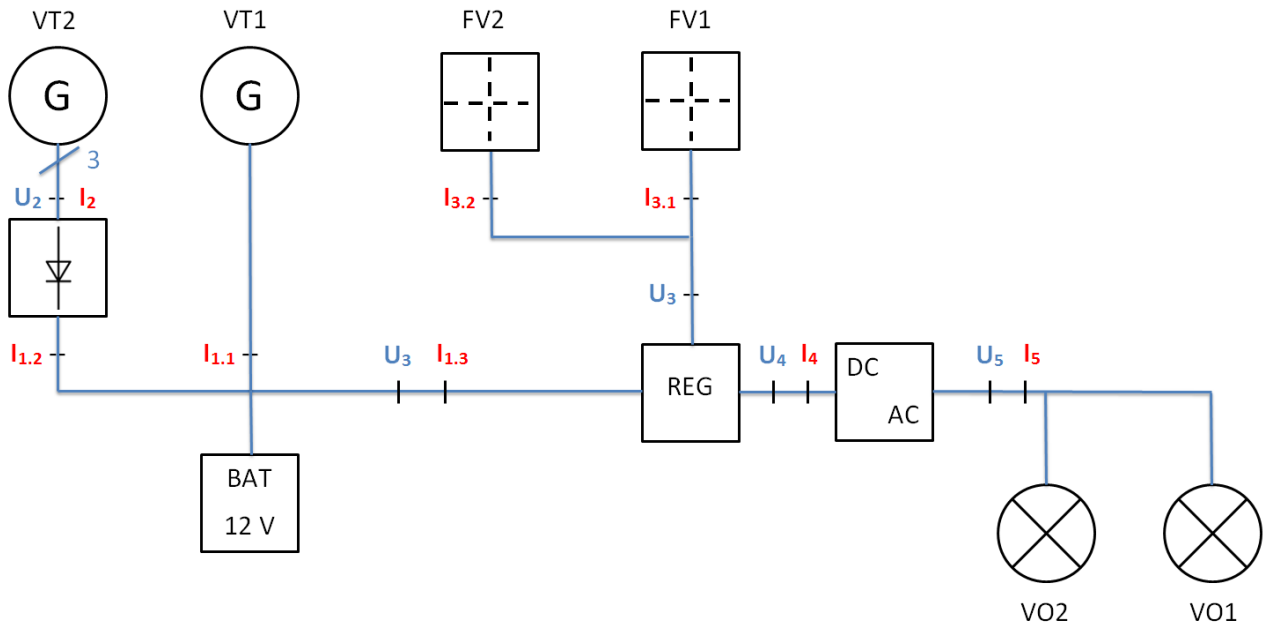


Fig. 2. The block diagram of the measured system and the measuring points [1].

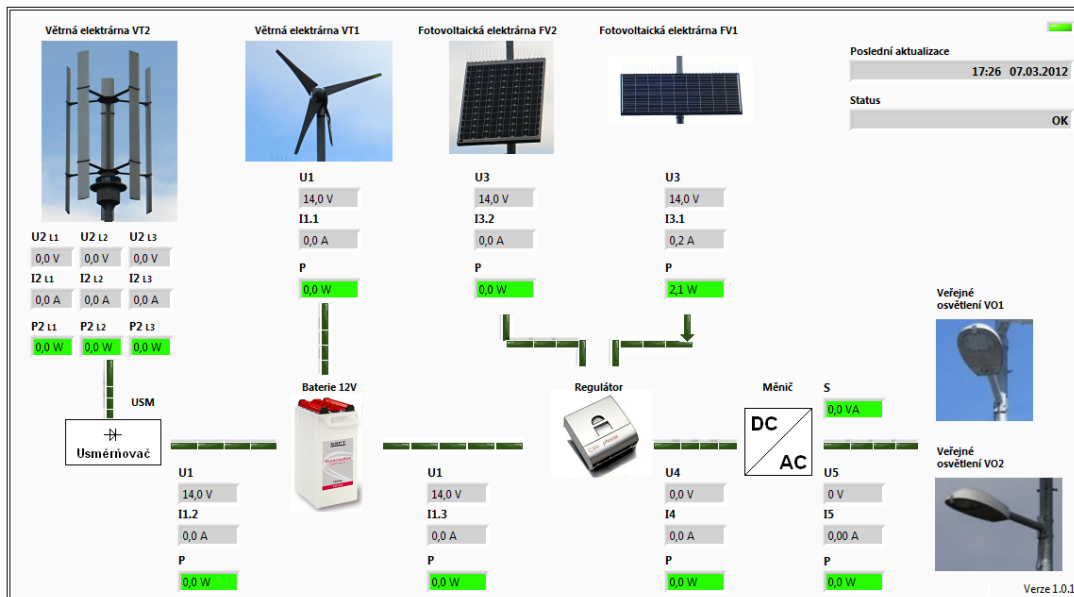


Fig. 3. Visualization of the measured data with the help of the web interface.

4. Application for evaluation of the measured data

The developed application for evaluation of the measured data (application) enables graphical display (Fig. 4) of the measured and computed data (performance streams, component efficiency). The users can specify the accurate time period (the minimum resolution is 1 day) or they can choose from the menu “The last 3 days”, “The last week”, ..., “The last year” (Fig. 5). The application enables to display up to 4 parameters in the graph at the same time, when each parameter has its own vertical axis with its scaling.

The application then processes these data statistically so that the data are divided into certain time parts so that the total number of samples to the graph was approximately a thousand for each course of the parameter. The algorithm of searching for the minimum and maximum value of the parameter and their display together with their time in the correct order is the reduction of the data.

The displayed data can be exported in the form of a picture, MS Excel table, text file and TDMS file (for data processing in the application NI DIAdem).

In a simplified way, developed application is data reader, so its accuracy and reliability are related to the monitoring system. If data files are corrupted (for example unexpended restart of the monitoring system), developed application ignores the corrupted data blocks. If the sought-after parameter is not found in the measuring files and is not located in other files, this day is filled in the data with an invalid value that is not displayed in the graph. In case of low current amplitudes, power evaluation is inaccurate, so users can set power thresholds in application settings to ignore the inaccurate results.

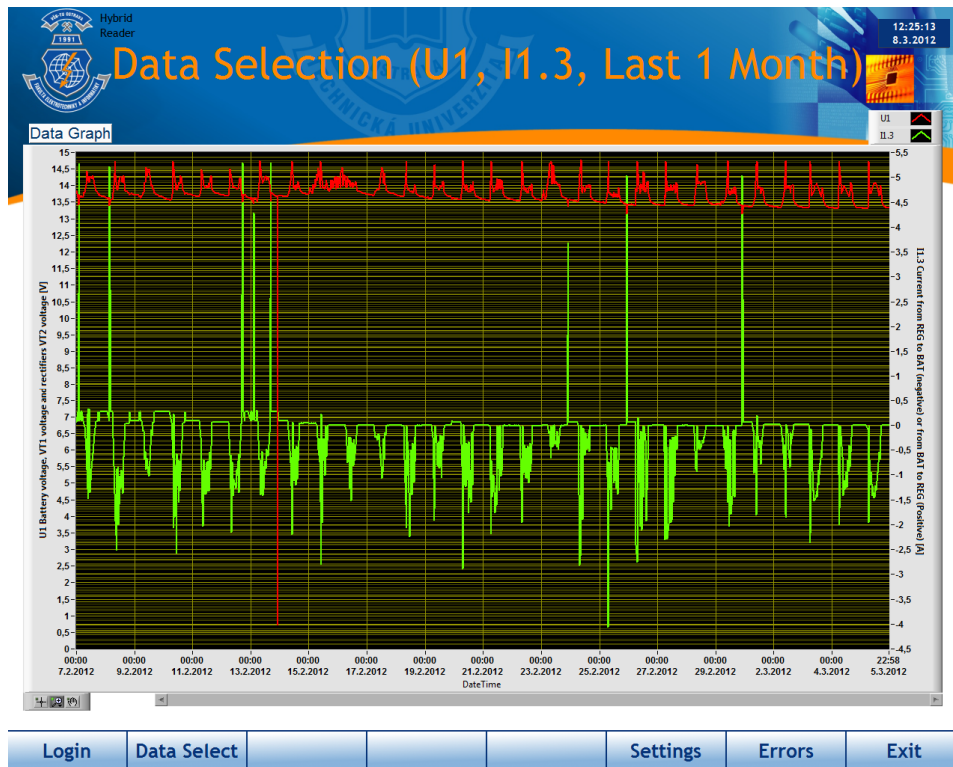


Fig. 4. GUI of the application created for the display of the data evaluated in the graph.

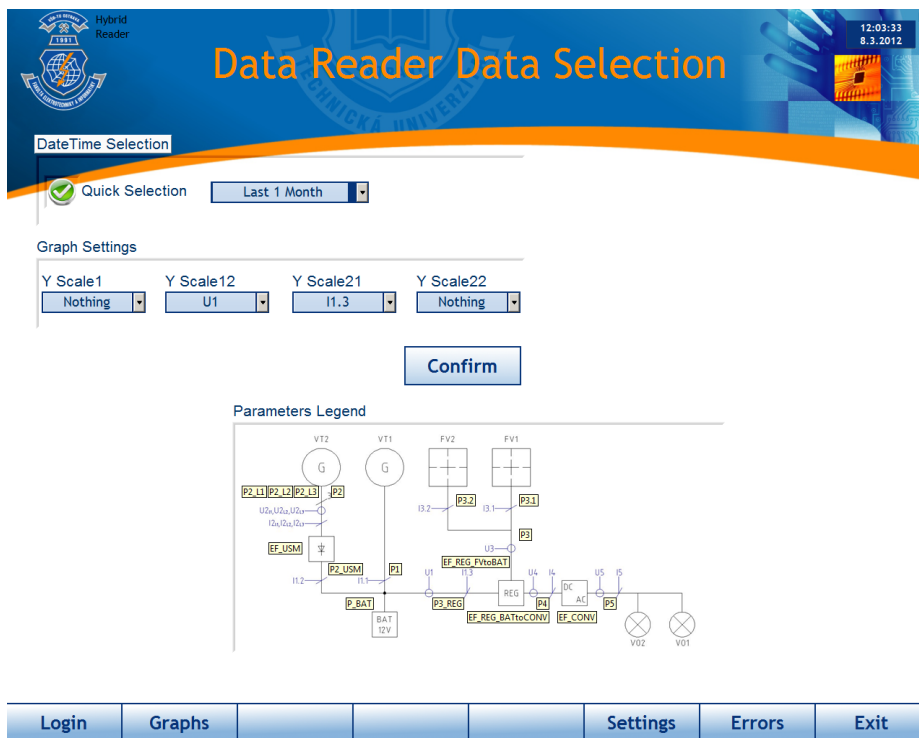


Fig. 5. GUI of the application created for the evaluated data selection.

5. Conclusion

The goal of this article was to describe the developed application for evaluation of the measured data from the hybrid power system consisting of two photovoltaic and two wind power stations.

The application allows an easier and more efficient analysis of phenomena in the hybrid system at VŠB-TU Ostrava. When the application NI DIAdem for the analysis of the measured data is used, the compilation of measurement protocols will be faster as well. These significant time savings enable the users to concentrate their time and energy on substantial issues during the research of the hybrid system.

Future development of the application will focus to create algorithms for more complex data analysis in the hybrid system.

The application uses the concept of virtual instrumentation, so it is expandable according to the future requirements without the need of higher time sources.

Acknowledgement

This work was partly supported by European operational program “Slovakia - Czech Republic 2007-2013”, project name “Collaboration between University of Zilina and VSB-TU Ostrava in increasing of quality of education and preparation of researchers in the area of electrical engineering”, project registration number 22410320029.

References

- [1] KVAPIL, Jakub; BILÍK, Petr; MIŠÁK, Stanislav: *Monitoring system of the hybrid power system* (Monitorovací systém hybridního napájecího systému). In *Proceeding of the 12th International Scientific Conference Electric Power Engineering 2011*. Kouty nad Desnou : VSB- Technical University of Ostrava, 2011. s. 1-3. ISBN 978-80-248-2393-5.
- [2] *National Instruments - Test and Measurement* [online]. 2010 [cit. 2012-05-03]. Dostupné z WWW: www.ni.com



Permanent Magnet Synchronous Motor Inductance Characteristics Investigation

*Marek Mušák, *Marek Štulrajter, *Valéria Hrabovcová, *Peter Dúbravka
*University of Žilina, Faculty of Electrical Engineering, Department of Power Electrical Systems,
Univerzitna 1, 01026 Žilina, Slovak Republic,
Marek.Musak@fel.uniza.sk, Marek.Stulrajter@fel.uniza.sk,
Valeria.Hrabovcova@fel.uniza.sk

Abstract. The main aim of the presented paper is to show an approach for inductance characteristics investigation in a permanent magnet synchronous motor (PMSM). As it is known, the magnetically nonlinear behavior of PMSM motors is characterized by current dependent magnetic flux linkage characteristics. In this work, the current dependent inductance characteristics that reflect the magnetic nonlinearity are measured. Both direct and quadrature axis synchronous inductances can be investigated over the entire operational area of the PMSM motor by applying a strategy described in the paper.

Keywords: d- and q- axis synchronous inductances, PMSM motor, saturation, characteristics

1. Introduction

The electric motor parameters determination is highly required for the purpose of accurate modeling and performance analysis of particular machines and/or their control approach. From motor control perspective the standard control strategies up to base speed do not require the current dependent inductance characteristics. The inductance parameters can be taken from either the motor datasheet or acquired from simple measurement neglecting the saturation phenomenon. However, there are plenty of advanced motor control techniques working in extended operational area such as field weakening control where motor works over the base speed or maximum torque per amper (MTPA) where partial field weakening is applied in order to take a benefit from the reluctance torque. Additionally, tons of model based algorithms such as observers and estimators require as precise motor parameters as possible.

Nowadays, there are plenty of various methods that can be used for the parameters evaluation [1, 2], [6], [8, 9]. The parameters can also be directly measured using a proper device, for instance, the RLC meter. However such approach is sufficient only for rough measurement and it is not recommended for very precise and complex measurement due to scale or range limitation, mid-level accuracy, low test current [3] and so on.

2. DQ Model in Stationary Reference Frame

The main purpose of the presented algorithms is to provide dq model parameters from physically measured data, mainly focusing on the inductance characteristics. Therefore, a two phase orthogonal dq model in synchronous reference frame has been used to analyze the synchronous reluctances of the machine. The mathematical model of PMSM motor is as follows:

$$\begin{bmatrix} u_d \\ u_q \end{bmatrix} = R_s \begin{bmatrix} i_d \\ i_q \end{bmatrix} + \begin{bmatrix} L_d & 0 \\ 0 & L_q \end{bmatrix} \frac{d}{dt} \begin{bmatrix} i_d \\ i_q \end{bmatrix} + \omega_e \begin{bmatrix} 0 & -L_q \\ L_d & 0 \end{bmatrix} \begin{bmatrix} i_d \\ i_q \end{bmatrix} + \omega_e \psi_{PM} \begin{bmatrix} 0 \\ 1 \end{bmatrix} \quad (1)$$

where R_s is stator phase resistance, L_d and L_q are synchronous inductances in dq frame and ψ_{PM} represents a flux of permanent magnets. Considering the rotor locked during the test, the cross-coupling terms in both d- and q-axis as well as the back-EMF voltage component in q-axis are eliminated and the PMSM model is linearized and simplified as follows:

$$\begin{bmatrix} u_d \\ u_q \end{bmatrix} = R_s \begin{bmatrix} i_d \\ i_q \end{bmatrix} + \begin{bmatrix} L_d & 0 \\ 0 & L_q \end{bmatrix} \frac{d}{dt} \begin{bmatrix} i_d \\ i_q \end{bmatrix} \quad (2)$$

From motor control point of view, the equation (2) describes the model of the plant for d and q current loop. Electrical torque in dq reference frame is developed by contribution of synchronous and reluctance torque, and is derived as follows:

$$T_e = \frac{3}{2} p (\psi_{PM} i_q + (L_d - L_q) i_d i_q) \quad (3)$$

2.1. Connection scheme and rotor alignment

Most of the industrial PMSMs do not have the mid-point of the Y-connected winding freely accessible and therefore the only line-to-line quantities can be measured and evaluated as motor parameters.

Respecting the mutual magnetic coupling between the three phases of the motor, the stationary tests with single-phase excitation is provided according to the scheme in Fig.1 [3]. For d- and q-axis synchronous inductances investigation, the rotor must be locked at specific position to the armature flux. For d-axis measurement the rotor flux ψ_{PM} must be aligned with the resulting armature flux ψ_{ABC} and for q-axis measurement the angle between rotor flux and resulting armature flux must be 90 degrees, Fig.1.

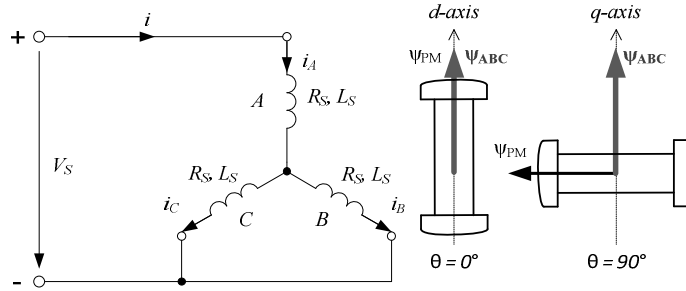


Fig. 1. Connection scheme arrangement

To reach the precise rotor position at d-axis and q-axis, respectively, the alignment procedure must be performed. The easiest way is to apply DC voltage as an excitation signal to the terminal of the motor. Such excitation creates a static armature flux that pulls the rotor to its position. More details are in [8, 9].

Having the rotor properly aligned with either d- or q- axis, the motor is fed by testing voltage signal. Based on the current feedback the circuit inductance is calculated.

3. Motor Parameter Characteristics

As it has been mentioned, this article focuses only on the methods for current dependent inductance characteristics measurement. Proposed approach of synchronous inductances measurement assumes the connection scheme shown in Fig.1. Since the stator winding is Y-connected without any neutral line for external access, the only line-to-line value can be measured. When the rotor's d-axis/q-axis are aligned with the stator phase A, the synchronous inductance L_d and L_q can be derived from equivalent line-to-line inductance L_{L-L} as two-thirds of L_{L-L} , depending

on the rotor angle θ . This assumption can be accepted only in case of simplification, where the mutual inductances are not taken into account.

Since inductance in the motor is also subject of saturation phenomena, the way to correctly monitor the inductances is to measure them at various current levels. The nonlinearity $\psi=f(i)$, $L=f(i)$ are caused by the saturation of iron parts of the stator and has the same shape as magnetizing curve $B=f(H)$. This dependency is described in Fig.2, where the relations $\psi=f(i)$, $L=f(i)$ in both axes are presented.

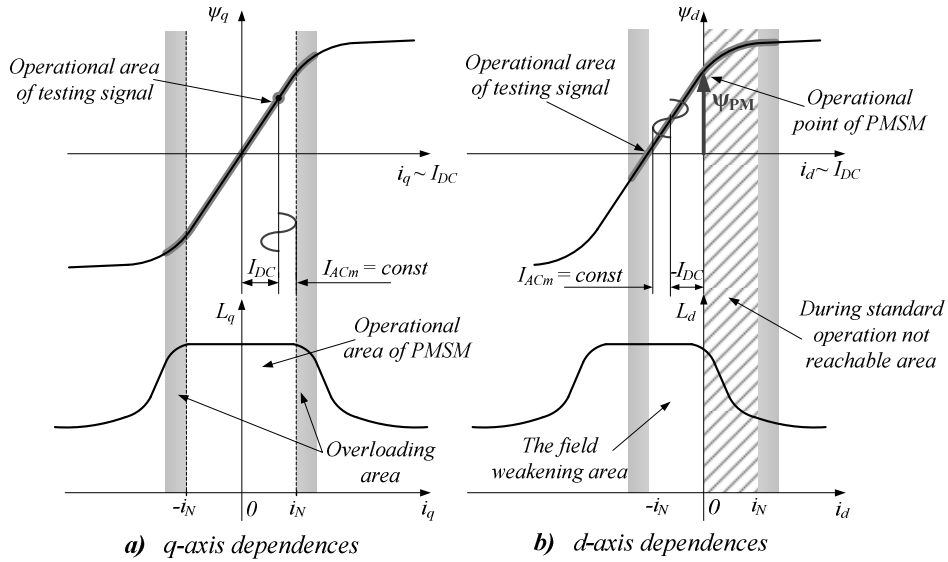


Fig. 2. The effect of saturation, ψ_{dq} and L_{dq} as a function of i_{dq}

To analyze the effect of saturation in q-axis, Fig.2a, the rotor q-axis has to be aligned with the stator phase A. If the motor is assumed to be under vector control, with no field weakening $i_d=0$, the increasing load will result in increased stator current in q-axis. When there is no load applied to the rotor, $i_q=0$, the linkage flux $\psi_q=0$. Increasing load results in an increase of i_q and ψ_q , and will cause saturation of the stator teeth around q-axis, which in turn decrease L_q .

To analyze the effect of saturation in d-axis, Fig.2b, the rotor d-axis has to be aligned with the stator phase A. All the flux existing in the machine is created purely by the permanent magnets and therefore the area around d-axis is mildly saturated even if there is no current flowing through the stator winding. As seen in Fig.2b, if magnetizing current i_d increases a magnetizing effect will occur and the area of stator around d-axis will be even more saturated with lowering L_d . And vice versa, if magnetizing current i_d decreases a demagnetizing effect will occur and the area of stator around d-axis will be less saturated with increasing L_d , [8, 9].

4. Motor Inductances Characteristic Measurement

Currently, there are several approaches to investigate the PM motors characteristics including the inductance characteristics [5, 6, 7]. Based on the previous research activities [8, 9], authors have decided to focus on a method where the excitation AC signal is summed with the DC signal, Fig.2. AC signal amplitude and frequency is kept constant while the DC voltage signal is adjusting such a way, that the rated current will flow through the motor circuit. The range of DC current should be $I_{DC} = (-1,2I_N \div 1,2I_N)$, [8, 9].

After DC component elimination from current and voltage signal, the RMS value is calculated. Having the RMS values and the phase shift ϕ between the AC voltage signal and AC current signal, the inductance is calculated as follows:

$$L_{d(\theta=0^\circ)} = L_{q(\theta=90^\circ)} = \frac{2}{3} \frac{1}{2\pi f_{test}} \frac{V_{RMS}}{I_{RMS}} \sin(\varphi) \quad (4)$$

Equation (4) is sensitive to the phase shift φ . In order to extract this value from the waveforms as precise as possible a proper technique has to be used.

The experimental results can be seen in Fig.3. Since the motor has $p=3$, there are three d/q axis alignment along the rotor mechanical revolution.

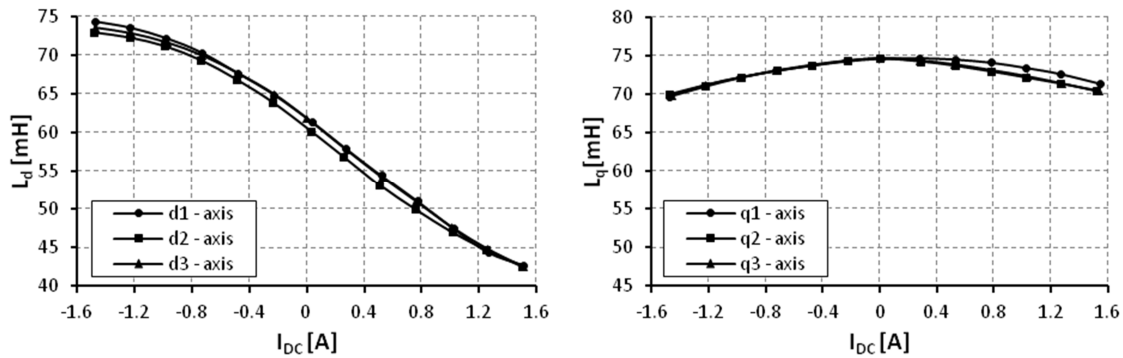


Fig. 3. The current dependent inductance characteristics

The proposed method has been verified on the high-voltage PMSM motor, DutymAX 75DSA, with following parameters:

P	= 0,38kW	T _N	= 1.2Nm	R _S	= 36.7 Ω
U _S	= 220V	n _N	= 3000 rpm	L _{2ph}	= 109mH
I _N	= 1.1A	J	= 0.0006kgm ²	p	= 3

Tab. 1. Parameters of tested high-voltage motor

5. Conclusion

The main purpose of the presented paper was to verify a method for inductance characteristic investigation that has already been introduced and verified on the low voltage PMSM motor in [8, 9]. In this paper an improvement in calculation and consequently the experimental verification on the high voltage PMSM motor can be seen. The experimental results confirm the theoretical assumption and the measured characteristics have expected behavior.

References

- [1] VAS, P.: *Parameter Estimation, Condition Monitoring, and Diagnosis of Electrical Machines*, Clarendon Press – Oxford, 1993, ISBN 0-19-859375-9
- [2] HRABOVCOVA, V, RAFAJDUS, P, HUDAK, P, FRANKO, M.: *Meranie a modelovanie elektrických strojov*, EDIS – Žilinská univerzita v Žiline, Žilina, 2004, pg.: 335, ISBN 80-8070-229-2
- [3] SOONG, W. L.: “Inductance Measurements for Synchronous Machines”, Power Engineering Briefing Note Series #2, 8 May 2008
- [4] OHM, Y, DAL.: *Dynamic Model of PM Synchronous Motors*, Drivetech, Virginia
- [5] WALKER, A., J., COSSAR, C., T. J. E. MILLER: *Simulation and Analysis of Magnetisation Characteristics of Interior Permanent Magnet Motor*, Acta Polytechnica Vol. 45 No. 4/2005, Prague
- [6] KAZEROONI, M., KAR, C., NARAYAN,: *Methods for Determining the Parameters and Characteristics of PMSM*, IEEE International Electric Machines & Drives Conference (IEMDC), 15-18 May 2011
- [7] Marcic T., Stumberger. G., Stumberger, B.: *Analyzing the Magnetic Flux Linkage Characteristics of Alternating Current Rotating Machines by Experimental Method*, IEEE TRANSACTIONS ON MAGNETICS, VOL. 47, NO. 9, SEPTEMBER 2011

- [8] STULRAJTER M., MUSAK M.,: *Unconventional methods for PM Synchronous Motor parameters investigation*, Elektro 2012, Rajecke Teplice, Zilina 2012
- [9] MUSAK M., STULRAJTER M., HRABOVCOVA V.,: *New approaches for parameters determinations of PM synchronous motor*, 12th International conference on Low voltage electrical machines 2012, October 15th-16th, 2012, Slapanice, Czech Republic, ISBN 978-80-214-4602-1



Oxygen Gas Sensors for Automotive Application

Lubomír Ostrica, Miroslav Gutten
 University of Žilina, Faculty of Electrical Engineering,
 Department of Measurement and Applied Electrical Engineering, Univerzitná 1, 01026 Žilina,
 Slovak Republic, {lubomir.ostrica, miroslav.gutten}@fel.uniza.sk

Abstract. Gas sensors have become an integral component of control systems for internal combustion engines to provide information for feedback control of air-to-fuel ratio (A/F) to achieve improved vehicle performance and fuel economy as well as decreased levels of emission. This report gives an overview on automotive exhaust gas sensors and proposal the diagnosis models for On Board Diagnostic system.

Keywords: Oxygen sensor, Fuel ratio, Diagnostic.

1. Introduction

When fuel is burned in the combustion chamber of an engine in addition to harmless products like water, carbon dioxide and nitrogen, some harmful emission, such as carbon monoxide, nitrogen oxides and hydrocarbons are also produced. The aim of the regulated catalytic converter is to reduce the amount of harmful substances. The lambda sensor plays a major role in enabling the catalytic convertor to fulfill this task because it guarantees the catalytic convertor optimal operating conditions. [1].

A stoichiometric mixture is the working point that modern engine management systems employing fuel injection attempt to achieve in light load cruise situations. For gasoline fuel, the stoichiometric air–fuel mixture is approximately 13:1, but Environmental Protection Agency regulations raised the ratio to 14:1 to allow the use of catalytic converters i.e. for every one gram of fuel, 14.7 grams of air are required (the fuel oxidation reaction is: $25/2 \text{ O}_2 + \text{C}_8\text{H}_{18} = 8 \text{ CO}_2 + 9 \text{ H}_2\text{O}$). Any mixture less than 14.7 to 1 is considered to be a rich mixture; any more than 14.7 to 1 is a lean mixture – given perfect (ideal) "test" fuel [1-3].

$$AFR = \frac{m_{air}}{m_{fuel}} \quad FAR = \frac{1}{AFR} \quad \lambda = \frac{AFR}{AFR_{stoich}} \quad \phi = \frac{1}{\lambda} \quad (1-4)$$

where: *AFR*–air fuel ratio, *FAR*–fuel air ratio, λ –air fuel equivalence ratio, ϕ – fuel air equivalence ratio.

Fuel	AFR _{st}	FAR _{st}	Equivalence Ratio	Lambda(λ)
Gasoline stoichiometric	14.7	0.068	1	1
Gasoline max power rich	12.5	0.08	1.176	0.8503
Gasoline max power lean	13.23	0.0755	1.111	0.900
E85 stoichiometric	9.765	0.10235	1	1
E85 max power rich	6.975	0.1434	1.40	0.7143
E85 max power lean	8.4687	0.118	1.153	0.8673

Tab. 1. Ratio fuel-air for petrol engines for different gasoline fuels

2. Oxygen sensors

There are basically three different types of lambda sensor. The zirconium dioxide and the titanium dioxide lambda sensors are also called switching, voltage jump, or “binary” lambda sensors, because two values depending on whether the fuelling is in a rich or lean state. The third type is the broadband lambda sensor. It is also known as “linear” lambda sensors because they have an output signal which is proportional to a wide range of air-fuel ratio, can accurately measure those ratios and the transitions between them. This paper is devoted only the first two types [3,4].

2.1. Zirconium dioxide oxygen sensor (switching sensor)

Currently the most commonly used automotive engine oxygen sensor is zirconia oxygen sensor. The sensitive component of it is made of zirconium oxide. There are the platinum electrodes on the internal and outer surface. A layer of porous ceramic is used to prevent the platinum corrosion by exhaust gas. The sensor on the outer sleeve is covered by a stainless steel, and there are some holes in each end of the sleeve, so that the internal platinum electrode is contacted with atmosphere and the outer platinum electrode is contacted with the engine exhaust. The structure is shown in Fig. 1 [4,6].

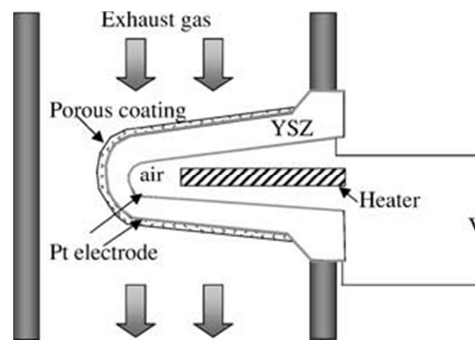


Fig. 1. Zirconia oxygen sensor’s schematic structure [4].

There are many holes in the zirconia ceramic body, so the oxygen can soak into the solid electrolyte, and oxygen will ionize when the temperature is higher than 350°C. When the oxygen content of the atmosphere in the internal side of the ceramic body is different from that of the engine exhaust in the outer side, the oxide ion will move from one side to the other side and a potential difference will emerge. The equation for calculation of the cell potential difference (sensor output voltage) is as follows [4]:

$$V_S = \frac{RT}{4F} \ln \frac{P_{O_2(atmosphere)}}{P_{O_2(exhaust)}} \quad (5)$$

where: R - universal gas constant; T - absolute temperature; F - Faraday constant; $P_{O_2(atmosphere)}$ - oxygen partial pressures of atmosphere; $P_{O_2(exhaust)}$ - oxygen partial pressures of engine exhaust.

The oxygen content of engine exhaust is high when the gas mixture is lean, so the oxygen concentration difference of the atmosphere and exhaust is small, so the output voltage is low (about 0.1V); but when the gas mixture is rich, there is little oxygen in the exhaust, the output voltage is high (about 0.8V). When the air-fuel ratio is close to the stoichiometric ratio (14.7), the oxygen content of the exhaust changes from redundancy to zero that leads to rapid change of the sensor’s output voltage[2-6]. The zirconia oxygen sensor’s voltage characteristic is shown in Fig. 2.

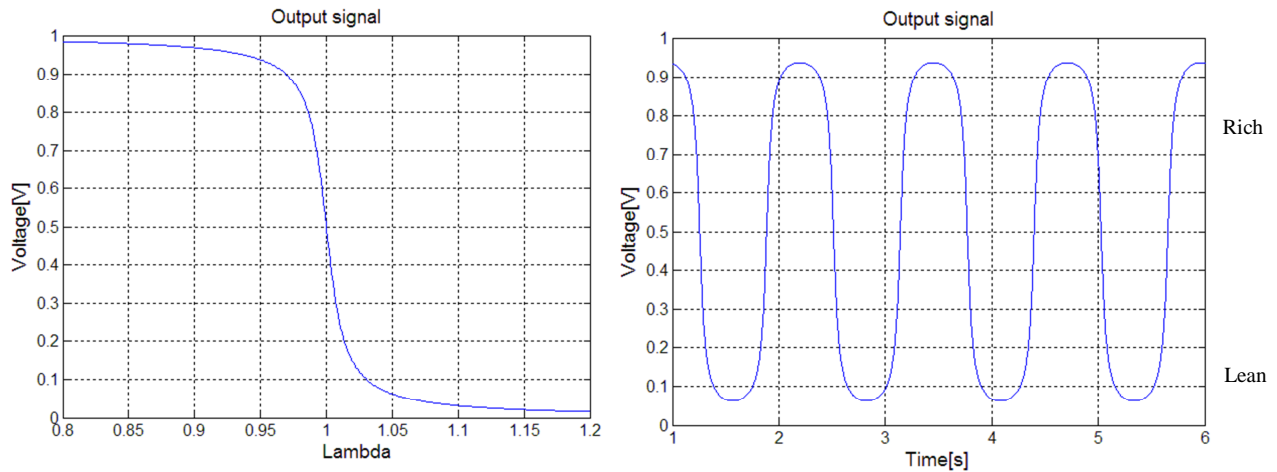


Fig.2. The zirconia oxygen sensor's voltage characteristic.

Mathematical equation for potential difference on zirconium sensor is:

$$V_s = \frac{-\arctan(100 \cdot (\lambda - 1))}{\pi} + 0.5 \quad (6)$$

2.2. Titanium dioxide oxygen sensor (switching sensor)

This type is known as a metal oxide sensor. Unlike zirconium dioxide lambda sensors, titanium dioxide lambda sensors do not self-generate a voltage. The ceramic element is a semiconductor, the electrical resistance of which varies relative to the residual oxygen concentration in the exhaust gas. Therefore by application of a voltage to the sensors a varying signal is produced depend on the oxygen concentration. All titanium dioxide lambda sensors have an integral heating element. By virtue of their design, they do not require access to ambient air for reference.

With a high oxygen concentration (λ greater than 1.0) the titanium dioxide is less conductive; with a low oxygen concentration (λ less than 1.0) it is more conductive. If a voltage is now applied to the element, the voltage changes according to the oxygen concentration in the exhaust.

The ideal operating temperature of this lambda sensor is 700°C [3].

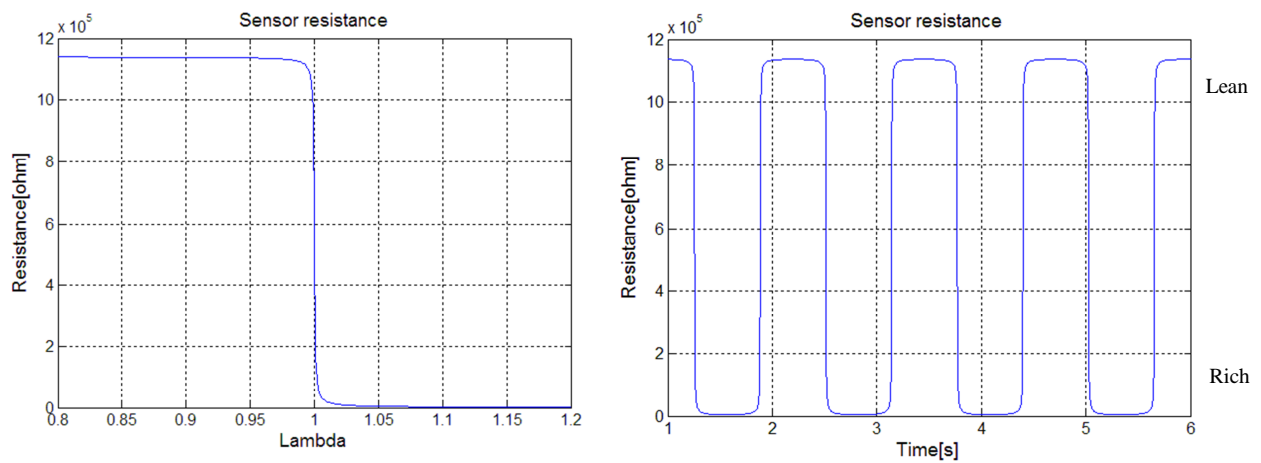
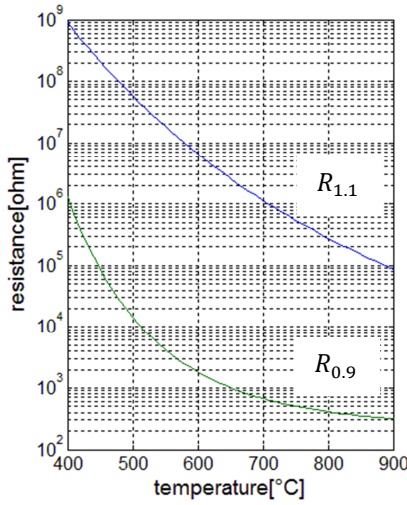


Fig. 3. Titanium dioxide oxygen sensor's resistance characteristic.

Following mathematical equations shows the change in resistance depending on the temperature for two different mixtures, for rich fuel mixture ($\lambda=0.9$) and for lean fuel mixture ($\lambda=1.1$):



$$R_{0.9} = 100 \cdot e^{\left(\frac{T}{1000} + 0.17\right)^{-4}} + 100 \quad (7)$$

$$R_{1.1} = 100 \cdot e^{\left(\frac{0.12 \cdot T + 202}{500}\right)^{-4}} + 100 \quad (8)$$

Fig. 4. Titanium dioxide oxygen sensor's resistance characteristic.

The formula calculating the resistance of the titanium dioxide oxygen sensor at operating temperatures 700 ° C depending on the value of lambda is:

$$R = (R_{0.9} + R_{1.1}) \cdot \left(\frac{-\arctan(2000 \cdot (\lambda - 1))}{\pi} + 0.5 \right) + R_{0.9} \quad (9)$$

3. Conclusion

The On Board Diagnostic checks the relevance of output signal of the oxygen sensor only in certain modes. However, there is the problem with the cold start the engine when the mixture is rich. At this time, the temperature sensor is still low. After heating the motor and sensor, control of fuel combustion begins to work. Management control unit enriches and impoverishes the mixture depending on the values of voltage sensor. Aging and dirt fouling is changing the sensor's parameters which results in influence of the fuel mixture. It is necessary to increase the lifetime of the sensor and control its response to the rich and lean mixture after the developed models.

References

- [1] VISSER, J. H., RICHARD, E., *Automotive exhaust gas sensing systems*, IEEE Transactions on Instrumentation and Measurement, vol. 50, no. 6, 2001
- [2] RIEGEL, J., NEUMANN, H., WIEDENMANN, H.-M., *Exhaust gas sensors for automotive emission control*. Exhaust Gas Sensor Development, Stuttgart, Solid State Ionics 152– 153 (2002) 783– 800
- [3] RAMAMOORTHY, R., DUTTA, P. K., AKBAR, S. A., *Oxygen sensors: Materials, methods, designs and applications*. Department of Materials Science and Engineering, The Ohio State University, Columbus. JOURNAL OF MATERIALS SCIENCE 38 (2 003) 4271 – 4282
- [4] DONGLIANG, W., KAISHENG, H., WEI, L., ZHIHUA, L., YINHUI, W., *OBD System Oxygen Sensor Degradation Monitoring and Mechanism Analysis*, 2011 Third International Conference on Measuring Technology and Mechatronics Automation.
- [5] WIEDENMANN, H.-M., HÖTZEL, G., NEUMANN, H., RIEGEL, J., STANGLMEIER, F., WEYL, H., *Exhaust gas sensors*, Automotive Electronics Handbook, 2nd edn., McGrawHill, New York, 1999, Chapter 6.
- [6] DENTON, T., *Advanced Automotive Fault Diagnosis*, 2nd edn., Elsevier Butterworth-Heinemann, Oxford, 2006, Chapter 5.



Electromagnetic Non-destructive Testing Using Advanced Magnetic Sensors

*Viera Pernisova, *Klara Capova

* Dept. of Electromagnetic and Biomedical Engineering, University of Zilina, Univerzitna 1, 010 26 Zilina, Slovakia, {pernisova; capova}@fel.uniza.sk

Abstract. The article deals with the advanced magnetic detection sensors used in nondestructive evaluation of materials. In this paper are described giant magnetoresistive (GMR) sensor, fluxgate sensors and coil as detection sensor in eddy current testing (ECT) probes. The article describes basic principles of used detection sensors and the experimental measurements with these detection sensors. The advantages and disadvantages of magnetic detection sensors are compared from both the frequency and the sensitivity points of view.

Keywords: nondestructive evaluation, eddy current testing, magnetic detection sensors, GMR, fluxgate.

1. Introduction

Eddy current testing (ECT) is one of the most often used nondestructive techniques for inspecting conductive materials and biomaterials at a very high speed that does not require any contact between the test piece and sensor. The principle of ECT is based on interaction between a magnetic field source and a test material. This interaction induces eddy currents in the examined object. The presence of cracks is monitoring by eddy current flow changes. The excitation field is generated by coil or by system of coils, but the key component in any EC probes is the detection sensor used to measure changes of response signal. There are several types of detection sensors, e.g. coil induction sensor or advanced magnetic sensors. Magnetoresistive sensors and fluxgate sensors belong to the group of magnetic sensors. In this paper there are used two types of magnetic sensors (GMR, fluxgate sensors) and coils sensor to compare their properties.

2. Giant magneto resistance (GMR) sensors

The basic principle of magnetoresistance effect lies on free charge movement influenced by external magnetic field. The result of this effect is the change of conductivity and magnetoresistance, too. Thus magnetoresistance can be defined as the change of resistance due to an external magnetic field. This change occurs by the movement of electrons in a very thin metal layer. This effect results from the Lorentz force which acts on electric charge e in homogeneous magnetic field.

Giant magneto resistance (GMR) demonstrated that the electric current in a magnetic multilayer consisting of a sequence of thin magnetic layers separated by equally thin non-magnetic metallic layers is strongly influenced by the orientation of the magnetizations of the magnetic layers (fig. 1). The cause of this giant variation of the resistance is attributed to the scattering of the electrons at the layers interfaces.

Fig. 2. shows a typical layout of commercial GMR magnetometer sensor. It is based on four GMR elements arranged in a Wheatstone bridge configuration. The resistor R_1 and R_3 are covered by metallic large plate structures which represents the magnetic flux shielding (flux concentrator).

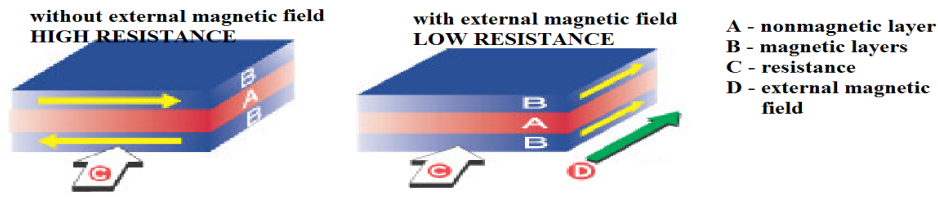


Fig. 1. GMR multilayer structure

For example if the magnetic field is applied, to GMR resistors (R_2 and R_4) resistance values decrease while the other GMR resistors under the flux concentrator remain constant. The imbalance of resistance is detected as output voltage change. GMR sensor integrated into small 8-pin chips was used for our measurements, [1, 2, 3].

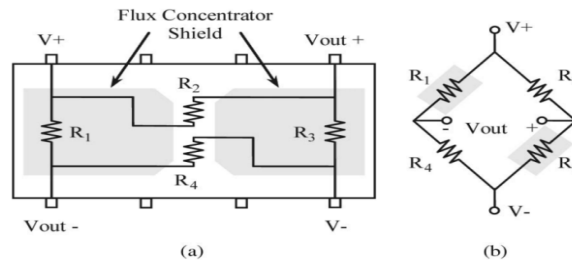


Fig. 2. (a) Sensor configuration and (b) Wheatstone bridge connection commercially available GMR magnetometers

3. Fluxgate sensors

Fluxgate sensors are used to measure the absolute strength of a surrounding dc magnetic field or low frequency ac magnetic fields. The sensors itself consists of a ferromagnetic core surrounded by a modulation coil which periodically saturates the probe core.

Fluxgate principle was first used in magnetic modulators. The excitation current through the excitation coil produces field that periodically saturates the soft magnetic material of the sensors core. In saturation the core permeability decreases and dc flux associated with the measured dc magnetic field is decreased. The name of the device comes from this "gating" of the flux that occurs when the core is saturated. When the measured field is presented, the voltage is induced into the sensing coil and it is detected as output signal, [4].

The main components of ECT probes for nondestructive testing are excitation coil or system of excitation coils and detection sensor such as GMR, fluxgate and detection coil

4. Experimental measurements

Conductive plate material is inspected and the specimen has a thickness of 10 mm having the electromagnetic parameters of stainless steel SUS 316L. This material is often used for implants realization and it has conductivity is $\sigma = 1.35$ MS/m and relative permeability is $\mu_r = 1$. The material contains five nonconductive defects with rectangular shape. The defects had a width of $w = 0.3$ mm, a length of $l = 10$ mm and their depth is varied $h = \{1; 3; 5; 7; 9\}$ mm (fig. 3).

The ECT probe consists of two excitation coils and one of the detection sensor, [5]. Two excitation coils are connected in series but magnetically opposite. The axes of coils are perpendicular to the evaluation material. The coils are driven by harmonic current with a value $I = 1$ A and two different frequencies $f_1 = 1$ kHz, $f_2 = 5$ kHz. Sensed component of magnetic field in given direction was measured to the output voltage. The detection sensors are placed in the center between the excitation coils with respect to the dimensions of all sensing elements.

One of the measuring configurations is shown in fig. 3. which means detection of defect on surface of specimen. The specimen is inspected along to crack length. The second configuration is the measurement of deep buried cracks. Excitation coils with detection sensors are placed on the

opposite side of the inspected material . The cracks are positioned in different depths $d = 1 \div 9$ mm with the step 2 mm. The excitation coils are driven by the same current as in the first configuration and frequencies are the same as well.

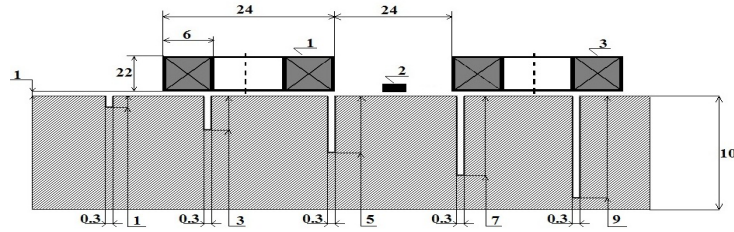


Fig. 3. Specimen with cracks and excitation-detection system; 1, 3 are excitation coils, 2 is detection sensor.

5. Results

The results of experimental measurements for the first configuration (surface scanning) are shown at fig. 4 and fig. 5. These figures show only selected resulting response signal for defects depths $h = 1$ and 3 mm.

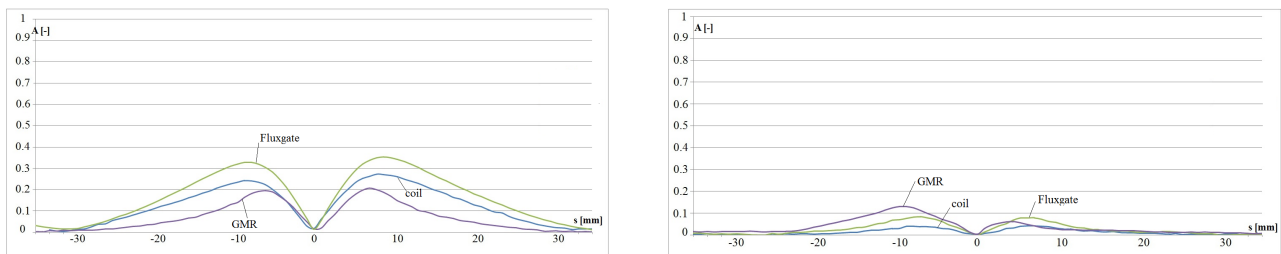


Fig. 4. Dependence of response signal (relative values) on probe position ($f = 1$ kHz, $h = 3$ mm and $h = 1$ mm)

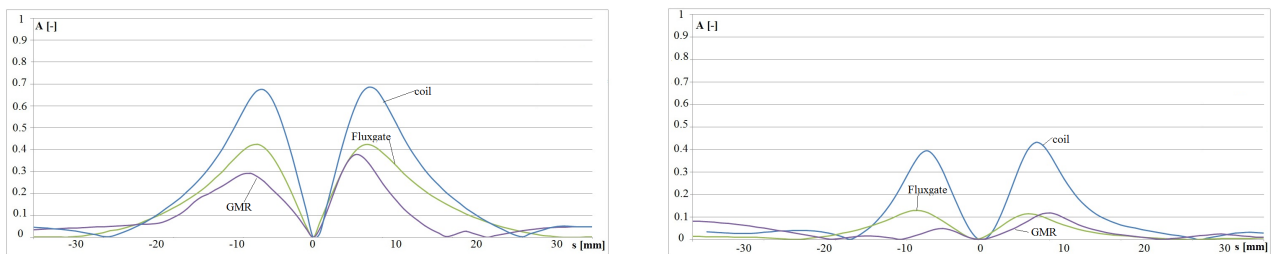


Fig. 5. Dependence of response signal (relative values) on probe position ($f = 5$ kHz, $h = 3$ mm and $h = 1$ mm)

The amplitude of response signal of 3 mm deep defect is higher than amplitude of 1 mm deep crack. Response signal has higher amplitude for excitation frequency 5 kHz coil sensing element and GMR detection sensors. The coil response signals at low excitation frequencies are lower than the GMR once because of the coil sensitivity at higher frequencies. GMR sensor has the best response signal for 1mm defect depth and excitation frequency $f = 1$ kHz. in compare with other sensing element.

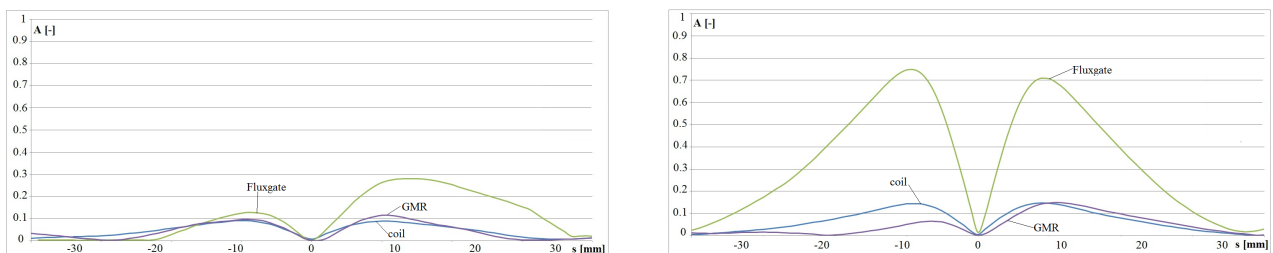


Fig. 6. Dependence of response signal (relative values, deep defects) on probe position ($f = 1$ kHz, $d = 3$ mm and $d = 1$ mm)

Results of experimental measurements for second configuration are shown in fig. 6 and 7. Defects which are situated in the depth $d = 1$ and 3 mm are reliably detected with all detection sensors. The deeper defect in the depth $d = 5$ mm is detected by use the coil and fluxgate detection sensors. The optimum excitation frequency was of $f = 5$ kHz.

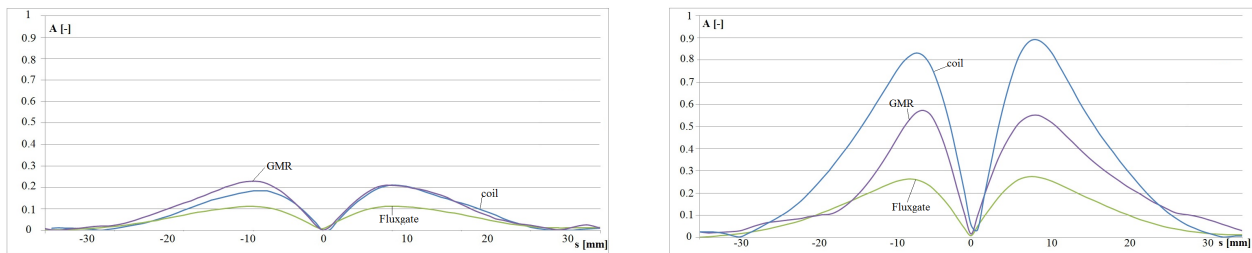


Fig. 7. Dependence of response signal (relative values, deep defects) on probe position ($f = 5$ kHz, $d = 3$ mm and $d = 1$ mm)

6. Conclusion

The aim of this paper is to introduce the advanced magnetic sensors for detection in nondestructive testing. The obtained response signals were measured and presented in the paper. In comparison with the use of coil the magnetic sensors have very similar response for this type of defects. The magnetic sensors are more sensitive to mechanic vibration of measuring apparatus and to the precision location of detection sensors. Magnetic sensors (mainly GMR) provide better response signal for a lower excitation frequency in compare with the coil. Sensitivity of coil increases with increasing excitation frequency. In the future we will continue in this work in order to obtain more complex information about defects using various types of detection.

Acknowledgement

This work was supported by the Slovak Research and Development Agency under the contract No. APVV-0349-10. This work was also supported by grants of Slovak Grant Agency VEGA, projects No. 1/0765/11, 1/0927/11.

References

- [1] REIG, C., CUBELLS-BELTRÁN, M. D, MUÑOZ RAMÍREZ, D.: *Magnetic Field Sensors Based on Giant Magnetoresistance (GMR) Technology: Applications in Electrical Current Sensing*, Sensors 2009, ISSN 1424-8220, p. 7920 - 7924
- [2] BETTA, G., FERRIGNO, L., LATACCA M.: *GMR- Based ECT instrument for detection and characterization of crack on planar specimen: A hand-held solution*, IEEE transactions on instrumentation and measurement, vol. 61, no. 2, February 2012, p. 505-512
- [3] CAPOVA, K., CAP, I., JANOUSEK, L., GOMBARSKA, D.: *Advanced probes for electromagnetic non - destructive testing*, proceedings of 54. Internationales Wissenschaftliches Kolloquium, 7th - 10th September 2009, ISBN 978-3-938843-45-1
- [4] MATKOVA, V., STRAPACOVA, T.: *Detection sensors for electromagnetic nondestructive evaluation*, ELEKTRO 2012, CD – ISBN 978-1-4673-1178-6
- [5] RIPKA, P.: *Advances in Fluxgate sensors*, ScienceDirect, Sensors and Actuators A 106, 2003 p. 8-14
- [6] SMETANA, M., JANOUSEK, L., STRAPACOVA, T., CAPOVA, K. *Comparison of detection capabilities between inductance detector and fluxgate magnetometers in ECT*. In *Electromagnetic Nondestructive Evaluation*, Vol. 36, Vol.2012, ISSN 1383-7281, pp. 227-232.



Testing gapless measurement of PQA according to IEC 62586-2

Petr Pětvaldský, Petr Bilík

*VŠB-TU Ostrava, FEECS, Department of Cybernetics and Biomedical Engineering, 17. Listopadu 15,
70833 Ostrava Poruba, Czech Republic, {petr.petvaldsky, petr.bilik}@vsb.cz

Abstract. This paper describes a tester for automated testing of power quality analyzers, focuses on evaluation of correct gapless and non-overlapping measurement according to standard IEC 62586-2 [1]. A test is used in order to verify the accuracy of the basic time window for evaluating RMS voltage values (10/12 cycle), and to evaluate whether during the measurements RMS samples (gapless) are not lost and mutual overlaps of individual cycles are not produced. The tester is based on principles of virtual instrumentation. The testing hardware uses PXI system architecture and the software is made in NI LabVIEW programming environment.

Keywords: Automatic testing; Power quality; IEC standards; Instrumentation and measurement;

1. Introduction

Due to large expansion of renewable energy resources in distribution grid, occurrence of disturbances in the power system has been increasing during few last years. It leads to degradation of power quality in power system. Therefore, long-term monitoring and evaluation of power quality is becoming increasingly important not only for electricity distributors but also for European regulators and customers.

With regard to these facts, systems for measurement and analysis of power quality are being increasingly used in different places of power system. Although the requirements for evaluation of power quality are described in IEC 61000-4-30 [2], testing equipment for power quality analyzer testing is not currently available. Last year (2012) a new international standard IEC 62586-2 [1] was published which describes new demands for testing power quality analyzers.

The Faculty of Electrical Engineering and Computer Science, VSB-Technical University of Ostrava is currently developing fully automated equipment that would be able to test devices which measure the power quality. This paper is focused on the description of testing correct gapless and non-overlapping measurement.

2. Gapless (non-overlapping) measurement

PQ analyzers compute RMS values from the basic measurement interval of 10/12 cycles (10 cycles at the signal frequency 50 Hz and 12 cycles for the frequency of 60 Hz) which is in both cases 200 ms time period. These values are then aggregated to continue the calculations for the following three periods:

- 150/180-cycles interval,
- 10-minute interval,
- 2-hour interval.

Individual intervals should be connected to each other (gapless) and should not overlap, apart from exceptions in the time synchronization every 10 minutes. Last 10/12 cycles interval in 10-minute intervals usually overlaps over the next 10/12 cycles interval, this interval is then included in the aggregation of the previous 10-minute interval - as Fig. 1 illustrates:

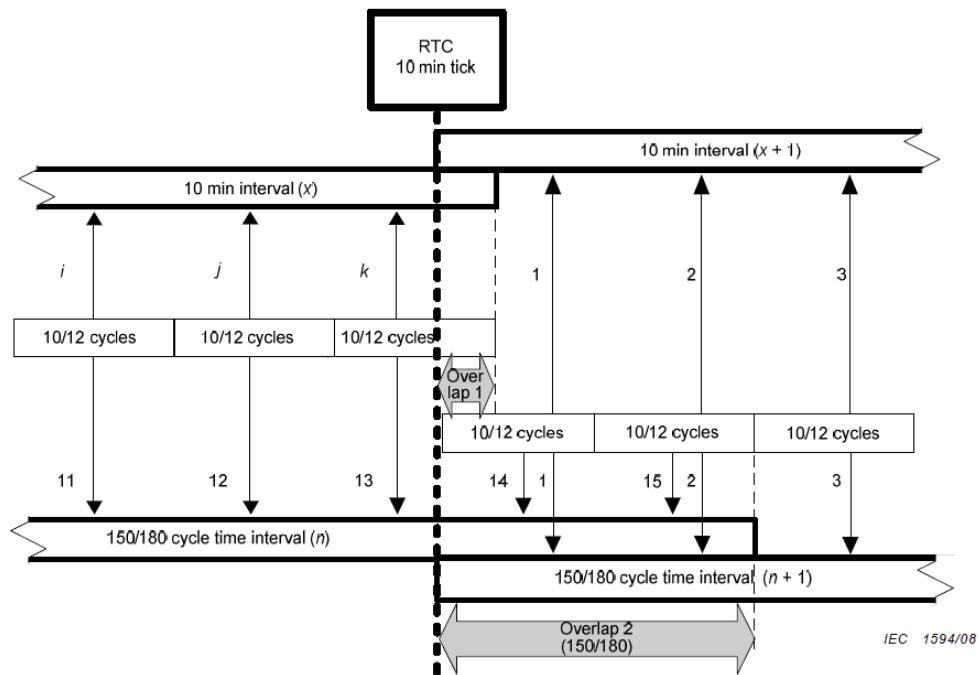


Fig. 1. 10 minute interval synchronization [2]

The exact timing of each interval and the synchronization is not an easy task. Thus there is a suspicion that some power quality analyzers manufacturers can simplify the measuring algorithm, so that an incorrect implementation is not visible at first sight. An example of incorrect implementation (Fig. 2) of 10/12 cycles measurements can be using a moving window of exact length 200 ms (or even greater than 200 ms) although it is required that the RMS values should evaluate for the 10/12 cycles (a frequency deviation from the 50/60 Hz cause inaccuracies).

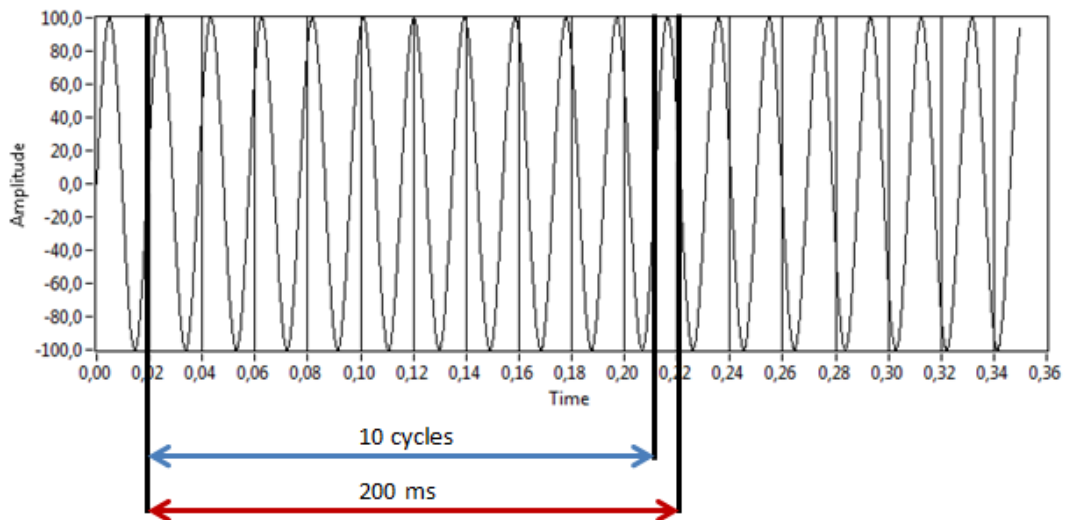


Fig. 2. Example of incorrect 10/12 cycles measurement

3. Test hardware description

In terms of hardware the test system consists of a control computer which is running the test software, which will be described in the next chapter.

The control computer is present here as a PC based device in PXI chassis (PCI eXtensions for Instrumentation). PXI system, which is a part of the tester is marked NI PXI 1033. It is a standard PXI chassis, which can be fitted with up to five extension modules.

Only one expansion module is used and it is a multifunction NI PXI 6733 card, which allows generating analog output signals with sampling frequency up to 1 MS/s. The card is equipped with D/A converter with 16-bit resolution.

With this multifunction card signals are generated for particular tests, as prescribed by the standard. This card, however, allows generating signals only in the range of -10 V to +10 V. Therefore the generated signal is amplified by power amplifiers to the level of 65 V, which corresponds to the declared input voltage (U_{din}) range of a tested power quality analyzer. Thus, the amplified signals for all the three phases can then be routed to the measuring inputs of the power quality analyzer. For purposes of this particular test part usage of only one phase was sufficient.

In Fig. 3 below, please see the block diagram and photography of the real test system, which is stored in mobile 19" rack.

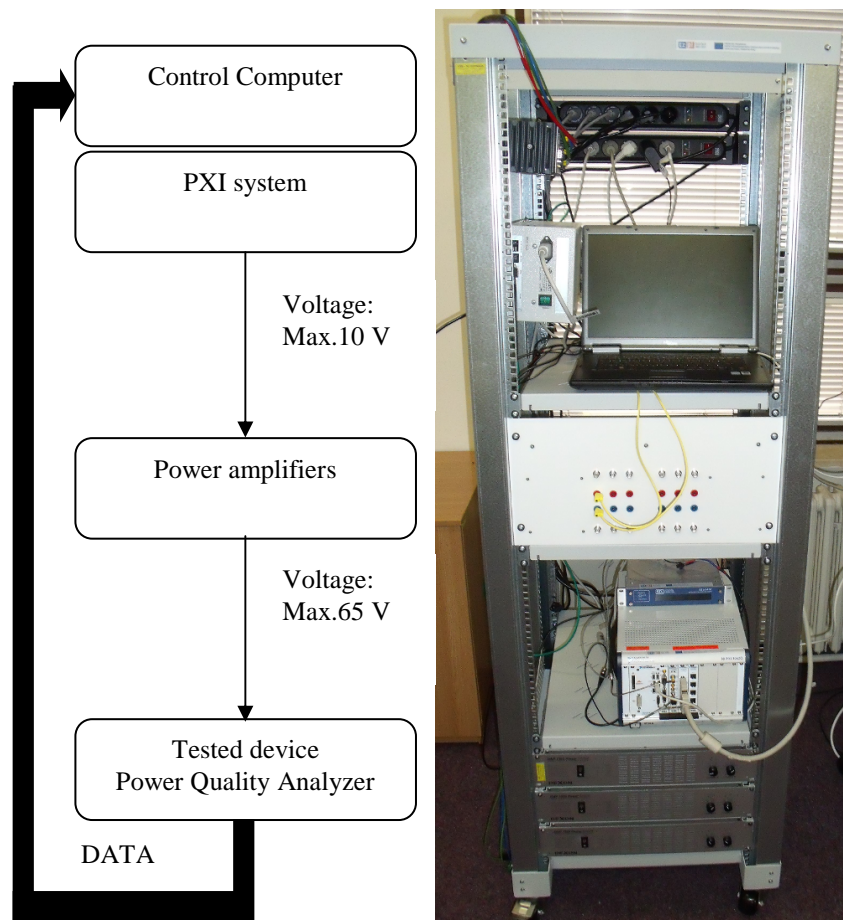


Fig. 3. Block diagram and photography of test system

4. Test description

For testing the correct evaluation of the RMS amplitude, the device under test must be tested with fluctuating signal of fundamental frequency with the following parameters:

- Sinusoidal modulation,
- Basic harmonic component amplitude: 100 % U_{din} , (V_1)
- Basic harmonic component frequency: 50 Hz, (f_1)
- Modulation depth +/- 10 %, (A_m)
- Modulation frequency: 2,3 Hz. (f_m)
- Phases: Not required. (φ_1, φ_m)

Signal can be mathematically expressed as follows:

$$s_{RMS}(t) = V_1 \sqrt{2} \cos(2\pi f_1 t + \varphi_1) (1 + A_m \cos(2\pi f_m t + \varphi_m)). \quad (1)$$

With the above parameters for the voltage U_{din} 230 V signal would be as shown in Fig. 4.

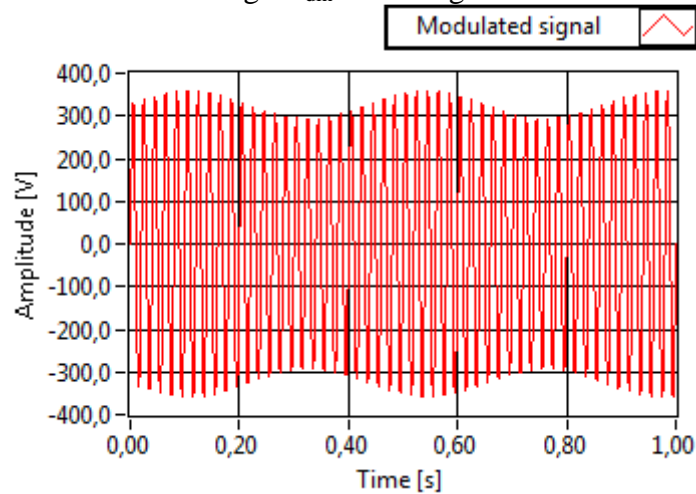


Fig. 4. Modulated (testing) signal

In this ideal case (theoretical simulation) the fluctuation frequency is exactly 2.3 Hz. It is now relatively easy to detect gaps or overlaps during measurement using FFT transformation. The spectrum is calculated from the relative (measured RMS value to U_{din}) RMS values (array of 100 elements).

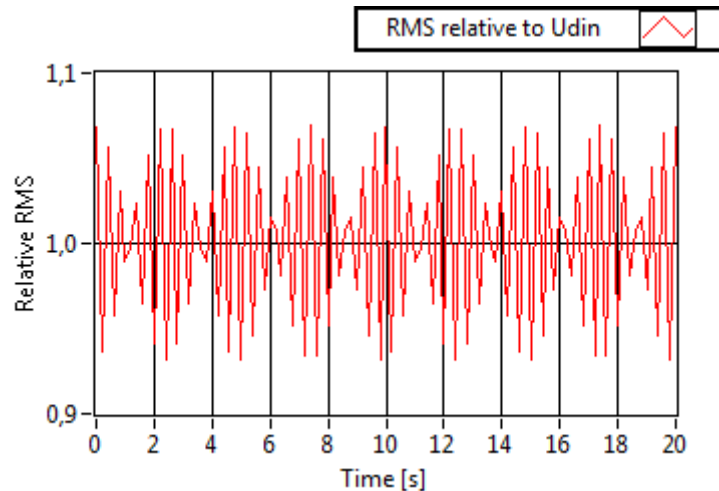


Fig. 5. RMS values relative to U_{din} (theoretical simulation)

If only one missing sample of RMS value in the analyzed array exists, spectral analysis reflects with spectrum leakage effect. It can be seen in the graph in Fig. 6. Blue color shows the spectrum that corresponds to the set of values, in which there are no missing values. Red color shows the spectrum of array that is missing one sample RMS value. The same disproportion in measured values as missing sample causes the gaps or overlaps.

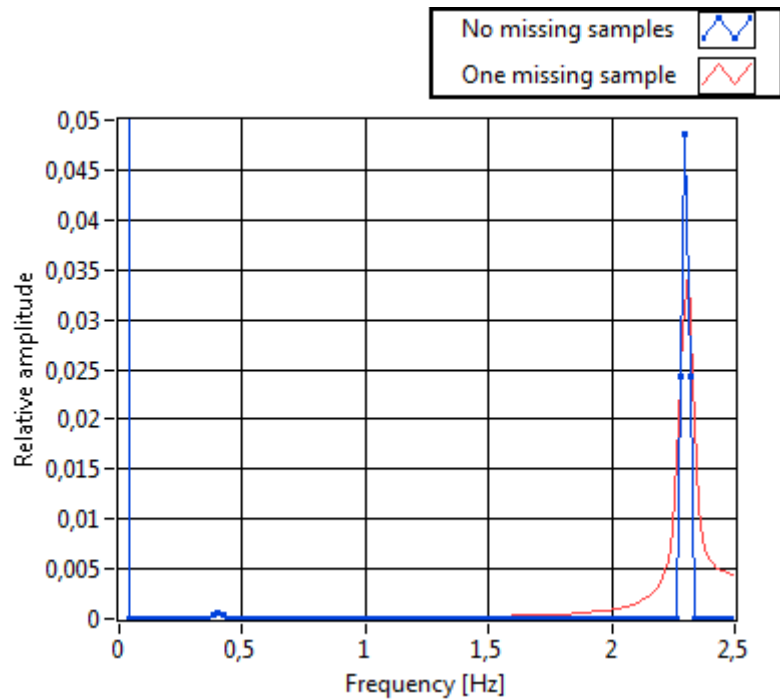


Fig. 6. FFT analysis of RMS variations (theoretical simulation)

The test should not take longer than 10 minutes, as this could lead to a possible overlap due to 10-minute aggregation interval. This, in this case, will be correct.

Voltages U_{din} (Declared input voltage) with an ideal signal / noise ratio should be applied to the test. Manufacturer of test equipment itself should specify the optimum value of this voltage.

The tested device should provide in interval of every 10/12 periods measured value of RMS voltage with a time stamp with the history of the samples with a length of at least 100.

The test device must store the data in a log file, or be able to read the measurement data from the communications port in order to subsequently process the measured data for testing purposes.

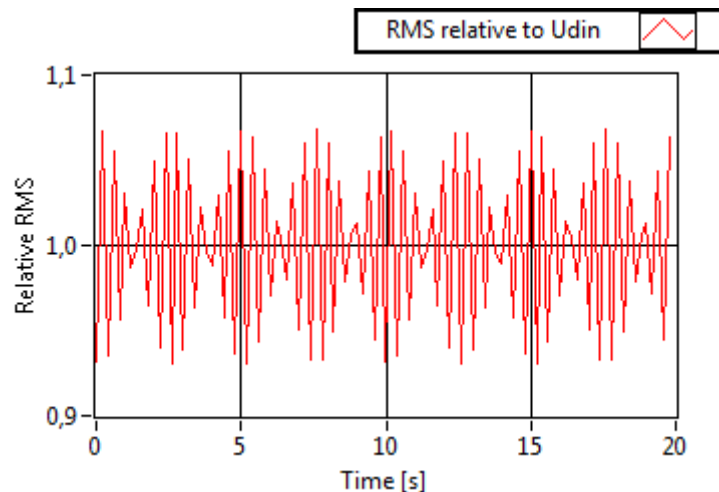


Fig. 7. RMS values relative to U_{din} (PQA ENA330)

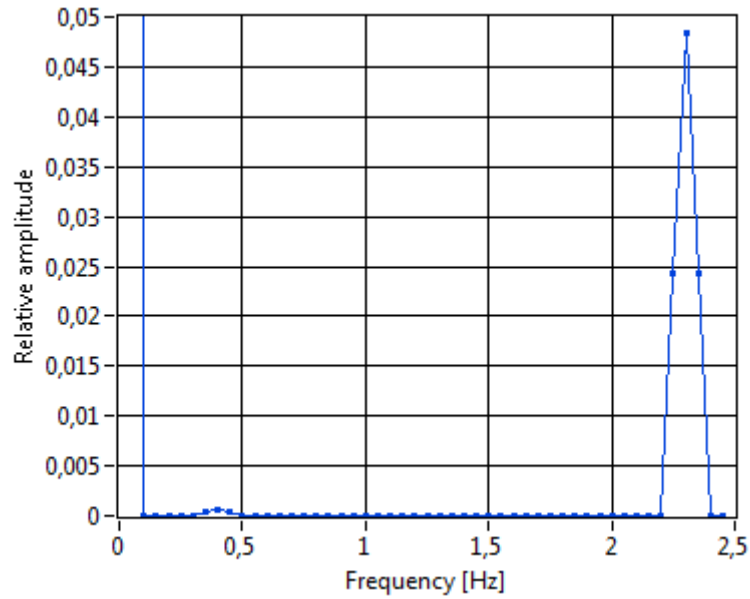


Fig. 8. FFT analysis of RMS variations (PQA ENA330)

Fig. 7 shows the relative RMS values (computed from measured RMS values and U_{din}) by ENA330 analyzer, which was subjected to this test. And Fig. 8 shows the spectral analysis of these values. From the view to the spectral analysis can be concluded that the analyzer meets the terms of the requirement for gapless measurement because there is no visible spectral leakage. But to obtain probative value, it is necessary to perform additional calculations.

5. Evaluation of results

Measured sequence of RMS values from 10/12 cycles period of signal are $U_{rms}(0) \dots U_{rms}(99)$. From this sequence it is possible to calculate the following values:

$$A(N) = \left\| \frac{1}{50\sqrt{2}} \sum_{n=0}^{99} U_{RMS}(n) e^{j2\pi \frac{n}{N} k} \right\|, k = 45, 46, 47. \quad (2)$$

Note: The double line denotes modulus of a complex number.

Where N size of an array with measured RMS values, k is the position of the FFT bin corresponding to the modulation frequency, and $A(k)$ is the amplitude of the bin.

As an indicator of missing samples, or overlaps, the following formula can be used:

$$Q = \sqrt{\frac{A(k)^2}{A(k-1)^2 + A(k+1)^2}}. \quad (3)$$

In this case, the modulation frequency of 2.3 Hz and the field size, determined for FFT analysis, 100 RMS values, the bin corresponding to modulation frequency is $k=46$, assuming that the DC component is bin with index 0.

$$Q = \sqrt{\frac{A(46)^2}{A(45)^2 + A(47)^2}}. \quad (4)$$

According to IEC 62586-2 [1] following requirements should be met:

- 1) $Q > 20$
- 2) $4.5 \% < A(46)/U_{din} < 5.5 \%$
- 3) $\text{Time}(U(99)) - \text{Time}(U(0)) = 20 \text{ s } \pm 6 \text{ ms}$

Analyzing the data measured by the analyzer ENA330 when testing under the above conditions, we came to the following values:

A(45)	A(46)	A(47)	A(46)/U _{din}	Q	t(U(99))-t(U(0))
0,0045	3,16841	0,0073	4,8424 %	369,4703	19,997

Tab. 1. Test result values.

6. Conclusion

Analyzing the results of the test, it was found that the measurement algorithm of tested analyzer ENA330 is processed appropriately according to the requirements of IEC 62586-2. Another analyzer (LEM Memobox 300) was also tested, but was found that this device does not export values with 200 ms interval, the lowest interval available for export values was measured 5 minutes. This is insufficient for analysis, so the unit had to be excluded from testing. The test described in this article is part of a comprehensive tester, it's still in development. Result will be a tester for automated testing of power quality analyzers.

References

- [1] IEC 62586-2 Ed.1. *Power quality measurement in power supply systems: Part 2: Functional tests and uncertainty requirements*. Geneva: International Electrotechnical Commission, 2012.
- [2] IEC 61000-4-30 Ed.2.0 *Electromagnetic compatibility (EMC): Part 4-30: Testing and measurement techniques – Power quality measurement methods*. Geneva: International Electrotechnical Commission, 2008. ISBN 2-8318-1002-0.
- [3] IEC 61000-4-7:2002/A1:2008 *Electromagnetic compatibility (EMC): Testing and measurement techniques - General guide on harmonics and interharmonics measurements and instrumentation, for power supply systems and equipment connected thereto*. Geneva: International Electrotechnical Commission, 2008.
- [4] IEC 61000-4-15 Ed.2.0. *Electromagnetic compatibility (EMC): Part 4-15: Testing and measurement techniques – Flickermeter – Functional design specifications*. Geneva: International Electrotechnical Commission, 2010. ISBN 978-2-88912-076-5

Design control strategy for Inverted Pendulum

* Andrej Rybovič, * Marek Paškala, ** Anna Bystričanová

*University of Zilina, Faculty of Electrical Engineering, Department of Mechatronics and Electronics,
Univerzitna 2, 01026 Žilina, Slovak Republic, {andrej.rybovic, marek.paskala}@fel.uniza.sk

**University of Zilina, Faculty of Electrical Engineering, Department of Mechatronics and Electronics,
Univerzitna 2, 01026 Žilina, Slovak Republic, anna.bystricanova@siemens.com

Abstract. This paper describe a method to design a controller for Inverted Pendulum. This is most solving samples in the area of control theory. Inverted Pendulum is a nonlinear and unstable system which can be used of the various control strategies. We present control method by placement poles to balance the pendulum in the inverted position. For tuning parameters we use Simulink library Design Optimization. The validity and accuracy of design controller are demonstrated.

Keywords: inverted pendulum, nonlinear control system, optimization.

1. Introduction

The growing attention in underactuated mechanical systems leads to optimization design controlling of these devices. Underactuated mechanical systems have fewer actuators than their degrees of freedom [1]. As examples of these systems is the inverted pendulum which often used to demonstrate and verify the effectiveness of control algorithms, e.g. robust model predictive control [2], fuzzy control [3], neural networks [4].

The content of this paper is design controller using state feedback control system and show tuning parameters with process optimization of the use tool Simulink library Design Optimization.

2. Inverted Pendulum system

2.1. Mechanical Model

The model of inverted pendulum is show in Fig.1. The system consists of two basic subsystems: chassis which in this case is sliding cart and a quality rod.

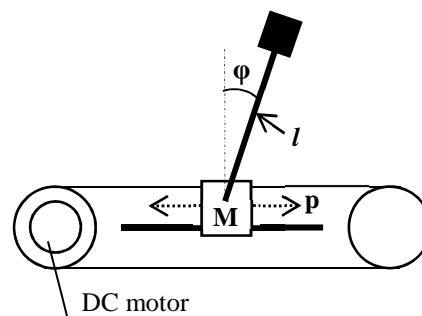


Fig. 1. Scheme of inverted pendulum.

The external force acting on the system is imposed by a DC motor that makes the cart move around the rail. It is also the input of the system. The outputs are cart position p and angle φ of pendulum rod. Movement cart is limited rail length [5].

2.2. Mathematical Model

The dynamic equations of this system consists of cart subsystem (1) and subsystem of pendulum rod (2).

$$F_A - \mu_f \cdot \dot{p}(t) - \mu_{fl} \cdot p(t) - \ddot{p}(t) \cdot M = 0 \quad (1)$$

$$m_p \cdot g \cdot l \cdot \sin(\varphi(t)) - m_p \cdot l \cdot \ddot{p}(t) \cdot \cos(\varphi(t)) - c_p \cdot \dot{\varphi}(t) - \ddot{\varphi}(t) \cdot I = 0 \quad (2)$$

where M is pendulum rod mass m_p and cart mass m_c , \ddot{p} is acceleration of cart, \dot{p} is velocity of cart, p is position of cart, $\ddot{\varphi}$ is angular acceleration of the pendulum, $\dot{\varphi}$ is angular velocity of the pendulum, φ is pendulum angle. Other system parameters are expressed in Tab.1.

Pendulum rod mass	m_p	0.36 kg
Cart mass	m_c	4.0 kg
Distance between the center of gravity and the center of rotation	l	0.451 m
Constant of the friction depending on the speed of cart	μ_f	10.0 kg/s
Constant of the friction depending on the location of cart	μ_{fl}	4 kg/s
Gravity acceleration constant	g	9.81m/ s ²
Moment of inertia of the rotational axis	I	0.08433 kg.m ²
Constant friction of the pendulum rod	c_p	0.00145 kg.m ² /s

Tab. 1. Type sizes for manuscript.

The aim of regulation is hold pendulum rod in equilibrium position. The nonlinear model can be linearized using form of the standard nonlinear state-space description [6]:

$$\begin{bmatrix} \dot{p}(t) \\ \ddot{p}(t) \\ \dot{\varphi}(t) \\ \ddot{\varphi}(t) \end{bmatrix} = \begin{bmatrix} 0 & 1 & 0 & 0 \\ -0.9174 & -2.2936 & 0 & 0 \\ 0 & 0 & 0 & 1 \\ 1.7663 & 4.4158 & 18.8871 & -0.0172 \end{bmatrix} \begin{bmatrix} p(t) \\ \dot{p}(t) \\ \varphi(t) \\ \dot{\varphi}(t) \end{bmatrix} + \begin{bmatrix} 0 \\ 0.2294 \\ 0 \\ -0.4416 \end{bmatrix} u \quad (3)$$

$$y = \begin{bmatrix} 1 & 0 & 0 & 0 \\ 0 & 0 & 1 & 0 \end{bmatrix} \begin{bmatrix} p(t) \\ \dot{p}(t) \\ \varphi(t) \\ \dot{\varphi}(t) \end{bmatrix}$$

For the control devices was need to convert a continuous signal into discrete with sampling period $T=0.03s$.

3. Control design

For control inverted pendulum is used pole placement method. This method is used to place the poles of closed- loop system in the desired positions by state feedback or output feedback [7]. The model described by equations (1) and (2) was created in the MATLAB/Simulink environment. The Simulink scheme is shown in Fig. 2.

Ackermann's formula is used for inverted pendulum control with a view to determine full-state feedback gain K . It is generalized in the sense of direct us of desired eigenvalues instead of characteristic polynomial coefficients. Prefilter p_f ensures that the output corresponds to the steady-state reference variable.

For calculated coefficient of characteristic equation of vector K we need know vector V . Calculation of pole placement and calculate feedback vector K was used with command in Matlab:

$$K=acker(A,B,V)$$

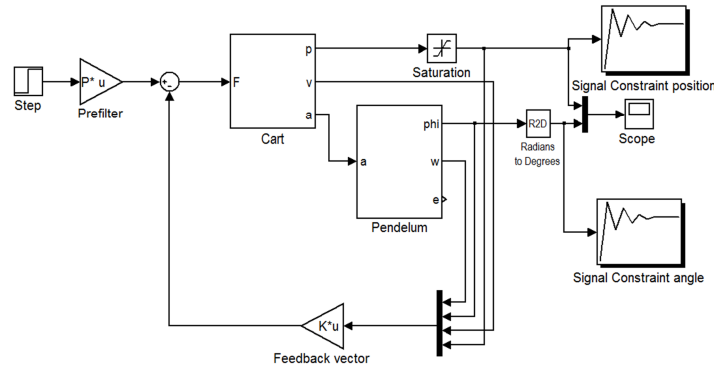


Fig. 2. Simulink scheme of full-state feedback control

Value of V set within the range of 0-1. For stabilization system is progressively finding optimal values of vector V or we can use tool Simulink library Design Optimization. This optimization toolbox improve designs by estimating and tuning model parameters using numerical optimization [8].

4. Simulation results

The experimental results from simulation model are shown on figures below.

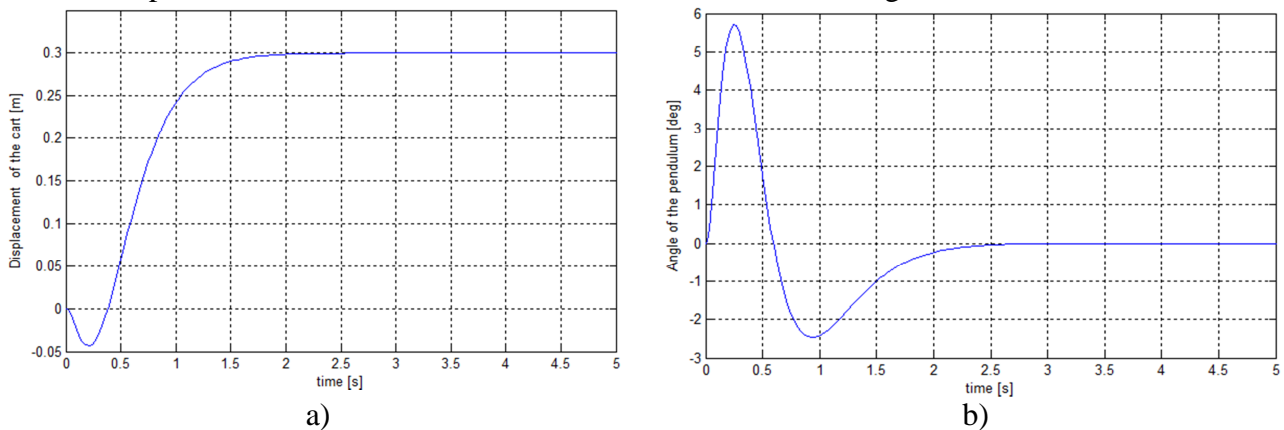


Fig. 3. Experimental result: a) Displacement of the cart, b) Angle of the pendulum

At the beginning was used values for vector $V=[0.8, 0.8, 0.8, 0.8]$. Response on disturbance was very fast which caused system instability with rapid changes of misalignment of the rod. Use optimization tools we have modified the response system to the required values. The result is shown in Fig.3.

5. Conclusion

In this paper has been presented the application of state feedback control for regulation stabilization of inverted pendulum. It was used the Ackerman formula that allow to put poles in our target position. The next step was showed as with help Simulink toolbox set required values. The simulation results demonstrated that the system can successfully be handled by using this type of controller.

Acknowledgement

The author wish to thank to project VEGA no.1/0943/11 and project OPVaV-2008/2.1/01 SORO 262220120003.

References

- [1] SPONG, M. W., PRALY, L. *Control of Underactuated Mechanical Systems Using Switching and Saturation*. Press in Lecture Notes in Control and Information Sciences Volume 222, 1997, pages 162-172.
- [2] GHANAVATI, M., MAJD, V. J., GHANAVATI, M. *Control of Inverted Pendulum system by using a new robust model predictive control strategy*. International Siberian Conference on Control and Communications (SIBCON), 2011, pages 27 – 32.
- [3] DHANNI, Y. K. *Single Input Variable Universe Fuzzy Controller with Contraction-Expansion Factor for Inverted Pendulum in Real Time*. Press in AEEE Volume 10, Number 5, 2012 pages 317 – 322.
- [4] JUNG, S., KIM, S. S. *Control Experiment of a Wheel-Driven Mobile Inverted Pendulum Using Neural Network*. In IEEE Transactions on Control Systems Technology, 2008, pages 297 – 303.
- [5] Amira GmbH, Duisburg <http://www.amira.de>.
- [6] JADLOVSKÁ, S., SARNOVSKÝ, J. *A Complex Overview of the Rotary Single Inverted Pendulum System*. ELEKTRO 2012, pages 305 – 310.
- [7] LAN, Y., MINRUI, F. *Design of State-feedback Controller by Pole Placement for a Coupled Set of Inverted Pendulums*. 10th International Conference on Electronic Measurement & Instruments (ICEMI), 2011, pages 69 – 73
- [8] MathWorks, <http://www.mathworks.com>



The influence of the interphase reactor on the operation of 12 - pulse AC/DC thyristor rectifier

*Paweł Stawczyk

*Kielce University of Technology, Faculty of Electrical Engineering, Automatics and Computer Science, Al. Tysiąclecia Państwa Polskiego 7, 25-314 Kielce, Poland, pawel83ck@gmail.com

Abstract. The parallel connection of 6 - pulse component bridges in the 12 - pulse rectifier requires associating inductors. The article presents an analysis of the influence on interphase reactor on the operation 12 - pulse AC/DC thyristor converter. Very important issue is to set the limit value of the load current, at a given firing angle of the thyristors which is working properly.

Keywords: AC/DC converter, power quality, interphase reactor, line currents, controlled rectifiers, multi-pulse AC/DC converters

1. Introduction

AC/DC converters are non-linear electrical loads which generates the higher harmonic currents into the power systems. Current deformations causes the increase of the active power losses and voltage waveform distortion in the AC networks. Multi-pulse systems (q - pulse) are used in order to reduce higher harmonic currents and voltages to the value specified by international standards.

It is possible to increase q number in the classical approach by series or parallel connection of p number of 3 - phase bridges which are supplied by transformers with required phase shifting.

$$\phi = \frac{2\pi}{q p} . \quad (1)$$

where p - number of parallel connected 6 - pulse bridges, q - pulse number

Serial connection is not generally used because of increase in the total voltage drop on conducting semiconductor devices. Parallel connection requires interphase reactors enabling independent operation of the component bridges.

2. 12- pulse thyristor rectifier

An example of solution significantly reducing line current distortions of the network is the 12 - pulse controlled rectifier which is an extension of 12 - pulse diode rectifier with modulation in DC current circuit.

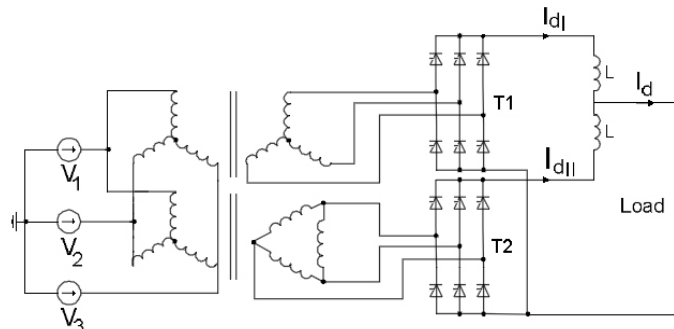


Fig. 1. 12 - pulse thyristor rectifier

Rectifier consists of two parallel connected 6 - pulse thyristor bridges supplied by Y/Y and Y/ Δ transformers with the required 30^0 phase shifting. This shifting is necessary for the proper operation of the 12 - pulse rectifier and allows to obtain stair shape of the line supply currents.

Simulation investigations have shown that properly selected interphase reactors cause the 12 - pulse controlled rectifier works as multipulse rectifier.

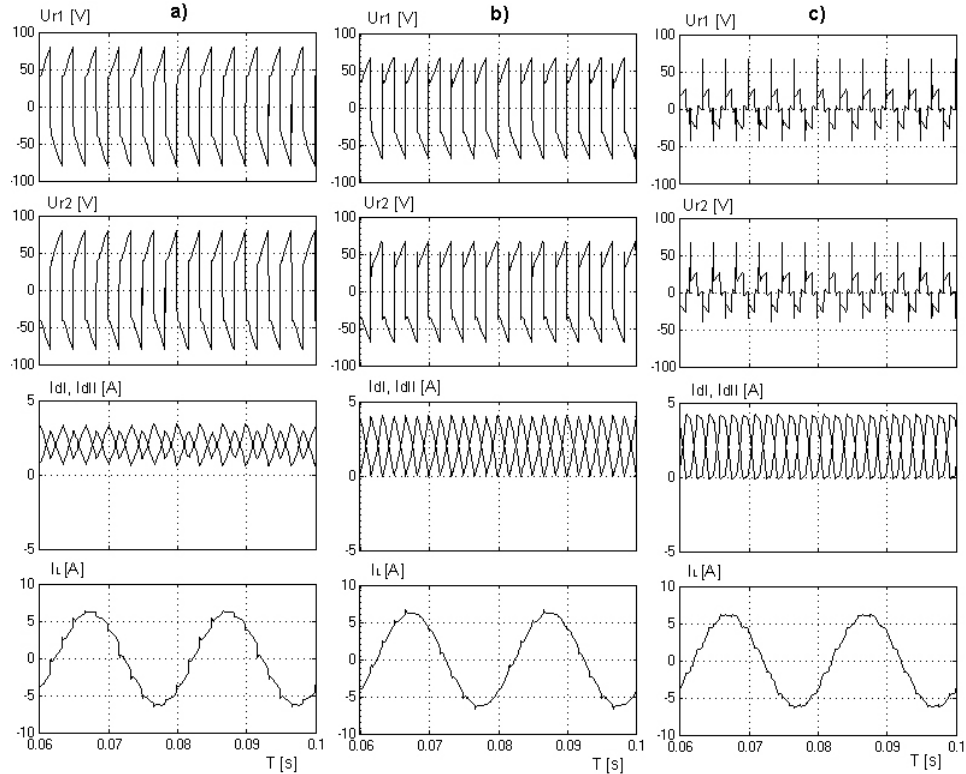


Fig. 2. Influence of interphase reactor on the load level of the component bridges T1 and T2 at the given firing angle $\alpha=45^0$: a) $L=0,04$ H, b) $L=0,02$ H, c) $L=0,005$ H

Taking into account:

$$I_{dI} + I_{dII} = I_d \quad (2)$$

$$I_{dI} = I_{nd}$$

The value of inductance L at the given firing angle of thyristors and the load current I_d should be such that amplitudes of the currents components bridges T1 and T2 were equal to half value of the load current. Load unbalance of the bridges, which can be seen in “Fig. 2” results from the initial conditions of the system. It can be seen, that the bridge which first begins to operate ie gets the first pulse of thyristors, takes part of the load current of the second bridge, which is attached at the end of 1,66 ms (delay angle 30^0). Assymetry in the load of both bridges is directly dependent on the value of the load I_d and interphase reactor L .

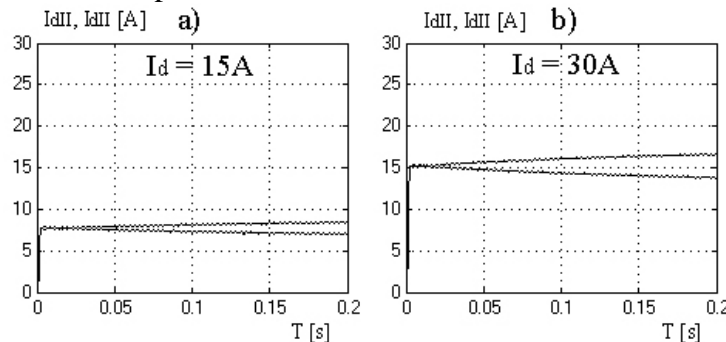


Fig. 3. The influence of the loading current on the component bridges current assymetry: $L=0,5$ H, $\alpha= 18^0$

The simulations showed that for a given firing angle of thyristors there is a correlation between inductance of interphase reactors L and value of the load I_d for the 12 - pulse rectifier working as multipulse converter.

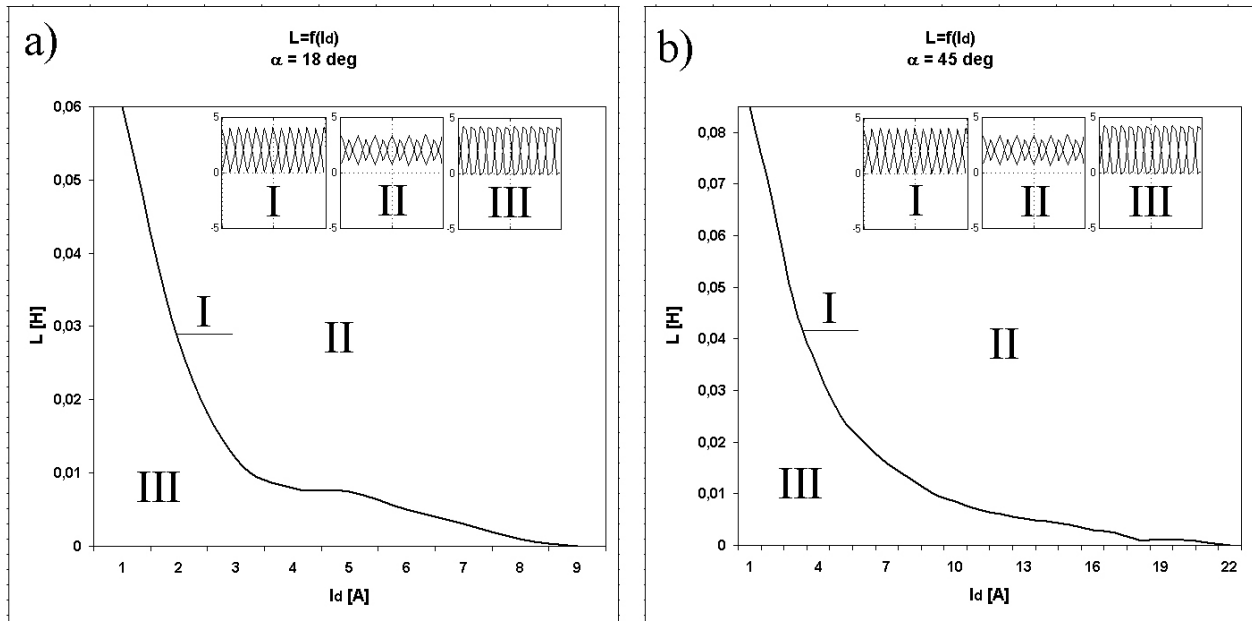


Fig. 4. The dependence of interphase reactor inductance on loading current $L=f(I_d)$: I- multipulse operation, II- underload operation, III- overload operation

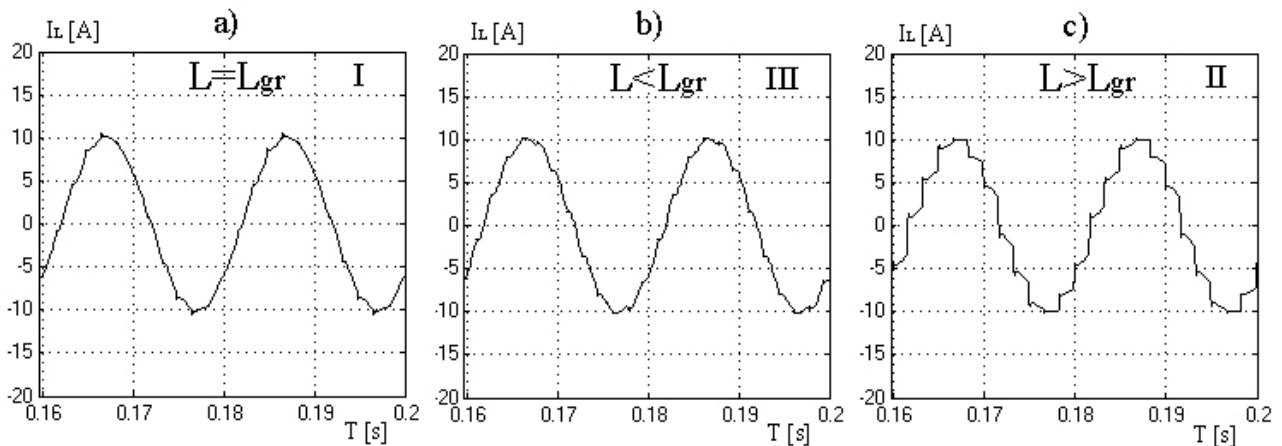


Fig. 5. The line current waveforms for loads as shown in “Fig. 4”, respectively

3. Conclusion

The properly selected firing angle of thyristors in relation to a specified loading current result in time-varying loads of the components bridges T1 and T2 in such way that the sum of the loading currents I_{dI} and I_{dII} of these systems is equal to loading current I_d of the rectifier. Suitable values of inductance (Fig. 4) provides the multi-pulse operation of the rectifier. The shape of line currents of the converter in consequence is close to sinusoidal.

Acknowledgement

The research has been partially funded by: NCN – research project N N510 356936

References

- [1] ROLEK, J. *Układy prostowników wielopulsowych z modulacją w obwodzie prądu stałego*. Przegląd elektrotechniczny, ISSN 0033-2097, R. 84 NR 5/2008.
- [2] ANRVINDAN, A, N., PUSHPAKARTHICK, P. *24- pulse rectifier realization 3-phase to four 3-phase transformation using conventional transformer*. NPEC 2010.
- [3] MIYAIRI, S., IIDA, S., NAKATA, K., MASUKAWA, S. *New Method for Reducing Harmonics Involved in Input and output of Rectifier with Interphase Transformer*. IEEE Trans. On Industry Applications, IA-22 (5), 790-797.
- [4] KAPŁON, A., ROLEK, J. *Analysis of Multipulse Rectifiers with Modulation in DC Circuit in Vector Space Approach*. 2008 13th International Power Electronics and Motion Control Conference (EPE-PEMC 2008).
- [5] PAICE, D ,A. *Power Electronic Converter Harmonics Multipulse Methods for Clean Power*. IEEE PRESS New York 1996.
- [6] YOUNIS, M., RAHIM, N., MEKHLEF, S. *Harmonic reduction in a three-phase rectifier with sinusoidal current*. Power System Technology, 2002. PowerCon 2002. International Conference on, (pages 2251 – 2255 vol.4).



Digital protection relay for 22 kV power line model

*Dominik Szabó, *Michal Reguľa, *Marek Höger

*University of Žilina, Faculty of Electrical Engineering, Department of Power Electrical Systems,
Univerzitná 1, 01026 Žilina, Slovak Republic, {Dominik.Szabo, Michal.Regula, Marek.Hoger}@fel.uniza.sk

Abstract. The paper deals with the function and structure of a digital protection relay used in 22 kV power lines. It contains the description of the relay's software and hardware and its realization. The device is designed for the three-phase 22 kV power line model. The proper function of the created protection relay is verified by real model tests.

Keywords: digital protection, electric protection device, voltage measurement, current measurement

1. Introduction

With the increasing number of new computer technologies, digital protection relays are improved as well. They are becoming more spread and affordable. Digital protection relays can also perform several other tasks and thus they contribute to monitoring, control and operating of the electrical power system and its components in real-time [1].

Digital protections play a very important role in every electrical power system. During normal fault-free operating condition they are useless but when a system failure or abnormal condition occurs they are vital. If an electrical protection device is designed properly only the affected power line section is disconnected during a system fault and the rest of the system equipment can continue to operate independently [2].

The fundamental parts of this type of protection relays are digital circuits. All or some of the variables within these devices are displayed and processed using discontinuous (discrete) values. Individual data are displayed by combinations of log "0" and log "1". The digital device is able to processed the complex information about the entire object. In state space \mathbf{P} the vector $\mathbf{x}(t)$ can be monitored in all n directions [3].

2. The digital protection design

For realization of the digital protection relay the digital SMART metering demo board DEMOEN is used. The hardware and software of the protection relay is designed to cooperate simultaneously. Thus the complex protection system is created and ready to be used in 22 kV power line model. The hardware of the proposed digital protection model consists of three main parts: measurement unit, controller and output power unit.



Fig. 1. The digital protection structure

2.1. The measurement unit

This part of the model provides current and voltage measurements. The outputs are six low voltage analogue signals ($0 \div 3,3$ V). In order to transfer them to digital values, these signals are processed by A/D converter in the next step. The electrical scheme of the measurement unit is

depicted in Fig. 2. It is divided into two sections – current measurement (the upper part) and voltage measurement (the lower one). The currents are measured by current transducers LEM HY 10p, which convert actual currents flown through phases to corresponding output voltage signals in the range of ± 4 V. For phase voltages measurement voltage dividers are implemented. Since the controller is fed by the voltage of $0 \div 3,3$ V it is able to process only positive voltage signals. Therefore, some DC offset must be added to the output signals so that they can be processed by the controller. This is executed by several operational amplifiers in the right hand side of the scheme. The voltage signals are superimposed by $+1,65$ V DC offset in the first step to ensure all the signals range from 0 to 3,3 V with $+1,65$ V DC as the mean value. Next, antialiasing filters are applied to reduce signal noise and ripple. The analogue signals obtained in this form are suitable for A/D converter processing and some other devices as well (e.g. data acquisition cards).

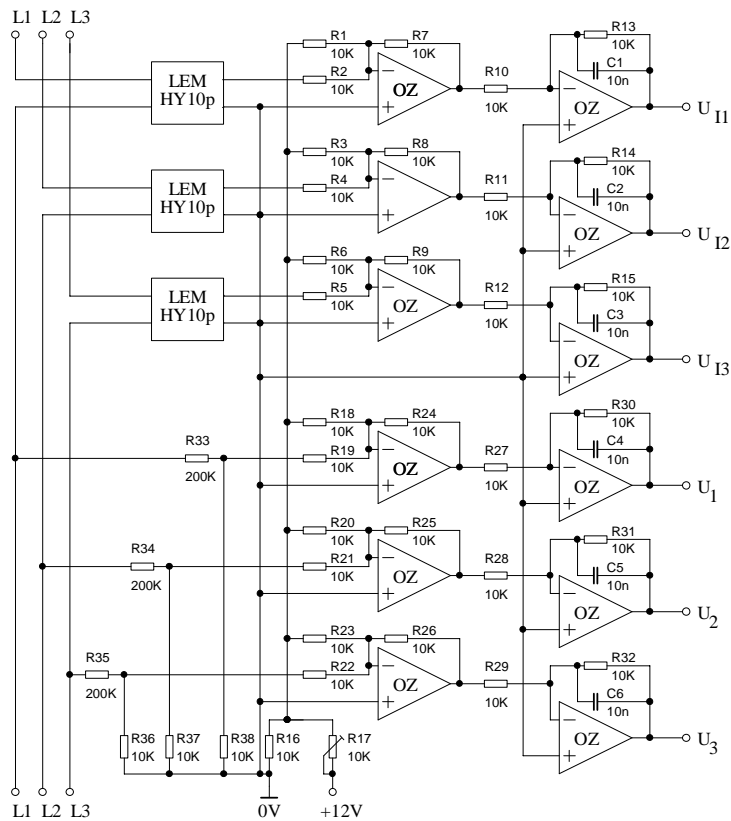


Fig. 2. The electrical scheme of the measurement unit

2.2. The controller

The core of the control unit is SMART metering demo board DEMOEM with microcontroller MCF51EM256. For this microprocessor the following algorithms are implemented: overcurrent protection (instantaneous and time overcurrent), line distance protection and earth-fault directional protection for earth-faults detection in the networks with isolated neutral point.

From automatic functions autoreclosing was integrated. The communication with the actuator is done using serial port RS232, which provides monitoring of the individual protections statuses, autoreclosing, power circuit breaker and all the measured variables.

One of the basic protections is overcurrent protection. This type of the protection has two main stages. The first one reacts on the overcurrent and second one reacts on the short circuit current. The difference between these two stages are starting current and tripping time. The possibility how to adjust a nondirectional overcurrent protection is as follows:

OverLevel_I(Val_I, strVal_I, endVal_I, tripTime_I, prtIndex_I);

where *Val_I* – measured phase currents,
strVal_I – starting current value,

- $endVal_I$ – holding current value,
- $tripTime_I$ – tripping time,
- $prtIndex_I$ – protection stage index.

According to the algorithm, RMS value of the current is computed instantly and compared with the desired value. Similarly, phase voltages can be monitored as well but only for signalization in the case of voltage sag or power supply loss.

The algorithm of the earth-fault directional protection is adjusted in such a way that it analyses and compares three variables – voltage and current zero sequence and their phase angle. The phase angle is computed on the base of signal zero crossing and in the case of sampling frequency of 64 samples per second the accuracy is $\Delta\varphi = 5,625^\circ$. The algorithm analyses whether the following three conditions are fulfilled at the same time:

- 1) $U_0 > 40\%$ of U_N
- 2) $I_0 > 1 \div 4\%$ of U_N , 0,5 % step size (depending on the power line length)
- 3) $P_0 > 0 \Rightarrow \varphi \in < -90^\circ, 90^\circ >$ (power flows from the source)

The distance protection algorithm evaluates the magnitude of a fault loop. For the algorithm circle shape impedance diagram was used with the center in the origin of R-X axis system. In the protection, there are three stages of the starting impedance values and the corresponding tripping times.

Every digital protection includes autoreclosing function. This function is called every time when any of the protection algorithms detects a fault. In the algorithm the potential-free time and blocking time is adjusted.

The algorithm is implemented into the microprocessor memory and thus the control unit is created and it is able to control the entire protection device.

2.3. The power unit

Fig. 3. shows the electrical scheme of the power section that is controlled by a bistable flip-flop circuit. The trip signal enters the set input of this circuit and at the reset input the control and interlocking of autoreclosing is brought. The essential power component of the output unit is a relay, which provides disconnecting of the power line section from the power supply and guarantees a secure galvanic isolation between the electronic equipment and the power circuit.

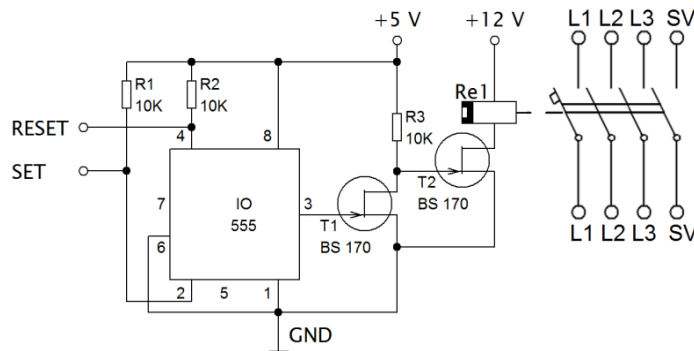


Fig. 3. The output power unit scheme

3. Measurements

In order to prove the correct function of the device, it was necessary to perform some tests. One of these tests is to investigate the output unit reaction on the trip signal, autoreclosing and blocking time. Fig. 4 shows the time-base principle of the digital protection operation. Three different time values were measured – delay time, potential-free time and blocking time of autoreclosing. The acquired times are compared with their preset values in Tab. 1.

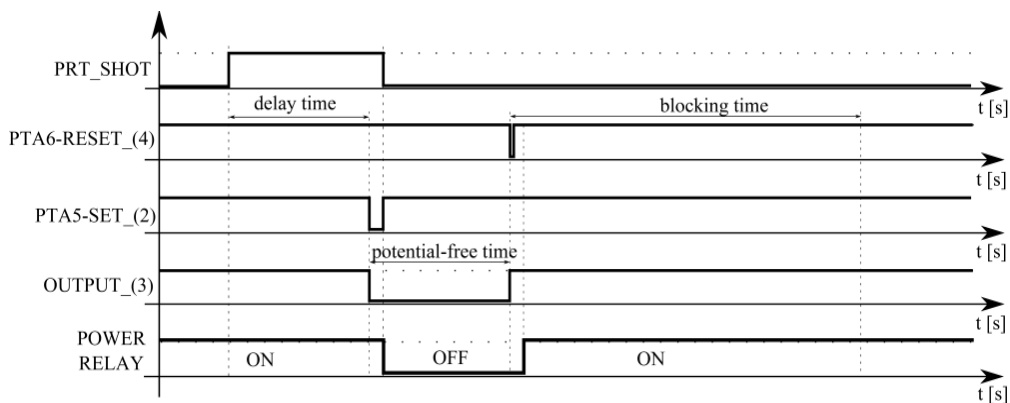


Fig. 4. Time-base principle of the digital protection operation

It is clear, that the timer is designed properly. Thus the implementation of the timer in the digital protection relay is possible and satisfactory.

Delay time		Potential-free time		Blocking time	
preset	measured	preset	measured	preset	measured
0,2 s	0,209 s	0,3 s	0,302 s	3 s	3,00 s
0,3 s	0,311 s	0,5 s	0,518 s	5 s	5,02 s
0,5 s	0,505 s	0,8 s	0,825 s	10 s	10,09 s
1 s	1,01 s	3 s	3,01 s	20 s	20,2 s

Tab. 1. Measured times and their preset values

4. Conclusion

The created digital protection relay is primarily designated to protect 22 kV power line model but it can be employed in many other applications such as education purposes or illustration of the electric protection operation. Since it is a digital device, it is possible to easily modify its software and a new control algorithm or communication with other devices can be implemented. The model of digital protection is suitable for the next research and because it contains demo board, various built-in modules and functions can be used in the future.

Acknowledgement



Project: Cooperation between the University of Žilina and VSB-TU Ostrava at the improving quality of education and training of researchers for the field of electrical engineering, ITMS 22410320029.

References

- [1] CHLADNÝ, V. JANÍČEK, F. BELÁŇ, A.: *Digitálne ochrany v elektrizačných sústavách*, Mercury Smekal, Košice, 2003, ISBN 80-8906173,7.
- [2] BLACKBURN, J., DOMIN, t.: *Protective relaying, Principles and Applications*, CRC Press 207, ISBN1-57444-716-5.
- [3] DOHNÁLEK, P.: *Ochrany pro průmysl a energetiku*, Nakladatelství technické literatury SNTL, Praha, 1978
- [4] HRAŠKO, M., HÖGER, M., HEČKO, P.: *Modeling and identification of failures in distribution network*. EE 09, Stará Lesná, 2009, 09, 23.-25., AFD, p.: 346 – 349.



Measurement and Data Acquisition from Technology of Thermal Borehole Polygons

*Tomas Vavrla, *Jiri Koziorek

*Department of Cybernetics and Biomedical Engineering, Faculty of Electrical Engineering and Computer Science, VSB – Technical University of Ostrava, 17.listopadu 2172/15, Ostrava – Poruba, 70833 Czech Republic, {tomas.vavrla, jiri.koziorek}@vsb.cz

Abstract. This paper deals with research and development of a system for measuring temperature profiles of boreholes. This work is mainly focused on developing the 1-Wire interface application library, implementation of a PLC (type of BR X20) into this measurement system, and realization of an autonomous database server used for saving the acquired data and a failure diagnostics.

Keywords: 1-Wire interface, Ethernet, FTP server, Micro LAN, ODBC, OPC, PLC and RS232.

1. Introduction

Nowadays, mankind is beginning to recognize the issue of finding alternative sources of energy, because fossil fuel era is coming to end. Geothermal energy is one of many possible types of energy for the acquisition of clean energy. The term “Geothermal energy” can be defined in a broader sense as heat in the Earth’s core and mantle. It is used in the form of thermal energy for residential heating or for electricity generation in geothermal power plants. The use of this energy is indeed simple at first glance, but the technical solution is difficult, because the hot water extracted from itself borehole contains many minerals and thereby clog technological devices [1].

Two experimental works (the experimental polygons) are in the vicinity VSB – TUO. They deal with the issue of geothermal energy (temperature changes of the rock massif) [1, 2, 3]:

- The Big Research Polygon (BRP),
- The Small Research Polygon (SRP).

Other experimental work is located in the place of the company Green Gas. The measuring system on both polygons acquires information about the behavior of heterogeneous earth and heat pumps. The information obtained is used for mathematical modeling and simulation of heat exchange (between the earth and the heat pump) and the prediction of system behavior in the future [1, 2, 3].

The work realizes two basic parts:

- Realization of the measuring system by using the Micro LAN network – This part is described in chapter 2 and chapter 3,
- Realization of the database server for saving data – This part is described in chapter 4.

Communication is introduced in order to limit the number of wires in the borehole. Direct use of sensors (the analog sensors) for every sensor requires at least two wires. Number of wires in the communication (the digital or the analog sensors with communication interface) with a higher number of sensors remains the same.

2. Micro LAN

This is a simple and inexpensive network technology for automation. It is defined in norm IEEE 1451.4. It uses 1-Wire protocol, therefore the 1-Wire bus. Components are devices and equipment with 1-Wire interface and block 64 to 128 bits identification number (8 bits => CRC, 48

bits => serial number and 8 bits => device type „family code“). Identification number can uniquely identify the device on the network. Device containing these two parts is declared by the manufacturer as standard Micro LAN. Other parts of the network may be different adapters and controllers [1].

3. The system with the Micro LAN network

Basic of measuring system (The Small Polygon and Green Gas) is programmable logic controller. The programmable logic controller is based on X20 architecture the Austrian manufacturer Bernecker & Rainer. Micro LAN network and programmable logic controller are connected converter communications. This converter converts the 1-Wire communications on the serial communications (RS232). The programmable logic controller work as Master. It is control the communication process. Superior system PLC consists of desktop computer with HMI/SCADA applications (visualization using VNC) and the database system. Block diagram of the system with Micro LAN network is show in Figure 1. The complete system has the following features [1]:

- Temperature measurement by using 1-Wire sensors (type of DS18B20),
- Control of Micro LAN communication using serial link,
- The obtained temperature data are saved into a FLASH memory card and a database system,
- Data transmission through integrated Ethernet interface,
- The direct FTP access to PLC,
- Control system with Micro LAN network and data visualisation using HMI/SCADA application (e. g. VNC visualization).

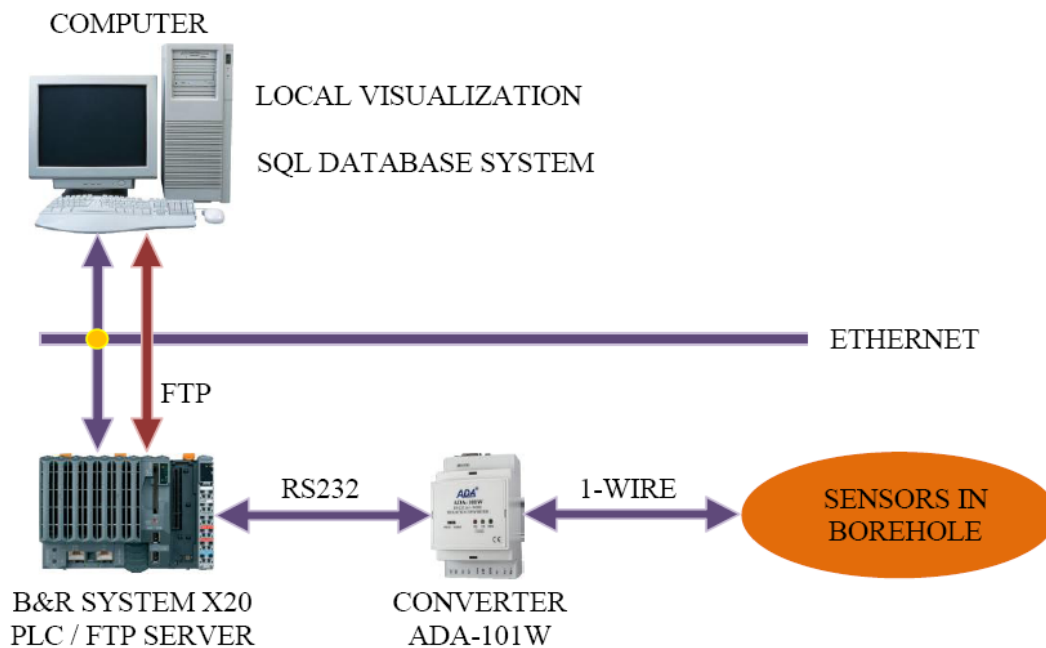


Fig. 1. Block diagram of system with Micro LAN network [1].

The software programmable logic controller has two parts. The first part performs network control (network management). The second part performs the evaluation of measured data. The data are sent over Ethernet to the desktop computer or saved to file on the FLASH card. The file can be read or downloaded at any time as programmable logic controller working as an FTP server. So if the PLC stops working for some reason, the obtained data are always available on the FLASH card and on the FTP. In addition, the FLASH card saves the configuration file with line spacing and the error file. Into the error file is saved the error flags (text with an error description) [1].

On the end of the communication (communication between the programmable logic controller and sensors) is evaluation of data. The data are evaluated after the end of communication comparing the identification number sensor with the table identification numbers. Table identification numbers are created in advance based on the position sensors in the borehole. We get specific information about the position sensors in the borehole and the appropriate temperature [1].

The most important part is communication and its control. For this purpose was developed the universal library of the functions using ANSI C. The library is dependent on the support serial communication (RS232). This library can be used in any programmable logic controller Bernecker & Rainer with support for serial communication. The library consists of three blocks of elementary functions:

- **The function for handling serial port PLC** – It contains the elementary functions for working with the serial port. E.g.: Functions for opening and closing the serial port. etc.,
- **The utilities** – It contains the auxiliary functions. They are: function for implementation delay; functions for realization of the CRC calculation and function realization conversion format the identification number into human readable form. The most important functions are function for calculating the CRC (Influence communication). Function for calculating the CRC detects the errors.,
- **The function for communication with 1-Wire network** – This is the most important block of the elementary functions. Elementary functions for realization of communication uses the functions for handle the serial port.

Combining the elementary functions (from the third block “Function for communication with 1-Wire network”) is implemented communication between the programmable logic controller and the 1-Wire sensors [1].

4. The autonomous system for acquisition of data and diagnostic of failures

The result is the autonomous database server system saves data from connected devices. The system includes of testing errors. Errors are tested for individual communications. Based on the detected error is send an SMS message or e-mail system administrator. Message contains the detected error and requests its removal.

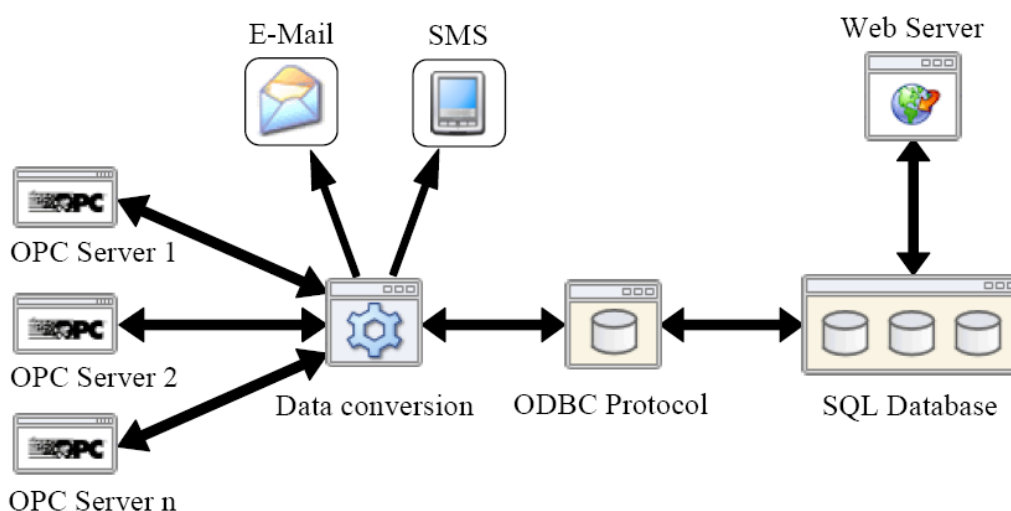


Fig. 2. Block diagram of data acquisition and failure/error diagnostics.

Core of the system is a computer with architecture designed for server application. The device provides data to the system connected via the Ethernet and OPC protocol. An OPC-ODBC conversion is the most important part of this information system. During this conversion errors may

occur, therefore the system includes means for the detection of errors. The acquired data is saved in a SQL database. Part of the system is web visualization (the SCADA application). The web visualization shows the individual data (Errors = E-mail, data = SQL) in the form of tables and graphs.

Currently, this autonomous system is connected with Small Research Polygon, Big Research Polygon and the measuring device from Green Gas.

5. Conclusion

Based on this work it was developed measuring system and autonomous system for data acquisition. Both systems were created on several communication protocols (ODBC, OPC, Ethernet, RS232 and Micro LAN).

The principle of measuring system is a library and communication converter that controls all measurement. Order to the library could be used in other applications of measurement and control is universal. It is limited to the use of programmable logic controller Bernecker & Rainer.

The principle of autonomous system is data transfer “data conversion”. It is possible for him connect many data sources (using OPC). The system is therefore universal. The final autonomous system has been registered as a function pattern (106/08-12-2011_F).

Acknowledgement

This work was partly supported by European operational program “Slovakia - Czech Republic 2007-2013”, project name “Collaboration between University of Zilina and VSB-TU Ostrava in increasing of quality of education and preparation of researchers in the area of electrical engineering”, project registration number 22410320029.

References

- [1] VAVRLA, T., KOZIOREK, J. *Temperature Measurement in Boreholes by Programmable Logical Controller B&R and Temperature Sensors 1-Wire*. In PDES 2012: Proceedings of 11th IFAC/IEEE International Conference on Programmable Devices and Embedded Systems, Brno, Czech Republic, May 23 – 25, 2012, p. 358 – 363.
- [2] HAJOVSKY, R., KOZIOREK, J. *Using PAC System for Temperature Monitoring*. In ICSE 2009: Proceedings on 20th International Conference on Systems Engineering, Coventry University, Coventry, United Kingdom of Great Britain and Northern Ireland, 2009, p. 195 – 200.
- [3] KOZIOREK, J., HORAK, B., HAJOVSKY, R., BUJOK, P. *Measurement of Thermal Conditions in Rock Massif*. In PDES 2009: Proceedings on 9th IFAC Workshop on Programmable Devices and Embedded Systems, VSB – TUO, Ostrava, Czech Republic, p. 230 – 235.

TRANSCOM 2013

Proceedings, Section 4

Published by University of Žilina

First Editions

Printed by EDIS-Žilina University publisher

Printed in 60 copies

ISBN 978-80-554-0693-0